University of Genoa

Doctoral Thesis

Elastically-bounded flapping plates for flow-induced energy harvesting

Author:
Stefano Olivieri

Supervisor:
Prof. Andrea Mazzino

A thesis submitted in fulfillment of the requirements for the degree of Doctor of Philosophy

Doctoral School in Civil, Chemical and Environmental Engineering
Curriculum in Fluid Dynamics and Environmental Engineering

April 6, 2020

Supervisor:
Prof. Andrea Mazzino - DICCA, University of Genoa

External Reviewers:
Prof. Markus Holzner - WSL and ETH Zürich, Zürich (CH)
Prof. Paolo Gualtieri - DIMA, University of Rome "La Sapienza", Rome (IT)

Examination Committee:
Prof. Alessandro Bottaro - DICCA, University of Genoa
Prof. Giorgio Bellotti - Department of Engineering, Roma Tre University, Rome (IT)
Prof. Daniele Rocchi - Department of Mechanics, Politecnico di Milano, Milan (IT)

Ph.D. Program in Civil, Chemical and Environmental Engineering
Curriculum in Fluid Dynamics and Environmental Engineering
Cycle XXXII

Abstract

Elastically-bounded flapping plates for flow-induced energy harvesting

by Stefano Olivieri

This work concerns a novel concept for energy harvesting (EH) from fluid flows, based on the aeroelastic flutter of elastically-bounded plates immersed in laminar flow. The resulting flapping motions are investigated in order to support the development of centimetric-size EH devices exploiting low wind velocities, with potential application in the autonomous powering of low-power wireless sensor networks used, e.g., for remote environmental monitoring. The problem is studied combining three-dimensional direct numerical simulations exploiting a state-of-the-art immersed boundary method, wind-tunnel experiments on prototypal EH devices, and a reduced-order phenomenological model based on a set of ordinary differential equations. Three key features of the aeroelastic system are investigated: (i) we identify the critical condition for self-sustained flapping using a simple balance between characteristic timescales involved in the problem; (ii) we explore postcritical regimes characterized by regular limit-cycle oscillations, highlighting how to maximize their amplitude and/or frequency and in turns the potential energy extraction; (iii) we consider arrays of multiple devices, revealing for certain arrangements a constructive interference effect that leads to significant performance improvements. These findings lead to an improved characterization of the system and can be useful for the optimal design of EH devices. Moreover, we outline future research directions with the ultimate goal of realizing high-performance networks of numerous harvesters in real-world environmental conditions.

Preface

The present Doctoral Thesis deals with the theoretical, numerical and experimental analysis of a specific aeroelastic system with the ultimate goal of extracting energy from laminar fluid flows exploiting a flutter-like instability.

The work has been carried out during the three years of the XXXII cycle (A.Y. 2016-2019) of the Ph.D. program in "Fluid Dynamics and Environmental Engineering" at the Department of Civil, Chemical and Environmental Engineering (DICCA) of the University of Genoa (IT).

After the dissertation on the aforementioned subject, a short report is included on complementary research that has been carried out during this three-year period.

Finally, the related scientific production (i.e., papers on peer-reviewed journals and communications at conferences and other events) is presented.

Contents

List of Figures

List of Tables

A mio padre

Chapter 1

Introduction

Aeroelastic phenomena represent a longstanding issue in the history of aeronautical and civil engineering. In the design of aircraft, bridges or tall buildings, many efforts have been devoted to their understanding, in order to suppress the source of potentially catastrophic failures or control issues [5, 6, 37]. In this kind of fluid-structure interaction (FSI) problem, the dynamics of elastic structures and fluid flows are fully coupled, leading to peculiar phenomena such as the *self-sustained* oscillation experienced by fluttering wings or bluff bodies [78, 79].

More recently, however, an increasing interest can be noted toward these same phenomena, but with the purpose of exploiting the underlying mechanisms to extract energy from the wind or marine currents [1, 45, 48]. Specifically, the development of efficient *energy harvesting* (EH) techniques is rapidly gaining importance as an innovative way for the autonomous supply of low-power sensors, which have numerous and promising applications, e.g. in environmental monitoring activities.

The present work concerns this latter framework by focusing on the investigation of a novel concept for aeroelastic EH based on elastically-bounded flapping plates. Before introducing the subject and the research objectives, we briefly recall classical concepts of aeroelasticity and review the increasing literature on FSI-based EH techniques, along with their potential application in emerging technologies.

1.1 Background

Several attempts of defining and classifying aeroelastic instabilities have been made by many researchers since the end of Second World War. A well-known classification was

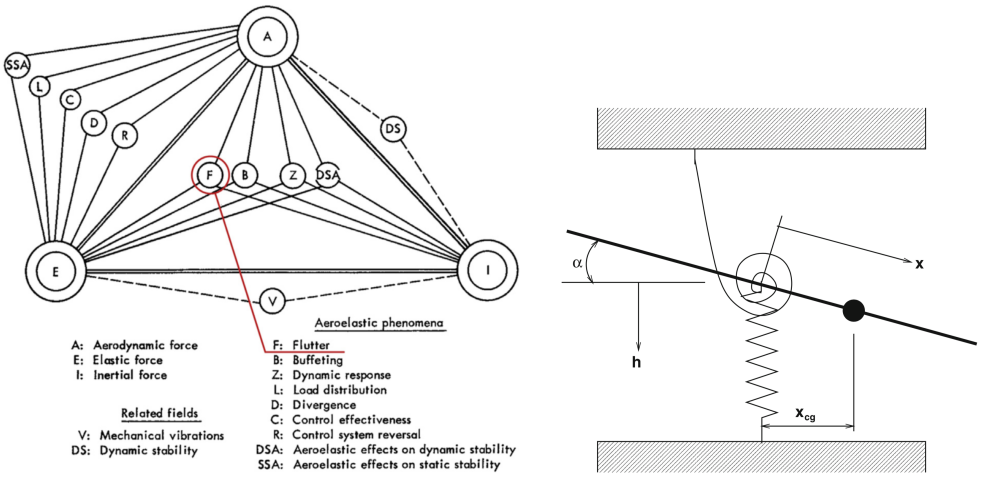

(a) (b)

FIGURE 1.1: (a) Collar's triangle of aeroelasticity (red line underlining flutter), reproduced from Ref. [48]. (b) Typical airfoil model for coupled-mode flutter, reproduced from Ref. [24].

first proposed by Collar [19] by means of a conceptual triangle between inertial, elastic and aerodynamic forces (reproduced in Fig. 1.1a), and then accepted by classical textbooks [5, 24]. Collar's classification is rather comprehensive and, in particular, points out the distinction between static and dynamic aeroelastic phenomena.

For the sake of energy extraction, we are concerned with the latter, for which a further classification can be made following Blevins [6]. Classical aeroelastic instabilities are, in particular, associated with steady flow interacting with structures having some degrees of freedom (DoFs). In this regard, we can have different mechanisms such as *flutter*, *galloping* and *vortex-induced vibration* (VIV). While flutter is associated with slender aerodynamic bodies such as wings or airfoils, galloping and VIV are typical of bluff bodies such as circular or prismatic cylinders.

On the other hand, McCarthy et al. [48] recently reviewed an alternative classification of flutter, aiming at unifying the overall framework, by distinguishing between (i) *moviment-induced excitation* (MIE) and (ii) *extraneously induced excitation* (EIE). Following McCarthy et al. [48], MIE is defined as a self-excited bending instability occuring above a certain critical flow velocity. Therefore, it includes what are commonly referred to as flutter instabilities. Conversely, EIE is defined as the interaction between a structure and an external time-varying flow. According to McCarthy et al. [48], EIE also includes VIV, although it should be noted that vortex shedding is a phenomenon caused by the fluid-structure interaction itself and not properly an external forcing.

Regardless of the particular kind that is considered, the common feature among all aeroelastic instabilities is that the mutual and nonlinear interaction between the

fluid and structural dynamics leads to a variety of nontrivial dynamical states, ranging from stable to chaotic ones and including the emergence of self-sustained *limit cycle oscillations* (LCOs) of regular and finite amplitude. From the EH perspective, the latter clearly deserves the major attention and have been the subject of many investigations devoted to their exploitation for energy extraction [1].

1.1.1 Aeroelastic flutter

Since this work concerns an energy extraction concept essentially based on flutter, we review in more detail this particular aeroelastic instability. More precisely, several kinds of flutter can be identified, depending on the number of active modes that are involved in the motion and/or the flow features (e.g., separated or attached): *stall* flutter is thus characteristic of 1-DoF systems where flow separation is occurring, whereas for 2-DoFs systems and attached flow we have what is commonly referred to as classical, or *coupled-mode*, flutter. Note, however, that this provides only an approximate classification since the same problem may involve the overlapping of such mechanisms, as for example in the postcritical stage of coupled-mode flutter where flow separation typically occurs and is actually one of the main causes of the resulting LCOs [3, 70].

Let us start by focusing on the framework of classical flutter where two modes, i.e. bending and torsion, are considered. Fig. 1.1b sketches the typical airfoil model as introduced by Dowell [24], where a streamlined body is allowed to translate in the vertical direction and rotate around an elastic axis parallel to the spanwise direction. The first DoF is denoted as *plunge* and mimicks the effect of bending on a generic section of the wing in terms of the linear displacement h. The second DoF, typically named as *pitch*, is related with torsion and is quantified by the rotation angle α.

In classical flutter theory, structural elasticity is included for both DoFs: for plunge we have a linear spring with stiffness K_h, while for pitch we have a torsional spring with stiffness K_α. The governing equations for such 2-DoFs system thus read [5]:

$$m\ddot{h} + S_\alpha \ddot{\alpha} + K_h h = -L, \tag{1.1a}$$

$$S_\alpha \ddot{h} + I\ddot{\alpha} + K_\alpha \alpha = M, \tag{1.1b}$$

where m is the mass of the airfoil, I its moment of inertia with respect to the elastic axis, L is the lift force and M is the aerodynamic moment. Similarly to what is done in vibration analysis, the *uncoupled* natural frequencies of the two modes can thus be derived: for the plunge motion (or bending mode) we have $\omega_h = \sqrt{K_h/m}$, whereas for the pitch (or torsion mode) we have $\omega_\alpha = \sqrt{K_\alpha/I}$.

Standard treatment of flutter features assuming simple harmonic motion, so that the solution of Eqs. (1.1) can be expressed as:

$$h = \bar{h}_0 e^{i\omega t}, \tag{1.2a}$$

$$\alpha = \bar{\alpha}_0 e^{i\omega t}, \tag{1.2b}$$

where $\bar{h}_0$, $\bar{\alpha}_0$ and ω are in general complex numbers.

Focusing on the aerodynamic force L and moment M, deriving their expression as a function of the wing motion (i.e. h and α) in the unsteady case with finite displacements is generally what gives rise to the complexity of the problem. Early attempts of predicting the onset of flutter relied on a linear approach, such as the one by Theodorsen [84] providing an aerodynamic theory for oscillating airfoils at small (i.e., infinitesimal) angles of attack. Exploiting Theodorsen's theory, along with using Eqs. (1.2) into Eqs. (1.1), leads to an eigenvalue problem by solving which an expression for the critical velocity U_{F} and frequency ω_{F} can be obtained, at which the instability gets triggered [5].

For $U > U_{\mathrm{F}}$, the interaction between the two modes is such that the energy transfer occurs from the flow to the structure. Moreover, the plunge and pitch frequencies are found to merge when approaching this critical condition. In this linear framework, however, the oscillation is amplified exponentially in time, thus diverging. Although they provide a crucial indication for avoiding the onset of the phenomenon, linear theories are not capable of reproducing the so-called *post-critical* stage of the instability, where oscillations become of finite amplitude and the interaction gets essentially nonlinear [24]. Indeed, for capturing the limit-cycle oscillations typically observed in experimental tests or numerical simulations, nonlinear approaches have to be considered.

Besides improving the physical understanding of flutter, the need of such approach is related at least to two other motivations. On one hand, a more advanced design of aircraft wings and control surfaces, where aeroelastic phenomena can be controlled and somehow exploited, could improve the flight performance or structural aspects [37]. On the other hand, it is driven by exploring the possibility of capturing the energy of fluid flows (as it will be done in this work). This could be used not only for EH and the consequent supply of low-power sensors, but also for proposing new, unconventional renewable energy generation systems [93].

Researchers have initially considered the effect of structural nonlinearities, representative of loose linkages or other constructive aspects, by means of using cubic or hysteretic constitutive laws in place of a linear Hooke constraint [42, 23]. Aerodynamic nonlinearities were first tackled mainly by focusing on transonic flow conditions, since linear expressions for forces and moments were found to be poorly accurate. In

low-speed, subsonic regimes, however, nonlinearity is relevant in the presence of flow separation. This is not only the case of 1-DoF stall flutter, but also for the postcritical stage of coupled-mode flutter. It is therefore evident how, in the general case, several types of flutter may actually co-exist.

More recently, several studies have investigated the postcritical stage of flutter by means of experimental wind-tunnel measurements. Among the numerous contributions, Dimitriadis and Li [22] focused on stall flutter of a NACA 0012 airfoil section characterizing the associated bifurcations, while Razak et al. [74] extended the analysis to the pitch-and-plunge model. Other works focused on the same 2-DoFs arrangement but considering flat plates with rectangular cross section instead of airfoils [3, 68, 70]. Overall, these studies report on the existence of LCOs of finite amplitude also for classical flutter.

Numerical investigations were also carried out essentially focusing on the same configurations. Early attempts were based on inviscid flow modeling and mostly interested in nonlinear effects associated with transonic phenomena [42]. With advances in the feasibility of full Navier-Stokes flow computations, the access to intrinsically viscous phenomena, such as the formation of leading edge vortices (LEVs), became possible [71]. In this regard, reduced-order modeling attempts were also proposed, such as vortex-lattice methods based on intermittent release of leading-edge vortices [72].

Nevertheless, one can note the relatively surprising lack of contributions on flutter instabilities in low-Reynolds flow conditions. In fact, although being of scarce relevance for more conventional aeronautics or civil engineering, this regime is actually concerned by intriguing topics such as the design of biomimetic micro-aerial devices, as well as that of small-scale EH devices [51, 54].

1.1.2 Flutter-based energy harvesting

Focusing on the framework of flow-induced EH, the significant number of review papers that have been recently appeared in this context testifies the increasing relevance of the topic [93, 92, 31, 1, 45, 48].

Among the various flutter-based EH systems, one can include those based on flapping flags [83, 52, 80] as well as passively flapping airfoils [92, 93]. For the latter, the motion of an essentially rigid, streamlined body is limited to a certain number of degrees of freedom (DoFs), typically two: translation along the transverse direction (*plunge*) and rotation around a spanwise axis (*pitch*).

Focusing on fully-passive systems (i.e., where the dynamics is entirely governed by the fluid-structure interaction, without any prescribed kinematics), early research by Peng and Zhu [65], conducted by two-dimensional numerical simulations, highlighted the variety of possible flapping states and provided a first estimate of the resulting

power and efficiency. These findings were confirmed and enriched by further computational studies in closely comparable conditions [97, 91] as well as rather different systems, e.g. with different cross sectional shapes and/or operating at higher-Reynolds regimes [94, 88, 72, 90].

Young et al. [94] introduced a configuration where the pitch and plunge motions are constrained by a mechanical linkage along with pitch control in order to increase the performance. Veilleux and Dumas [88] performed an optimization study for a fully-passive device by two-dimensional CFD simulations, which became the basis for the experimental prototype later presented by Boudreau et al. [12]. These studies agree in reporting that the performance is improved for an adequate synchronization between the two DoFs and in case of nonsinusoidal pitching motion. Wind-tunnel investigations were reported by Pigolotti et al. [69, 68, 70] considering a flat plate in a classical pitch-and-plunge arrangement and exploring systematically the effect of several physical parameters on the flutter onset and the nonlinear oscillations in the postcritical regime. A nearly identical system was considered in the work by Wang et al. [90] where two-dimensional computations were performed in order to characterize the dependence of limit-cycle oscillations with respect to the governing parameters, initial conditions, spring nonlinearity and extraction (modelled by viscous damping).

Besides the development of the individual energy harvester and the consequent understanding of the associated aeroelastic system, one can look at scaling the total extracted power by assembling a network of multiple energy harvesters. Following this perspective, however, a further degree of complexity arises since the behavior of each device in the network will be coupled with those of others by means of nonlinear mutual interactions, leading to substantial alterations of the resulting dynamics compared to that investigated in the individual case.

Among the few contributions on multiple devices for EH application, Bryant et al. [17] tested devices made by a rigid airfoil hinged on a cantilevered flexible beam and arranged in in-line or staggered configuration, reporting performance improvements for downstream devices by virtue of the beneficial effect of wake forcing. Moreover, it was later proposed that such effect can be controlled by tuning the pitching stiffness of downstream devices [38]. McCarthy et al. [47, 49] focused on the in-line arrangement considering a different flutter-based system where a triangular leaf is joined to a piezoelectric stalk by a revolute hinge. They reported increases in power of about 40% for the downstream device caused by the interaction with the horseshoe cone vortex released by the upstream device. Finally, several studies focused on multiple filaments (in 2-D) or flexible plates (in 3-D) placed in the side-by-side configuration, showing that oscillations can increase with respect to the single case if the distance between the flapping objects was within an intermediate range [95, 26, 35].

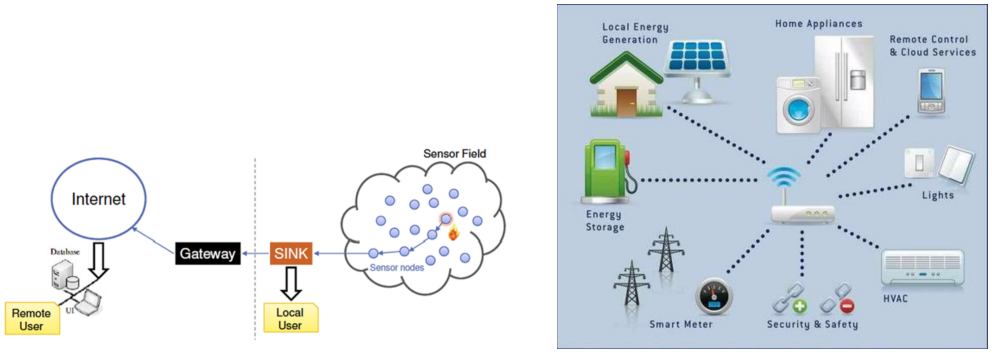

(a) (b)

FIGURE 1.2: (a) Schematic representation of WSN, reproduced from Ref. [73]. (b) Examples of WSN applications in the IoT framework, reproduced from Ref. [21].

1.1.3 Application to wireless sensor networks

Among the numerous progresses of electronics in the last decades, one is the development of low-power (or ultra-low-power) devices. Combined with the success of communication technologies, the key concept of *wireless sensor network* (WSN) has emerged and gained rapidly the attention of many researchers and investors [73].

Fig. 1.2a illustrates schematically how WSNs typically work: a multitude —even hundreds or thousands— of sensor nodes are deployed in a certain region, being able to communicate between them and send the acquired data to one, or few, sink nodes which collect the information and act as a global sender/receiver to/from a remote server.

The potential applications of WSNs range from environmental to military ones and from healthcare to smart industry. Examples include ecological monitoring, hazard detection (e.g., fire, flood, hurricane, earthquake), precision agriculture and search-and-rescue activity [2].

WSNs may be placed in remote locations with difficult or dangerous access, thus posing significant issues regarding their power supply. In fact, the use of replaceable batteries is often not feasible, and the need of autonomous powering turns out to be crucial. This requirement can be satisfied by equipping the nodes with an embedded energy harvesting system that is capable of converting energy from ambient sources. Typically, the EH system shall be capable of providing a relatively small electrical power, typically $\mathcal{O}(\mathrm{mW})$ or even below.

Among the available sources for EH, one can include vibrational, electromagnetic, solar and thermal [30]. The present work concerns, in particular, with harvesting from fluid flows, such as wind or water currents, exploiting fluid-structure interaction mechanisms.

WSNs can also be classified depending on the environment in which they are intended to operate (e.g., terrestrial, underground, underwater), posing specific features and constraints. However, some general requirements can be outlined. For the single nodes, it is typically required to have a low production cost and a small size. For the overall network, the following criteria can be listed: fault tolerance, self-reconfigurability, cooperativity between nodes [73].

Additionally, the outlined framework can be generalized within the new technological paradigm that has been defined as the *Internet of Things* (IoT), where physical devices are able to measure, communicate and operate in a radically innovative way, opening to countless applications as sketched in Fig. 1.2b [28]. Such a groundbreaking evolution has become possible, on one hand, in light of the advances achieved in low-power/low-cost electronics. On the other hand, the rapid growth of data-driven modeling techniques has highlighted the potential of exploiting large amounts of information collected by a widespread distribution of sensors. According to the European Commission, the number of IoT connections within the EU is estimated to increase from approximately 1.8 million in 2013 to almost 6 billion in 2020, leading to the EU IoT market being higher than one trillion euros by 2020 and consistently the global energy harvesting market, valued at EUR 1.2 billion in 2014, has been anticipated to reach EUR 2.63 billion by 2020 [21].

1.2 Subject of the present work

This work concerns a particular flutter-based energy harvesting system (which will be described in more detail in Chapter 2) featuring elastically-bounded plates interacting with laminar flow, originally proposed by Boragno et al. [11]. The system is characterized by a fluttering instability giving rise to finite-amplitude limit cycle oscillations (LCOs) and flapping motions, from which energy extraction can be performed, e.g., by means of electromagnetic coupling. In this work, in particular, we will mainly focus on deepening the comprehension of its purely aeroelastic behavior.

At a first glance, this physical system resembles the pitch-and-plunge model that we have reviewed in the preceding section. Indeed, the occurring aeroelastic instability could be associated with coupled-mode flutter. However, remarkable differences exist with respect to classical flutter, the main one being the absence of any torsional restraint on the rotation, i.e. $K_\alpha = 0$. Consequently, despite the substantial similarities this yields distinctive features such as, e.g., in the critical condition for the onset of self-sustained flapping (as it will be discussed in Chapter 4). On the other hand, this case represents a singular limit for which classical flutter theory does not apply in a straightforward manner.

Related to this topic, Boragno et al. [11] were the first introducing the concept and presenting a first configuration of experimental devices. They provided wind-tunnel measurements highlighting a variety of different flapping states that elastically-bounded wings could experience (e.g., stable, periodic or chaotic), depending on the combination of anchor point and center of mass positions. Moreover, they also proposed a first comparison with numerical simulations and a preliminary indication of the potential energy extraction.

Following this study, Orchini et al. [64] addressed the identification of the critical threshold for sustained flapping in the framework of a two-dimensional model. To this aim, they resorted to a linear stability analysis exploiting Theodorsen's theory, i.e. considering inviscid flow and small perturbations. The prediction by the theory was then corroborated by two-dimensional numerical simulations featuring overlapping grids for handling with the moving wing. Several features of the system were highlighted exploring the variety of flapping states while varying the main governing parameters (i.e., mass density ratio, spring elastic constant, pivot point position), including the existence of another flapping instability in the limit case of infinite spring stiffness.

Despite these previous studies, several points remain largely unexplored which are of key interest, both for the optimal design of EH devices and improving our comprehension of this aeroelastic system.

The first open issue is the identification of the flapping threshold in a framework closer to the real situation. In fact, the analysis by Orchini et al. [64] holds for the two-dimensional case and very high Reynolds numbers. However, we actually deal with three-dimensional and finite-Reynolds-number flows. The question that arises is whether it is possible to derive a different prediction of the flapping onset, which has to be more reliable in this latter framework.

For the purpose of energy extraction, we are mostly interested in the postcritical regime characterized by regular LCOs, for which we have an easier design of the conversion apparatus and a more constant harvested power. In this regime, the goal is thus to maximize both the amplitude and frequency of the oscillation, and in turns the mechanical power harvested by the flapping plate. The knowledge on this aspect, however, is rather limited and mainly based on experimental evidence. The second issue thus regards how we can understand the essential role of the various governing parameters (e.g., geometry and mass distribution) on the flapping dynamics, therefore obtaining useful indications for optimizing the device.

Finally, for the sake of scaling the harvested power we can think of considering not just one but many devices, i.e. considering the potential of EH networks (or arrays) of elastically-bounded flapping plates. A new degree of complexity will be introduced in the problem: on top of the fluid-structure interaction experienced by the single

device, new nonlinear and mutual interactions between the different flapping objects will exist, causing a substantial alteration of the behavior observed in the single case.

To tackle the problem in an effective way, our study will be characterized by a twofold approach: on one hand, seeking to capture the essential physics, we will consider a simplified and idealized model (which will form the basis both for theoretical developments and numerical simulations); on the other, we will also consider several configurations of the real energy harvester (that will be experimentally tested by means of wind-tunnel measurements, and later compared with a reduced-order mathematical model).

1.2.1 Research objectives

Having discussed the points deserving our main interest, the objectives of the present work can be summarized as:

1. Identify the critical condition for self-sustained flapping motions of elastically-bounded plates in a general and representative framework.

2. Characterize the postcritical behavior of (single) flapping plates, focusing on how to maximize the EH potential of regular limit-cycle-oscillation regimes.

3. Investigate the possibility of combining multiple devices in array configurations, assessing the convenience for EH application.

1.2.2 Thesis' outline

Following this introduction, the rest of the work is structured as follows:

Chapter 2 gives first an overview of the experimental energy harvester based on elastically-bounded plates, and then introduces our idealized model, along with defining the characteristic parameters governing the system.

Chapter 3 describes the different methodologies that were used in this research: (i) fully-resolved Navier-Stokes direct numerical simulations; (ii) wind tunnel experimental analysis; (iii) quasi-steady phenomenological modeling.

Chapter 4 addresses Objective 1 by proposing a predictive theory for the critical condition for self-sustained flapping, that is corroborated by both numerical and experimental results.

Chapter 5 investigates the postcritical regimes where regular limit-cycle oscillations occur (Objective 2), focusing on how to essentially reproduce the same dynamics observed in the experiments, along with presenting the description by means of the quasi-steady phenomenological model.

Chapter 6 explores the dynamical behavior and EH potential of arrays of multiple devices for several basic arrangements, addressing Objective 3. A parametric study is conducted by means of numerical simulations and the appearance of a constructive interference mechanism is confirmed by wind-tunnel experiments in a complementary way.

Finally, Chapter 7 summarizes the main results and outlines the possibility for future developments.

Chapter 2

Physical problem

Having outlined the general framework of the present work, this chapter presents in more detail the subject that will be investigated. First, we supply a description of the experimental device for aeroelastic energy harvesting. Then, we present the mathematical model that is able to capture the essential dynamics of interest, discussing the related assumptions and introducing the main parameters governing the problem.

2.1 Experimental device

As already mentioned in Sec. 1.2, the aeroelastic system under consideration is represented by a rigid plate that is elastically anchored to a fixed frame, e.g. using linear springs or elastomeric elements, and invested by a laminar fluid flow. The plate is characterized by its geometrical parameters (i.e. chord c, thickness δ and span s) and mass m, and can be considered to be essentially rigid. The elasticity of the structure is concentrated in the anchoring elements and can be generally quantified by an overall stiffness K. This structure is invested by an incompressible laminar flow, which is characterized by the freestream velocity U and by the fluid properties, i.e. density ρ_{f} and kinematic viscosity ν.

Fig. 2.1a gives a schematical side view of the system, introducing the two main degrees of freedom, i.e. the transverse (or plunge) displacement y and the pitching angle θ. Based on this concept, experimental devices of centimetric size have been realized, such as the one shown in Fig. 2.2. In this case, the wing is made by a polyvinyl acetate foil, glued to a polymeric 3D-printed tube, and it is free to rotate around a brass rod (i.e. the *pivot* axis). This latter is fixed at its ends to a pair of

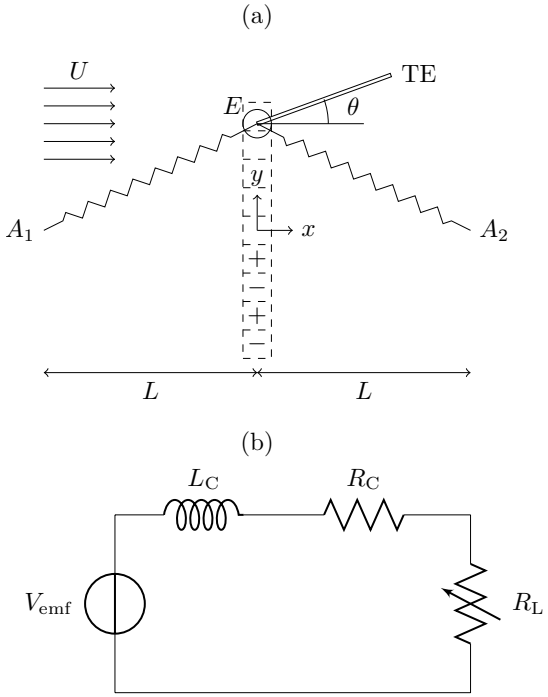

FIGURE 2.1: Schematisation of the system: (a) the elastically bounded wing (E denotes the pivot point, θ the pitching angle, TE the trailing edge; L is the initial elastomer length and A_i are the elastomer anchorage points) with coils (moving with the pivot point E) and fixed magnets placed with alternated polarity, invested by a uniform fluid flow of unperturbed velocity U; (b) electrical circuit for energy extraction: V_{emf} is the electromotive force generated by Faraday effect, L_{C} and R_{C} are the internal coil inductance and resistance, respectively, and R_{L} is the applied resistive load.

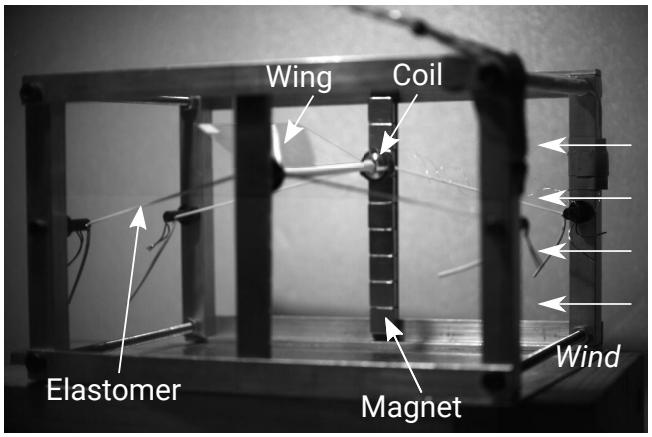

FIGURE 2.2: Experimental prototype based on the elastically-bounded wing concept and equipped for EC extraction. Photograph from wind tunnel experiments, while the wing is undergoing the flapping motion when invested by incoming uniform flow.

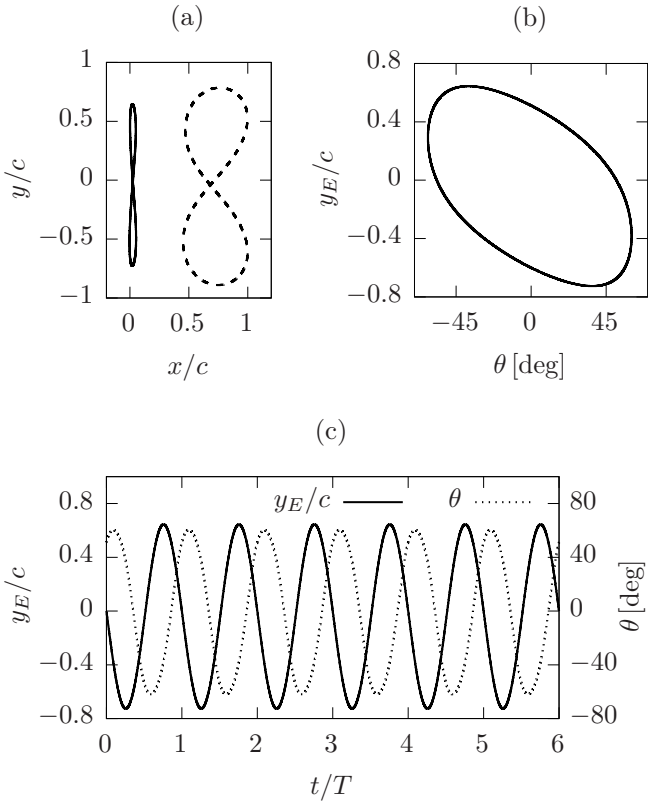

FIGURE 2.3: Flapping kinematics associated with the experimental prototype for unperturbed wind velocity $U = 4\text{m/s}$ and applied load resistance $R_\text{L} = 1\text{k}\Omega$: (a) pivot point (solid line) and trailing edge (dashed line) trajectories, from a lateral view; (b) pivot point vertical oscillation versus the pitching angle; (c) time histories of pitch (dotted) and plunge (solid) degrees of motion. Lengths and time are normalized with the wing chord and flapping period, respectively.

3D-printed supports (hosting the coils needed for energy conversion) and is connected to four elastomeric elements made of polyisoprene and arranged parallel to the wind direction.

In the presence of incoming flow and if the parameters (i.e.: geometry, mass, elastic constant, wind velocity) are within a proper range, an aeroelastic instability occurs, leading to self-sustained limit cycle oscillations (LCOs), as reported in Fig. 2.3 for a representative situation. The wing performs a regular flapping motion, with the pivot point (i.e. the trace of the pivot axis in a lateral view) undergoing a substantially vertical trajectory, along with periodic stretching and relaxing of the elastomers. Note that, although in the presented layout all the motion degrees of freedom are allowed in principle, the resulting displacement of the pivot point in the streamwise direction is almost negligible, as for rolling and yawing rotations. Indeed, this configuration is designed to obtain, within a specified wind velocity range, a regular flapping regime among the possible ones (which may also include, e.g., chaotic states) [11].

In this configuration, the wing has the following geometry: chord $c = 35$mm, span $s = 85$mm and thickness $\delta = 100\mu$m. The mass of the wing (foil + rod) is $m_{\mathrm{w}} \approx 1.0$g, while the total mass of the system (wing, axis, supports and elastomers) is $m \approx 5.0$g. The measures of the supporting frame are 10cm × 12cm × 17cm. The four elastomers have circular cross-section with diameter $D_0 = 1.2$mm and length $l_0 = 50.3$mm, at rest; they are pre-stretched so that the initial length is $L = 73$mm. The pivot axis is set at $0.1c$ from the leading edge. For this kind of material, the elastic force magnitude for each elastomer can be modelled as [75]

$$|F_{\mathrm{el}}| = GA_0(L/l_0 - (l_0/L)^2), \tag{2.1}$$

where $G = 0.534$MPa is the material shear modulus and $A_0 = \pi D_0^2/4$. The natural frequency of the system (associated with the vertical motion) can be measured from the free oscillation after perturbing the wing in still fluid, yielding $f_{\mathrm{n}}^{(y)} = 12.8$Hz.

From the resulting LCO, energy conversion can be realized by means of electromagnetic coupling (EC) between a pair of coils placed at the two ends of the pivot axis and two bars of magnets with alternated polarity, as shown in Fig. 2.1a and Fig 2.2. The physical principle underneath this strategy is the electromagnetic induction described by the Faraday-Neumann-Lenz law: because of the relative motion between the coils (moving with wing) and the magnets (which are fixed), the magnetic flux enclosed by each coil varies in time and therefore an electromotive force is generated. The coils are connected in series to an external circuit, such as the one sketched in Fig. 2.1b, where a variable resistive load R_{L} can be inserted. The mean dissipated power over the applied resistance is then evaluated as $P_{\mathrm{out}} = V_{\mathrm{rms}}^2/R_{\mathrm{L}}$, where V_{rms} is the root mean square of the measured voltage.

Fig. 2.4a presents the obtained power for different values of the flow velocity, ranging from 2 to 4 m/s. At $U = 2.5$m/s the maximum power (reached for $R_{\mathrm{L}} = 10\mathrm{k}\Omega$) is nearly 1mW, representing an already interesting amount for supplying low-power sensors. The power level then increases with the flow velocity while the value of the optimal load decreases. The maximum P_{out} varies monotonically as shown in Fig. 2.4b, reaching the highest amount of 14mW at $U = 4$m/s.

To quantify the performance of the device, a comparison can be made with other aeroelastic energy harvesters recently proposed in literature [16, 13, 46, 39, 81, 96]. Fig. 2.5 collects these data in terms of the ratio between the output power and the swept area, as a function of the wind speed [48, 1]: for our device, at $U = 4$m/s, we have $P_{\mathrm{out}}/A_{\mathrm{swept}} \approx 0.27\mathrm{mW/cm^2}$. If we consider instead the power per planform area, we obtain $P_{\mathrm{out}}/A_{\mathrm{wing}} \approx 0.47\mathrm{mW/cm^2}$. Looking at these results, our system collocates in an interesting position with an efficiency close to that of microturbines [13]. Besides, we confirm the competitivity of flutter-EC-based harvesters [48].

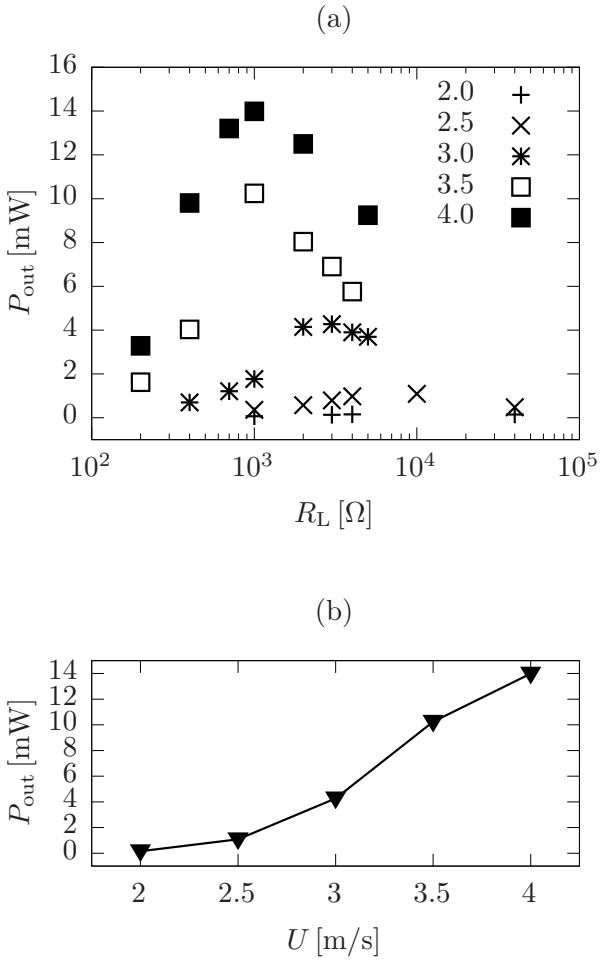

FIGURE 2.4: (a) Mean output power measurements for the experimental prototype as a function of the external electrical load, for different flow velocities (values in legend are given in [m/s]); (b) maximum output power obtained by the experimental prototype as a function of the flow velocity (taken at the corresponding optimal resistive load).

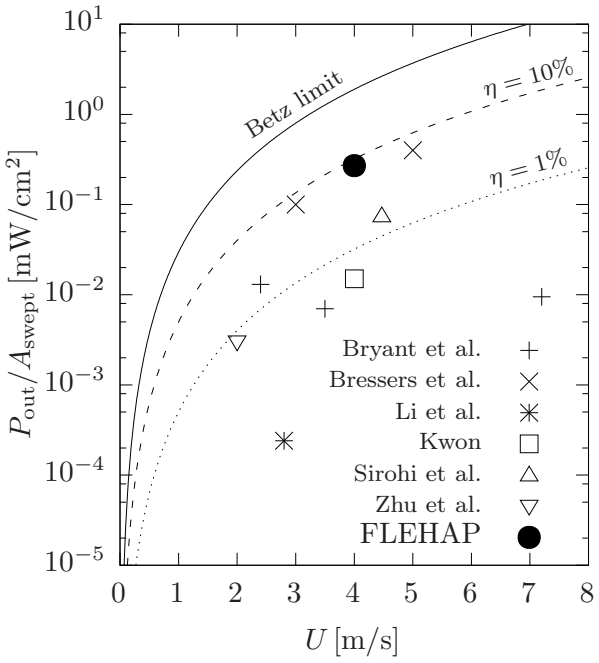

FIGURE 2.5: Performance comparison between our prototype (filled black circle) and other energy harvesters proposed in literature [16, 13, 46, 39, 81, 96] in terms of output power per swept area versus the wind velocity. Curves of constant efficiency are based upon Eq. (5.6), with the Betz limit corresponding to the theoretical limit nearly 59.3%.

In light of these findings, the aeroelastic system under consideration appears to be promising for EH applications. Overall, the aim is to develop competitive EH devices of centimetric size to extract $\mathcal{O}(\text{mW})$ electrical power by exploiting low wind conditions (i.e. $U < 5\,\text{m/s}$), in order to supply low-power microprocessors such as those employed in wireless sensor networks.

Among its features, we highlight that the system is completely passive, without any control mechanisms acting on the wing motion, as it is for active or semi-passive EH systems [93]. Furthermore, the constructive layout is rather simple, with a potential benefit from the cost viewpoint. However, the resulting dynamics is completely governed by the occurring fluid-structure interaction, so that the physical understanding of the latter turns out to be crucial for the design of the energy harvester.

To give an overall description of the possible flapping states, Fig. 2.6 shows the resulting motions for a centimetric-size device while varying both the incoming flow velocity and the elastomer equivalent stiffness $\mathcal{K}_{(y)}^{\text{eff}}$ (this quantity will be properly introduced in Sec. 4.1.1). Here, the elastomers are placed orthogonal to the wind: although this arrangement is not the most suitable when employing an electromagnetic coupling, a rich variety of flapping regimes is revealed. Looking at the reported trajectories, several observations can be made:

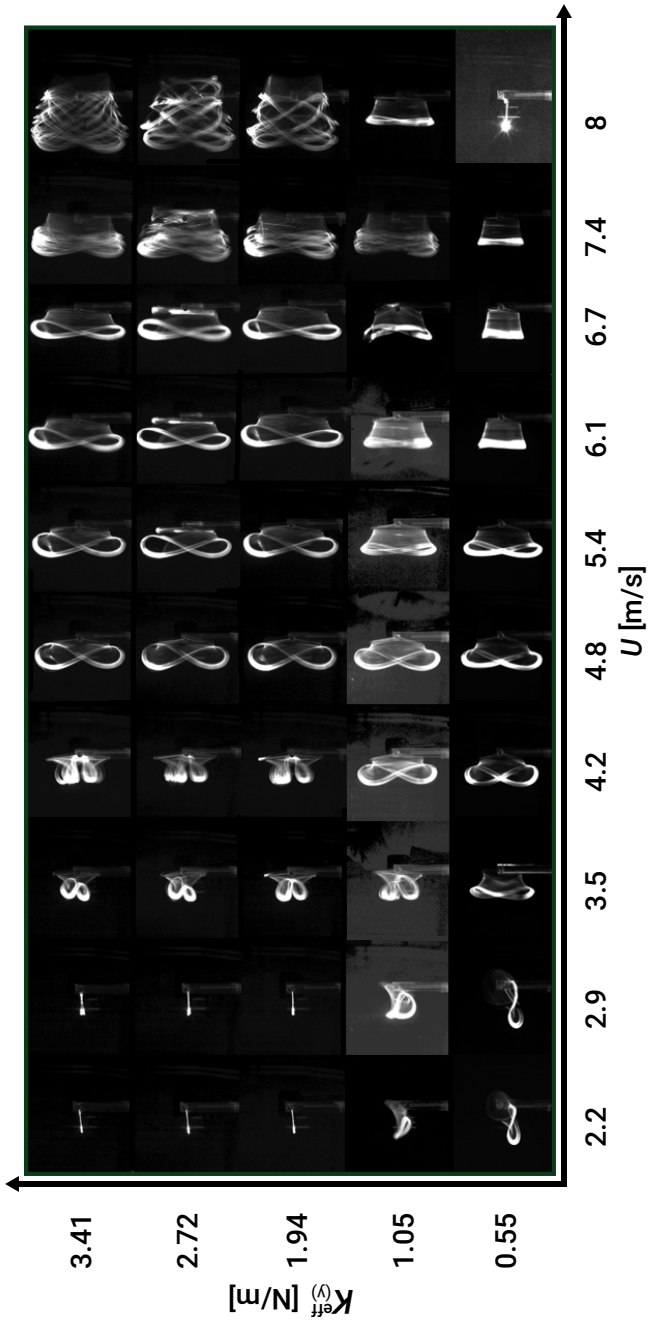

FIGURE 2.6: Wing motion regimes as a function of flow velocity (horizontal direction) and elastomer equivalent stiffess (vertical direction; see Sec. 4.1.1 for its definition). The wind is flowing from the right to the left. Trailing edge and pivot point trajectories are acquired by a digital camera with long-time exposure (more information about the experimental method are given in Sec. 3.2).

1. The aeroelastic instability occurs only if the flow velocity is above a critical value, that we will denote as U_{cr}, otherwise the wing tends to align with the flow reaching a stable and essentially steady state. This onset condition appears to depend on the value of the elastic constant: as an example, at 2.9m/s, for $\mathcal{K}^{\mathrm{eff}}_{(y)} \leq 1.05\mathrm{N/m}$ flutter is triggered, while for larger values we are still below the critical threshold.

2. If one increases the flow velocity beyond U_{cr}, for all the reported cases the wing enters a regular flapping regime characterised by limit cycle oscillations. The trailing edge trajectory rapidly changes its shape and the amplitude increases with U up to a value which is comparable to the chord size. We highlight how the flow velocity corresponding to this maximum in amplitude varies with $\mathcal{K}^{\mathrm{eff}}_{(y)}$. On the other hand, it can also be noted how the flapping amplitude does not vary significantly with $\mathcal{K}^{\mathrm{eff}}_{(y)}$.

3. Up to a certain wind velocity, the amplitude of the pivot point trajectory (although not so visible in the figure) is larger than the one of the trailing edge, while for $U > 3.5 \div 4.2\,\mathrm{m/s}$ (depending on the stiffness value) the situation gets opposite. It can be shown that this transitional behaviour corresponds to a significant variation of the phase between the pitch and the plunge motions. Moreover, when the pivot point displacement is maximised, a relative maximum is typically found also for the flapping frequency: even if this aspect is still under investigation, this condition appears as the most efficient for energy harvesting.

4. When increasing further U, the motion regime may vary significantly. At the highest velocities that could be tested ($U = 8\mathrm{m/s}$), two particular behaviours are observed: for the smallest stiffness the system goes back to a stable condition, while for larger values the motion becomes chaotic.

From the EH perspective, both amplitude and frequency of the oscillation must be maximized. Currently, there is a lack of simple analytical models able to predict accurately the nonlinear dynamics of this kind of aeroelastic systems, especially for fully-passive ones and for flapping regimes of interest for EH, characterized by finite-size displacements and large flow separation [3, 70]. Furthermore, the correlations between the numerous governing parameters are not trivial, e.g.: adding mass on the pivot axis increases the amplitude but, at the same time, decreases the flapping frequency, while increasing the elastic stiffness to gain a higher frequency also increases the onset of flapping, i.e. U_{cr}.

Along with the experimental testing here described, computational fluid dynamics (CFD) simulation represents a complementary research tool to tackle the problem and increase our understanding. The first step of any computational strategy is the choice

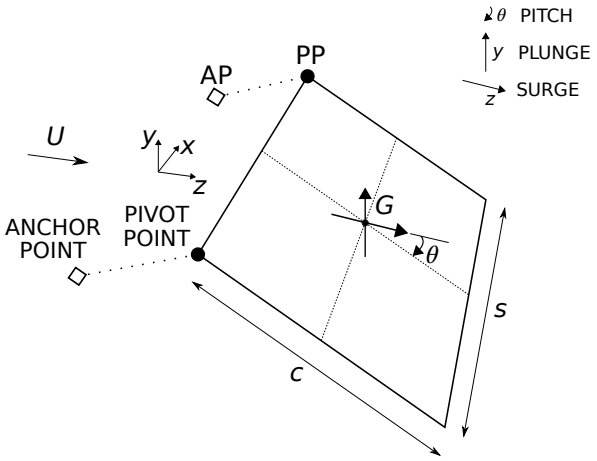

FIGURE 2.7: Sketch of the aeroelastic model considered in the present work.

of a representative mathematical model, i.e. the set of governing equations along the initial and boundary conditions (which are later discretized and solved numerically). In the following section, we introduce the model that will be used for describing our aeroelastic system.

2.2 Aeroelastic model

In this section, we present the mathematical model that will be used in the rest of the work. It will provide the basis for numerical simulations (see Sec. 3.1), as well as represent the framework for elaborating theoretical predictions (see Sec. 4.1). The idea is to consider the simplest model that is capable of capturing the essential physical phenomena that are observed experimentally and that we are mostly concerned with (i.e., onset of the fluttering instability, postcritical LCOs and interaction between multiple flapping plates). Following this line of reasoning, the analysis gets simplified both from the theoretical and numerical standpoint, enabling to disregard the constructive details of the experimental device and, at the same time, providing results of wider validity.

A graphical representation of the model is given by Fig. 2.7. We consider a three-dimensional, rectangular plate whose geometry is characterized by chord c, span s and thickness δ. At first, let us consider the case where the plate is characterized by homogeneous density ρ_s. The mass of such homogeneous plate is $m = \rho_s\, c\, s\, \delta$, with the center of gravity G coinciding with the geometrical center. The plate is assumed to be perfectly rigid, this assumption being motivated by the experiments where the observed deformation is negligible.

The wing is let to move, although it is anchored to the fixed frame by means of two elastic elements. In our case, these are chosen to be linear, massless springs. For

each spring, one end is connected to the plate at the pivot point (PP) and the other one is retained fixed at the anchor point (AP). The elastic force can thus be written following Hooke's law:

$$\mathbf{F}^{\mathrm{el}} = -k(\mathbf{r}_{PP} - \mathbf{r}_{AP}), \tag{2.2}$$

where k is the spring stiffness, while $\mathbf{r}_{PP}$ and $\mathbf{r}_{AP}$ are position vectors for the pivot point and the anchor point, respectively.

We then consider the presence of an incompressible uniform flow with freestream velocity U investing the body. The physical properties of the fluid are the dynamic viscosity μ and the density ρ_{f}.

Next assumption concerns gravitational effects. Although in the experimental evidence this component appears not to be negligible (e.g. causing asymmetrical flapping trajectories), we argue that generally it is not a crucial ingredient for describing the essence of the flapping dynamics. Hence, we choose to suppress the presence of gravity, i.e. $g \equiv 0$, in order to decrease the number of independent parameters and to isolate the aeroelastic interaction. However, one could expect that the importance of gravity effects is proportional to the Froude number, defined as $Fr = gL/U^2$ (where g is gravity acceleration and L a reference length), so that this decreases for higher wind speeds.

Focusing on the purely aeroelastic behaviour, in the present work we do not consider any model of energy extraction. However, predictions on the potential EH performance can be made also in this framework on the basis of the resulting motion and aerodynamic force and moment (see e.g. Ch. 5; indeed, this choice can be intended as equivalent to the open-circuit condition for the real device).

Inspired once again by the dynamics observed for real devices, the plate motion is allowed only with respect to three degrees of freedom (DOFs), i.e.: (i) translation in the streamwise direction (*surge*), (ii) translation in the transverse direction (*plunge*), (iii) rotation around the spanwise axis (*pitch*). Under these assumptions, the rigid body equations governing the motion of the wing center of mass G (whose position is denoted by $\mathbf{r}_G$) and the rotation angle θ read:

$$m\,\ddot{\mathbf{r}}_G = \mathbf{F}^{\mathrm{aero}} + 2\,\mathbf{F}^{\mathrm{el}}, \tag{2.3}$$

$$I_G\,\ddot{\theta} = M^{\mathrm{aero}} + 2\,M^{\mathrm{el}}, \tag{2.4}$$

where m is the mass, I_G is the moment of inertia with respect to G along the spanwise direction x, $\mathbf{F}^{\mathrm{aero}}$ is the aerodynamic force, $\mathbf{F}^{\mathrm{el}}$ is the elastic force exerted by each spring (given by Eq. (2.2)), M_{aero} is the aerodynamic moment and $M^{\mathrm{el}} = (\mathbf{r}_{PP} - \mathbf{r}_G) \times \mathbf{F}^{\mathrm{el}}$ is the elastic one.

The aerodynamic force and moment can be obtained by integrating over the plate surface S the fluid stress tensor:

$$\mathbf{F}^{\text{aero}} = \int_S (\boldsymbol{\tau} \cdot \mathbf{n} - p\mathbf{n}) \, \mathrm{d}S, \tag{2.5}$$

$$M^{\text{aero}} = \int_S \mathbf{r} \times (\boldsymbol{\tau} \cdot \mathbf{n} - p\mathbf{n}) \, \mathrm{d}S, \tag{2.6}$$

where $\boldsymbol{\tau}$ and p are the viscous stress tensor and pressure, $\mathbf{n}$ is the outward normal unit vector and $\mathbf{r}$ is the distance between the generic point of the surface and G.

In order to compute the aerodynamic forces, we will employ a fully-resolving approach, i.e. the fluid flow is modelled by the Navier-Stokes equations that we can write for the incompressible, Newtonian and isothermal case as follows:

$$\rho_{\text{f}} \left(\frac{\partial \mathbf{u}}{\partial t} + \mathbf{u} \cdot \nabla \mathbf{u} \right) = -\nabla p + \mu \nabla^2 \mathbf{u}, \tag{2.7}$$

$$\nabla \cdot \mathbf{u} = 0, \tag{2.8}$$

where $\mathbf{u} = \mathbf{u}(\mathbf{x}, t)$ denotes the fluid velocity and $p = p(\mathbf{x}, t)$ is the pressure, at a certain location in space $\mathbf{x} \in \Omega_{\text{f}}$ (being Ω_{f} the considered fluid domain) and instant t.

Our aeroelastic model is hence composed by combining Eqs. (2.3), (2.4), (2.7) and (2.8). Details on how this set of coupled differential equations is solved numerically will be given in Sec. 3.1. Before proceeding further, however, let us take advantage of a nondimensionalization procedure in order to decrease the number of independent parameters and, consequently, derive the essential quantities that control this kind of FSI problem.

2.2.1 Nondimensional governing parameters

Recollecting the dimensional, independent quantities previously introduced (in the simplest situation), we have $N_q = 8$ parameters: c, s, δ, ρ_{s}, k, U, μ and ρ_{f}.

Let us therefore proceed by transposing our problem into nondimensional form. Considering its purely mechanical nature, the problem involves $N_p = 3$ physical dimensions, i.e. length L, mass M and time T. This number also corresponds to the number of scaling quantities that are needed for nondimensionalization. In our case, we choose to employ the unperturbed flow velocity U, the plate chord c and the fluid density ρ_{f}. With this choice, we can construct the following reference values for length, mass and time: $L = c$, $M = \rho_{\text{f}} c^3$, $T = c/U$.

We start by nondimensionalizing the spatial and temporal coordinates. Note that

in the rest of the work we will always refer implicitly to these nondimensional quantities:

$$(x, y, z) \mapsto (x/c, y/c, z/c), \tag{2.9}$$

$$t \mapsto t/(c/U). \tag{2.10}$$

Next, it follows that the independent parameters in nondimensional form are $N_q - N_p = 5$. Here, we choose: s/c, δ/c, $\rho_\mathrm{s}/\rho_\mathrm{f}$, $k/(\rho_\mathrm{f} U^2 c)$ and $\rho_\mathrm{f} U c/\mu$. However, a further reduction can be obtained by considering the product between the cross-sectional aspect ratio δ/c and the density ratio $\rho_\mathrm{s}/\rho_\mathrm{f}$ instead of the two quantities separately (this new parameter can be seen as a nondimensional surface density of the wing).

To summarize, the following four nondimensional, independent parameters can be defined:

$$\text{Æ} = \frac{s}{c}, \tag{2.11a}$$

$$\rho_\mathrm{w} = \frac{\rho_\mathrm{s}}{\rho_\mathrm{f}} \frac{\delta}{c}, \tag{2.11b}$$

$$K = \frac{2\,k}{\rho_\mathrm{f}\, U^2\, c}, \tag{2.11c}$$

$$Re = \frac{\rho_\mathrm{f}\, U\, c}{\mu}. \tag{2.11d}$$

Let us briefly comment on each of the introduced quantities. The first one, Æ, is the planform aspect ratio and it is purely geometrical. Then, Eq. (2.11b) defines the surface density parameter, ρ_w. Note that both Æ and ρ_w are related with the structure only, and not with the fluid. By multiplying these two quantities, one finds the nondimensional mass of the wing:

$$m^* = \rho_\mathrm{w} \text{Æ}. \tag{2.12}$$

Next, we have the nondimensional stiffness K, as defined in Eq. (2.11c) (where the factor 2 is used to account for both springs). This parameter is the one conceptually associated with the fluid-structure interaction, since it depends both on the structural and flow parameters. In fact, this quantity can also be associated with the reduced velocity typically introduced in aeroelasticity. If we use the classical definition for the latter, i.e. $U_\mathrm{R} = U/(f_\mathrm{n} c)$, it follows that $U_\mathrm{R} \sim \sqrt{m^*/K}$ [6]. Last, the chord-based Reynolds number Re represents a measure of the ratio between inertial and viscous forces in the fluid flow.

Chapter 3

Methods of investigation

In this work, several research methodologies will be combined in a complementary way. Their description is the subject of the present Chapter. First, the numerical approach is introduced in Sec. 3.1. Then, the experimental one is presented in Sec. 3.2. Finally, a reduced-order mathematical model is described in Sec. 3.3.

3.1 Numerical simulations

Let us begin by introducing the computational tool, by means of which the dynamics associated to the aeroelastic model of Sec. 2.2 will be extensively investigated. To this aim, an *immersed boundary method* (IBM) is used to perform fully-resolved numerical simulations of the incompressible Navier-Stokes equations in the presence of multiple moving bodies. We limit ourselves to a rather introductory discussion; for an extensive description of the IB method, see the papers by Iaccarino and Verzicco [36], Mittal and Iaccarino [53], and Peskin [67].

In this class of numerical methods, originally proposed by Peskin [66], the grid on which the fluid flow equations are solved does not conform to the geometry of the solid bodies, unlike what happens in more conventional body-fitted approaches where the no-slip boundary condition is directly imposed. Instead, here the latter is accounted for by introducing an additional forcing in the momentum equations, modeled as a singular source term distribution. Hence, we have an *Eulerian* grid for the fluid and a *Lagrangian* one for the immersed structure. Typically, the Eulerian grid is fixed and can often be a simple Cartesian grid, while the Lagrangian one can move and be of various kind, e.g.: one-dimensional series of points, such as those used for modeling

flexible filaments [79, 26, 76], or two-dimensional surfaces discretized with triangular elements, as done for finite-size spherical particles [86, 14, 82] or flapping flags [33, 43] (the latter is also the case of the present work).

Since the two grids do not coincide, the transfer between the Eulerian and Lagrangian frameworks is typically handled by using a regularized Dirac delta function and performing two characteristic operations: the *interpolation* of Eulerian quantities at the (time-varying) Lagrangian positions and the *spreading* of Lagrangian quantities at the surrounding Eulerian points [67].

While sharing the same basic concept, several types of IB methods have been proposed which differ on the basis of how the boundary conditions on the immersed surface are imposed. Following Mittal and Iaccarino [53], an overall distinction can be made between *continuous* and *discrete* forcing approaches. In the former, that is the approach originally used by Peskin [66], the forcing is included into the governing equations before discretization. Conversely, it is added to the discretized equations in the case of discrete forcing approaches. These can further be divided into *indirect*- and *direct*-forcing methods: since in this work we employ a direct-forcing method [85], let us focus on this particular class, whose first example was proposed by Fadlun et al. [25] for three-dimensional complex geometries with subgrid-scale turbulence modeling. The idea behind direct-forcing IB methods is that the desired value of the velocity is directly imposed on the boundary without any dynamical process (i.e., unlike what is done in continuous-forcing methods) [25]. The resulting advantage is a less restrictive condition on the simulation time step, although numerical oscillations can be observed in case of moving and/or deformable bodies. In order to improve this aspect, an alternative version of this method was proposed by Uhlmann [86] in the framework of particle-laden flow applications, through which a smooth transfer between the Eulerian and Lagrangian quantities forces is obtained. Consequently, Vanella and Balaras [87] generalized the approach of Uhlmann and introduced a different reconstruction method based on a *moving-least-squares* (MLS) interpolation, resulting in a more versatile approach, since the forcing computation is decoupled by the local discretization, that can be used in a wider variety of situations (e.g., either structured or unstructured grids).

We will employ, in particular, the direct-forcing approach recently proposed by de Tullio and Pascazio [85], which is based on a the same concept of Vanella and Balaras [87]. This method has been used for simulating flows with particles and bubbles by Spandan et al. [82]. An overview of this approach along with its specialization to the present problem is given in the rest of the Section. For further information, the reader is referred to Refs. [85, 82].

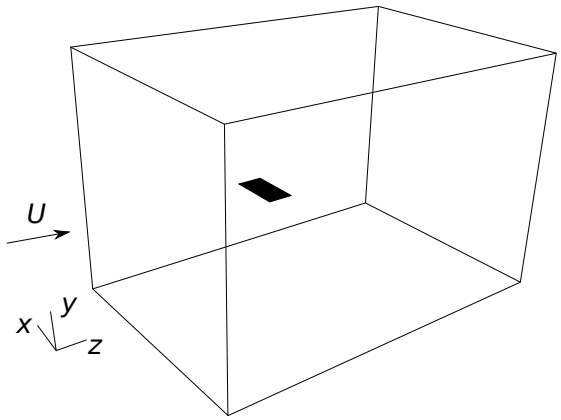

FIGURE 3.1: Sketch of the fluid domain used in the numerical simulations, showing the flat plate in its initial position.

3.1.1 Numerical method

The fluid flow obeys to the incompressible Navier-Stokes Eqs. (2.7) and (2.8) that we can rewrite in nondimensional form as:

$$\frac{\partial \mathbf{u}}{\partial t} + \mathbf{u} \cdot \nabla \mathbf{u} = -\nabla p + \frac{1}{Re} \nabla^2 \mathbf{u} + \mathbf{f}, \tag{3.1}$$

$$\nabla \cdot \mathbf{u} = 0, \tag{3.2}$$

where $\mathbf{u} = \mathbf{u}(\mathbf{x}, t)$ denotes the fluid velocity, $p = p(\mathbf{x}, t)$ the pressure and $\mathbf{f} = \mathbf{f}(\mathbf{x}, t)$ the volumetric forcing. We consider a three-dimensional domain made by a rectangular box of size $L_x \times L_y \times L_z$ (Fig. 3.1), choosing the following set of boundary conditions: the fluid velocity is uniform at the inlet, convective boundary conditions are used at the outlet [27], the top and bottom faces are treated as slip (i.e., non-penetrating) walls, while periodicity is assumed at side faces.

Eqs. (3.1) and (3.2) are solved numerically on a Cartesian grid, with the forcing term $\mathbf{f}$ mimicking the presence of solid bodies. Centered finite differencing is adopted for space discretization using a staggered grid, the overall scheme yielding second-order accuracy. The main iteration loop can be summarized as follows:

- The nonlinear terms are updated explicitly using a second-order Adams-Bashfort scheme.
- The diffusive terms are discretized implicitly with a Crank-Nicolson scheme and an intermediate, nonsolenoidal velocity field is computed by means of an approximate factorization technique for solving the resulting algebraic system [89].
- The correction by the IB forcing is added to the velocity.

- The Poisson equation for enforcing mass conservation is solved and the divergence-free velocity is obtained, together with the pressure field.

Concerning the IB treatment, a direct-forcing approach is used, based on a moving-least-squares (MLS) interpolation to reconstruct the solution nearby the immersed surface [87]. The plate is discretized to a planar surface mesh with N_t triangular elements, their centroids being the Lagrangian markers at which the forcing will be computed by imposing the no-slip condition. For each Lagrangian marker, we consider a support domain enclosing $N_\mathrm{e} = 27$ adjacent Eulerian nodes which are used for the interpolation and spreading operations. Compared with classical IB methods, the adoption of the described method allows to use a larger simulation timestep and to obtain smoother flow solutions and hence aerodynamic forces (for a more complete description, the reader is referred to Ref. [85]).

The numerical procedure has been tested for our physical problem by means of a convergence analysis with respect to the spatial and temporal resolution. Results of this latter and discussion on the choice of grid parameters are collected in Sec. 3.1.2. As a baseline indication, the used domain box ranges from $(-5, -5, -5)$ to $(5, 5, 10)$ and is discretized using a minimum grid spacing $h = 0.02$, with the triangulated meshes discretizing the solid plates having comparable resolution.

3.1.2 Validation

The numerical method used in the present study has been extensively validated for several FSI problems involving both rigid and deformable bodies [85, 82]. For the current investigation, however, we assess the dependency of numerical results on the spatial and temporal resolution. To this end, the chord-based Reynolds number is set to $Re = 1000$, i.e. the highest value tested in the whole study, and the following baseline values for the other control parameters are chosen: $\mathit{AR} = 2$, $\rho_\mathrm{w} = 2$ and $K = 3$. This configuration corresponds to a regular flapping state. A finite initial perturbation on the angular velocity is given in order to shorten the transient, although the achievement of the same steady limit-cycle was verified in case of unperturbed initial condition.

The wing is initially placed with its geometrical center at the origin $(0, 0, 0)$. The domain bounds are set at ± 5 both in the x and y direction, and at -5 and 10 in the z direction. A Cartesian grid is used, with uniform resolution in the spanwise direction and stretched in the other two directions. However, the grid spacing h is made locally uniform in a region close to the wing, i.e. for $-1 < z < 2$ and $-1 < y < 1$. In order to quantify convergence with respect to the spatial resolution, eleven different grids were considered, characterized as shown in Table 3.1. While the same topology is retained, the grids differ by an overall refinement factor. The wing is assumed to have

TABLE 3.1: Grid settings used for convergence study. N_x, N_y and N_z denote the number of nodes in the x, y and z direction, while H and h indicate the maximum and minimum grid spacing, respectively.

Grid	N_x	N_y	N_z	H	h
A	251	84	127	0.4	0.04
B	271	97	147	0.35	0.035
C	334	113	170	0.3	0.03
D	401	136	205	0.25	0.025
E	501	170	257	0.2	0.02
F	541	189	286	0.18	0.018
G	601	213	322	0.16	0.016
H	641	235	353	0.146	0.0146
I	751	258	388	0.133	0.0133
J	865	298	448	0.115	0.015
K	1001	344	516	0.1	0.01

zero thickness and is thus discretized into a surface mesh made of triangular elements whose characteristic length is proportionally adjusted to be essentially equal to the minimum Eulerian spacing h.

The approximate solution can be expressed as a function of grid spacing as follows:

$$f(h) \approx f^* + Ch^p \tag{3.3}$$

where h is the grid spacing, f^* is the exact solution (i.e., the solution that one would have for $h \to 0$), C is a constant and p is the (actual) order of convergence. Instead of fitting the obtained data using this expression, we find more convenient to introduce the relative error with respect to the finest grid (for which $h = h_{\min}$), defined as

$$\epsilon(h) = \frac{f(h) - f(h_{\min})}{f(h_{\min})}, \tag{3.4}$$

since by combining Eqs. (3.3) and (3.4), the following relation can be found:

$$\epsilon(h) = C(h^p - h_{\min}^p), \tag{3.5}$$

where only C and p appear. The fitting is therefore applied to this latter expression, from which we later extrapolate the exact value f^*.

Grid convergence is assessed by considering the amplitude of the transverse oscillation of the pivot point $\mathrm{Amp}(y_{PP})$. Each case is computed up to measure at least 5 cycles of steady LCO. Fig. 3.2a shows the corresponding mean values along with

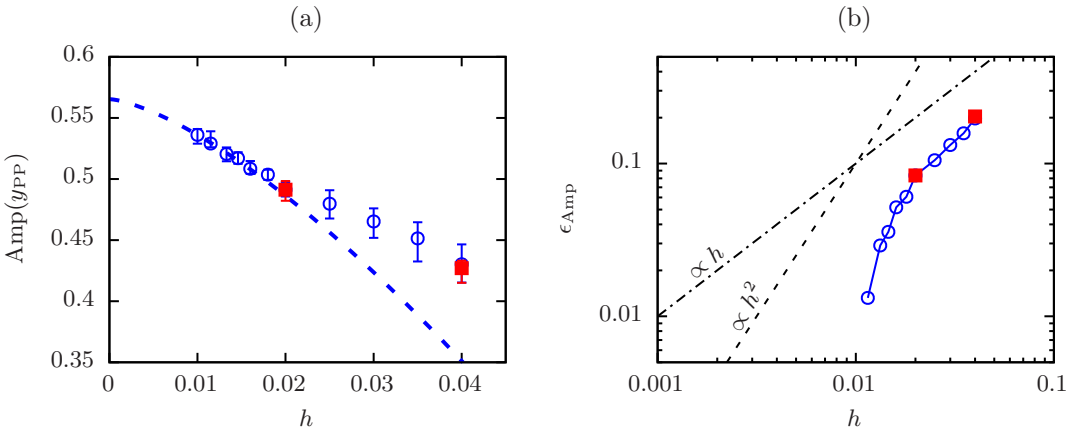

FIGURE 3.2: Grid refinement analysis: (a) amplitude of the pivot point transverse oscillation and (b) corresponding relative error with respect to the solution from the finest grid K (see Table 3.1), as a function of spatial resolution. Blue circles correspond to cases with nonuniform grid spacing (listed in Table 3.1), from which the fitting curve indicated by the blue dashed line is derived, while red squares refer to ones with uniform grid spacing.

the minimum and maximum ones. From the plot one can notice that the convergence trend has a change at about $h = 0.02$, the actual order improving while increasing the resolution. By applying Eq. (3.5), the curve depicted in Fig. 3.2a is found, where the coefficients appearing in the expression are $C \approx -40.7$ and $p \approx 1.44$, yielding the extrapolated value of the exact solution $f^* \approx 0.56$. In the plot we also report data from two cases employing uniform grids with constant spacing $h = \{0.02, 0.04\}$, showing that the discrepancy with equivalent stretched grids (with same h) looks contained and decreases while increasing the resolution. Moreover, we can also refer directly to the relative error with respect to the finest grid considered, as defined by Eq. (3.4). This quantity is shown in Fig. 3.2b where we can notice overall second-order accuracy for finer grids and first-order accuracy for coarser ones, in agreement with what reported by previous studies [85].

In the parametric studies presented in the following, two different grid settings are used. For the single elastically-bounded flapping plate (studied in Sec. 4.2 and Sec 5.1), we use grids E and A, depending on the value of Re. When investigating the dynamics of multiple devices, the chosen settings are grid E for the in-line arrangement (Sec. 6.1). For the staggered (Sec. 6.2) and side-by-side (Sec. 6.3) configurations, we use instead a uniform grid with $h = 0.04$. The latter choice is motivated by the fact that a wider region of the domain has to be refined in this case. One can note that the oscillation gets underestimated when using coarser grids, thus the numerical result is generally conservative from the EH viewpoint. A similar trend can be found for the pitching amplitude, while the flapping frequency shows a convergence that is far more rapid with variations less than 2% within the considered range of spatial resolution.

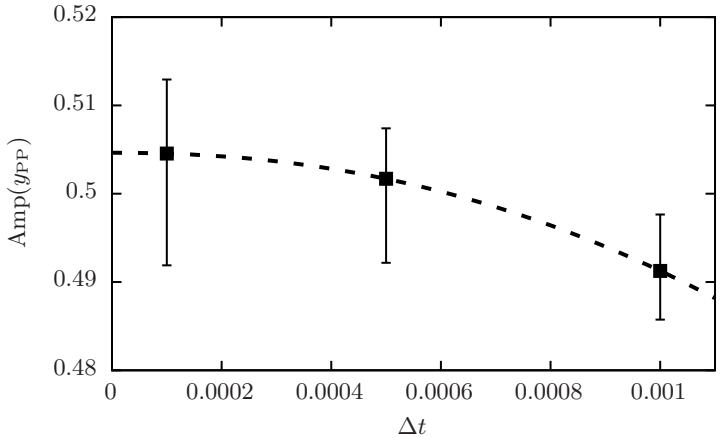

FIGURE 3.3: Amplitude of the PP transverse oscillation, as a function of the numerical timestep, for the case of nonuniform grid E.

Fixing the choice of the grid, we are able to investigate the dependence of the solution with respect to the simulation timestep. Fig. 3.3 shows the convergence when decreasing the timestep, with an estimated error of about 3% with respect to the extrapolated value for vanishing Δt. Last, the sensitivity to the size of the chosen domain was checked, with negligible differences observed in the resulting flapping motion when doubling the size of the bounding box in all directions.

We conclude by providing a comparison of our results with those obtained with an essentially alternative approach, i.e. using a body-conforming mesh. The computation is performed using the open source library `OpenFOAM` [63], which is based on the finite volume method and offers dynamic mesh features, such as the overset treatment that is employed in our benchmark. For this test, we set the case so that the spatial and temporal resolutions are comparable to those of grid A. In Fig. 3.4, we report the time histories of the pivot point motion and pitching angle obtained with the two approaches: all quantities look in good agreement, with small differences in the amplitude and period of the oscillation.

The simulations were performed on the same workstation using 8 processors. The comparison between the computational times of the two codes indicates a wall clock time of $\simeq$ 0.25s per time step for the IBM code and $\simeq$ 5s for OpenFOAM, thus yielding a factor 20. Although the specific figures might depend on the particular computer architecture and the details of the problem, it is clear that the IBM code performs more efficiently for this class of problems. It is worth mentioning that the differences might become even more evident when more than one flapping element is considered in the problem. In fact, while for IB methods the CPU time would grow only because of the larger number of immersed surface elements, for a moving grid method there would be more grid patches in relative motion and the computational

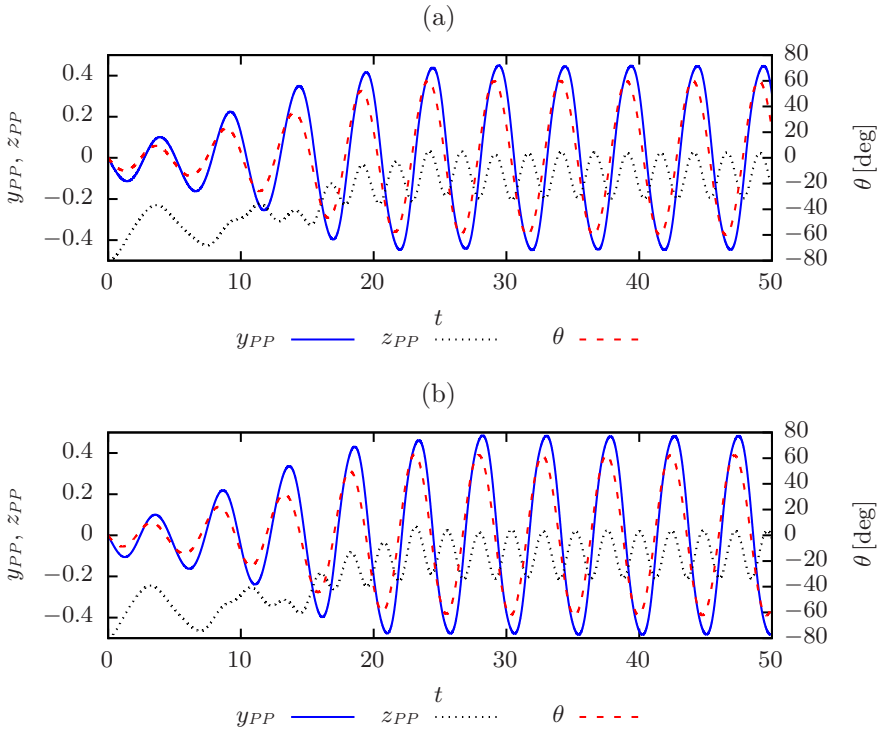

FIGURE 3.4: Comparison of the resulting plate motion between (a) the presently used immersed boundary method and (b) the body-conforming, overset mesh procedure [63], for the case $Re = 100$, $\mathcal{AR} = 2$, $\rho_{\mathrm{w}} = 2$ and $K = 3$, in terms the following observables: PP transverse translation (blue solid line), PP streamwise translation (black dotted line) and pitching angle (red dashed line).

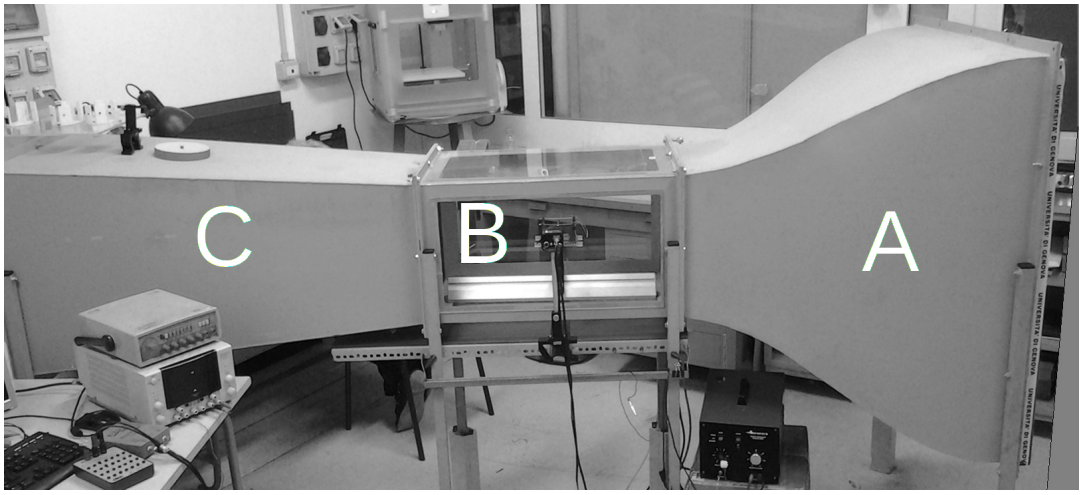

FIGURE 3.5: The employed wind tunnel at DIFI, UniGe, where the real devices are tested, showing: (A) nozzle, (B) test chamber, (C) diffuser.

load would increase more rapidly than the surface element counting.

3.2 Wind-tunnel experiments

Using the computational tool previously described, we aim at providing support for the experimental research activity. This is carried out using a subsonic aspirating open circuit wind tunnel built at the Department of Physics (DIFI) of the University of Genoa (Italy), shown in Fig. 3.5. The air is aspirated through a honeycomb grid into the nozzle (A), conveyed to the test chamber (B) and then through the diffuser (C), at the end of which a three-phase motor of the aspirating fan is collocated. The tunnel has total length 3m and its shape is designed to obtain a stable and controlled laminar flow inside the $40 \times 40 \times 70\,\mathrm{cm}^3$ test chamber, located in the middle part of the tunnel.

The tunnel calibration was performed using a Cobra probe sampling at 1250Hz. A free-stream turbulence level around 0.6% is ensured thanks to the use of the honeycomb grid, the appropriate curvature of the nozzle and the slope of the diffuser. By varying the fan rotational speed, the operational flow velocity in the test chamber ranges from 1.7 to 10.5 m/s with an absolute error of 0.15m/s. Moreover, visualizations of the free-stream flow and of the flow-structure interaction are obtained using a home-made smoke generator apparatus (Fig. 3.6).

By using a 500fps high-definition camera along with an appropriate illumination and video processing system, it is possible to acquire the time history of wing motion: a light scatterer placed on the rotational axis of the wing is illuminated by a line laser

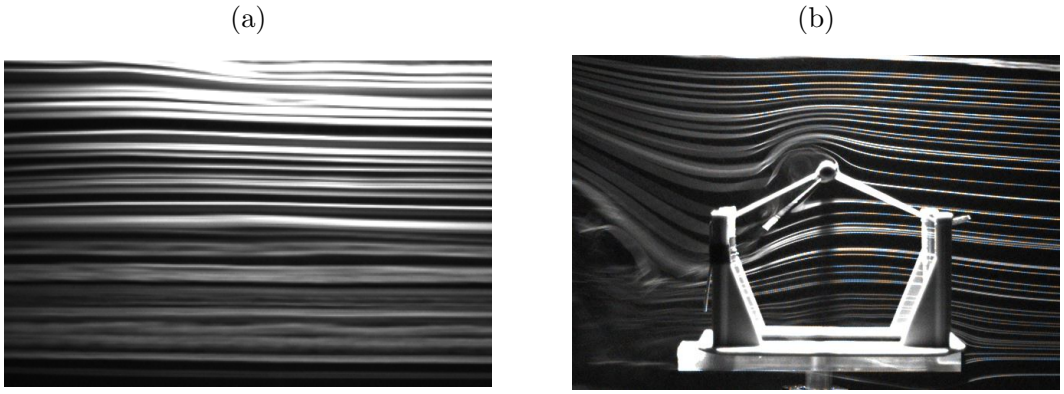

FIGURE 3.6: Flow visualizations using smoke generation: (a) free-stream; (b) flow-structure interaction.

beam and by a numerical elaboration of the movie one can obtain the quantities of interests such as the pivot point and trailing edge positions and the pitching angle.

As for the energy extraction strategy, several configurations are exploitable. We choose to maximize the spatial magnetic flux gradient by fixing the magnets in alternated polarity and locate the coils at the ends of the pivot axis (see Fig. 2.2 and Fig. 2.1a). When LCOs occur, an alternated voltage at the ends of the coils is generated by Faraday effect. An integrated circuit, specifically designed for the EH application, is then used to rectify the signal and store the charges efficiently in a supercapacitor. The electromagnetic coupling depends mainly on the coercive field of the magnets, their internal inductance and number of turns of coils, as well as on the distance and geometry of coils and magnets (further information on this aspect can be found in Refs. [9, 7]).

3.3 Quasi-steady phenomenological model

Besides the numerical and experimental approaches, a reduced-order modeling attempt can be made by means of a set of ordinary differential equations (ODEs) suitable for describing this specific (electro-)aeroelastic system. Seeking for such a mathematical description, we introduce a quasi-steady phenomenological model able to reproduce the nonlinear regimes exploitable for energy harvesting. In this framework, we are inspired by the models originally proposed for the study of falling plates [4, 34, 32] and later applied to describe fluid forces on appendages in animal locomotion [40] as well as flapping foils for EH application [15].

Following this line of reasoning, we seek for a two-dimensional effective description of the system (as that sketched in Fig. 2.1). Our model thus consists of a set of first

order ODEs written in the frame of reference (x', y') co-rotating with the wing[1]:

$$(m + m_{11})\dot{v}_{x'} = (m + m_{22})\dot{\theta}v_{y'} + F^{\mathrm{el}}_{x'} - m'g\sin\theta - \rho_{\mathrm{f}}\Gamma\tilde{v}_{y'} - F^{\nu}_{x'} + F^{\mathrm{EC}}_{x'} \tag{3.6}$$

$$(m + m_{22})\dot{v}_{y'} = -(m + m_{11})\dot{\theta}v_{x'} + F^{\mathrm{el}}_{y'} - m'g\cos\theta + \rho_{\mathrm{f}}\Gamma\tilde{v}_{x'} - F^{\nu}_{y'} + F^{\mathrm{EC}}_{y'} \tag{3.7}$$

$$(I_E + I_{\mathrm{a}})\dot{\omega} = -m_{22}\dot{v}_{y'}r_O - m_w r_w \ddot{y}'_E - C_g\cos\theta + l_\tau\rho_{\mathrm{f}}\Gamma\tilde{v}_{x'} - \tau^{\nu} \tag{3.8}$$

$$\dot{x}'_G = v_{x'} + \dot{\theta}y'_G \tag{3.9}$$

$$\dot{y}'_G = v_{y'} - \dot{\theta}x'_G \tag{3.10}$$

$$\dot{\theta} = \omega \tag{3.11}$$

$$L_{\mathrm{C}}\dot{I} + (R_{\mathrm{C}} + R_{\mathrm{L}})I = V_{\mathrm{emf}} \tag{3.12}$$

In the equations above, $v_{x'}$ and $v_{y'}$ are the center of mass velocity components, $\tilde{v}_{x'} = (v_{x'} - U\cos\theta)$ and $\tilde{v}_{y'} = (v_{y'} + U\sin\theta)$ are those relative to the unperturbed flow, $m_{\mathrm{f}} = \rho_{\mathrm{f}}cs\delta$, $m' = m - m_{\mathrm{f}}$, I_E is the moment of inertia with respect to the pivot point E, $C_g = (m_{\mathrm{w}}r_{\mathrm{w}} - m_{\mathrm{f}}r_O)g$, r_O and r_{w} are the distances between the center of mass and the pivot point (normalized by the chord) considering the translating-only and the translating and rotating bodies, respectively, x'_G and y'_G are the coordinates of the plate center of mass, θ is the pitching angle and $l_\tau = c(2 - \cos\theta)/4$ is the moment arm of the circulatory force. The added mass quantities m_{11}, m_{22} are expressed for the plate of rectangular cross-section following Huang *et al.* [34]: $m_{11} = (3\pi/8)\rho_{\mathrm{f}}\delta^2$, $m_{22} = (3\pi/8)\rho_{\mathrm{f}}c^2$, while $I_{\mathrm{a}} = (5\pi/256)\rho_{\mathrm{f}}(c^2 - \delta^2)^2 + m_{22}r_O^2$ according to Bryant *et al.* [15]. $\mathbf{F}^{\mathrm{el}}$ is the elastic force and $\mathbf{F}^{\mathrm{EC}}$ is the electromechanical coupling force; we model the elastomeric force using Eq. (2.1) and take into account the energy extraction by using the additional equation (3.12), mimicking the presence of a RL circuit which is coupled to the mechanical part, so that we obtain the complete electro-aeroelastic system representative of real EH prototypes (more details will be given in Sec. 5.2.2). The expressions for the aerodynamic quantities, i.e. the circulation Γ, the viscous force $\mathbf{F}^{\nu}$ and the dissipative fluid torque τ^{ν}, are based on those by Andersen *et al.* [4]:

$$\Gamma = -C_T c\frac{\tilde{v}_{x'}\tilde{v}_{y'}}{\sqrt{\tilde{v}^2_{x'} + \tilde{v}^2_{y'}}} + \frac{1}{2}C_R c^2\dot{\theta}, \tag{3.13}$$

[1]For the sake of readibility, we report here only the form used in [8], which differs in some details from the one presented in [62]. Nevertheless, the two versions share all the essential aspects of the model.

$$\mathbf{F}^{\nu} = \frac{1}{2}\rho_{\mathrm{f}} c \left[C_D(0)\,\tilde{v}_{x'}^2 + C_D(\pi/2)\,\tilde{v}_{y'}^2\right] \frac{\sqrt{\tilde{v}_{x'}^2 + \tilde{v}_{y'}^2}}{\tilde{v}_{x'}^2 + \tilde{v}_{y'}^2}\,(\tilde{v}_{x'}, \tilde{v}_{y'}), \tag{3.14}$$

$$\tau^{\nu} = C_{\tau}\rho_{\mathrm{f}}\dot{\theta}\left(\frac{|\tilde{v}_{y'}|c^3}{24} + \frac{|\dot{\theta}|c^4}{64}\right), \tag{3.15}$$

where C_T and C_R are the translational and rotational lift coefficients, $C_D(0)$ and $C_D(\pi/2)$ are drag coefficients in the parallel and normal orientation, and C_τ is the dissipative torque coefficient. These coefficients are actually free parameters of the model that are set after a proper calibration against experimental or numerical data. For example, when considering the prototypal configuration presented in Sec. 2.1 (which will be investigated with this model in Sec. 5.2), by fitting to the experimental data the following set is chosen: $C_T = C_R = 1.0$, $C_D^0 = 0.1$, $C_D^{\pi/2} = 6.5$, $C_\tau = 5.5$.

Some comments are worth concerning this delicate aspect. If one focuses on a range of parameters sufficiently small, we found that a single model calibration is enough to qualitatively reproduce the system dynamics. On the other hand, if one aims at predicting the system behavior for large variations of the physical and geometrical parameters, results provided by the model are generally not accurate and reliable. To overcome this limitation, a good strategy could be, e.g., to follow the idea proposed by Lee et al. [44] where the calibration parameters have been obtained as a function of relevant dimensionless quantities. In this way, the model could be further generalized and thus represent a useful tool for the design of our EH devices, e.g. to find optimal dimensions and/or mechanical properties as a function of those of the fluid flow.

One arising question is whether applying such a quasi-steady modeling is justified in our situation. Although the system reduced frequency, i.e. the Strouhal number $St = fc/U$, is typically found to lie between 0.1 and 0.2, the fact that our phenomenological model works also far from the quasi-steady regime can be traced back to the same reasons invoked in [4] (see their section 3.4). In our case, of course, the wing is not falling in still fluid: it is the wind field that, impacting against it, makes the interaction of the wing with its own wake of little significance. In plain words, leading edge vortices excited during the flapping stage are quickly swept away from the unperturbed flow.

Finally, the effect of structural damping, mainly associated with friction at the hinge axis and possibly to the elastomeric springs, was measured by means of experimental tests perturbating the structure in still fluid, but not included in the presented equations since its contribution is typically negligible when the system undergoes flapping regimes.

Chapter 4

Critical condition for flapping

In the analysis of our aeroelastic system, the first point to be addressed is the condition for which the flutter instability is triggered. In this regard, a common notion in aeroelasticity is the existence of a critical flow velocity U_{cr}, above which the instability starts to manifest [5, 6]. When $U > U_{\mathrm{cr}}$, the wing enters into an *unstable* state undergoing self-sustained oscillations. Conversely, for $U < U_{\mathrm{cr}}$ a *stable* state is found, where the wing eventually aligns with the unperturbed flow.

Historically, the majority of efforts in investigating flutter and other aeroelastic instabilities focused mainly on this aspect, with the goal of avoiding the onset of flow-induced vibrations. However, the same knowledge serves as a starting point also in the EH framework, although with the opposite aim of triggering the instability: U_{cr} can thus be intended as a *cut-in* velocity, i.e. the lower threshold of the operational range for the energy harvester.

The critical velocity depends on several parameters, such as the mechanical properties of the structure (i.e. mass, spring stiffness, geometry), as well as the fluid properties (i.e., density and viscosity). In fact, we can refer more generally refer to a *critical condition* for the onset of aeroelastic instabilities.

Focusing now on elastically-bounded plates, a first insight is given by Fig. 4.1 where the time histories of the plate motion from two numerical simulations are reported. The two cases differ only by the choice of the stiffness K. An initial perturbation is given by imposing non-zero angular momentum at $t = 0$. For $K = 3$ (Fig. 4.1a) we have an unstable configuration with self-sustained oscillation, while increasing the stiffness to $K = 10$ (Fig. 4.1b) above the critical threshold yields a stable state where the perturbation is suppressed.

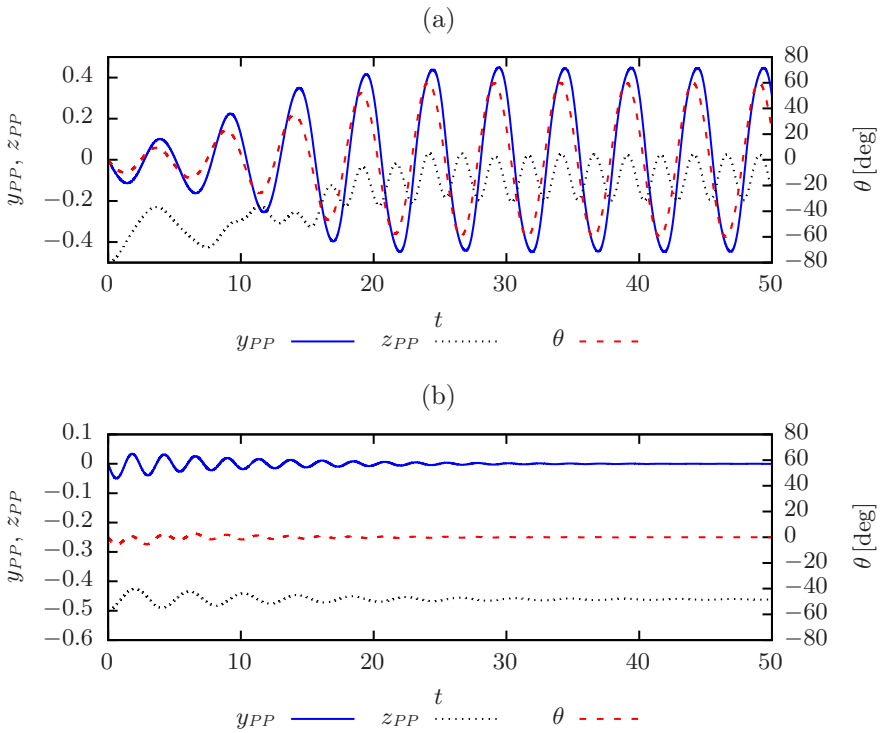

FIGURE 4.1: Time history of motion [PP transverse translation (blue solid line), PP streamwise translation (black dotted line) and pitching angle (red dashed line)] for homogeneous plate at $Re = 100$, $\mathcal{AR} = 2$, $\rho_{\mathrm{w}} = 2$ for (a) $K = 3$ (unstable state) and (b) $K = 10$ (stable state).

The first goal of the present work is thus to identify the critical condition for self-sustained flapping of elastically-bounded plates immersed in uniform flow, in order to reveal the role of the various governing parameters and obtain predictive scaling laws supporting the optimal design of EH devices. Although the topic has already been addressed by previous work, in the two-dimensional case and for very large Reynolds number [64], we propose here a different approach that, despite its simplicity, turns out to have a wider applicability.

In the following of the Chapter, we first identify the critical condition and derive analytical predictions for the onset of flapping (Sec. 4.1); hence, we provide both numerical (Sec. 4.2) and experimental (Sec. 4.3) evidence corroborating such predictions.

4.1 Theoretical prediction

To identify the critical condition for flapping, we propose here a relatively simple approach based on balancing two characteristic timescales (or frequencies) involved in the problem. The first is the natural frequency, while the second is the so-called *wind-vane* frequency. Assuming that both translational and rotational displacements are infinitesimal, an estimation of these timescales is provided. Hence, by balancing the two we obtain a prediction for the critical nondimensional stiffness K_{cr} or, equivalently, the critical velocity U_{cr}.

4.1.1 Natural frequency

The first characteristic timescale that we consider is the one associated with the free response of the elastically-anchored plate when perturbed in the absence of external forcing and damping. Focusing on this uncoupled situation, the evolution of the linear displacement X is thus determined only by the inertial and elastic terms, so that an analogy can be drawn with the equivalent mass-spring system

$$m\ddot{X} + \mathcal{K}X = 0, \tag{4.1}$$

where m is the wing mass and $\mathcal{K}$ is the overall stiffness of the considered system (its explicit expression differs on the basis of the type of elastic elements that are considered, as later shown). To tackle the problem in a complementary way, we will split the analysis by considering two different frameworks.

Let us first refer to the more idealized situation represented by the aeroelastic model introduced in Sec. 2.2, and also sketched in Fig. 4.2a. Here, $\mathcal{K} = 2k$. Assuming a periodic solution $X(t) = X_0 \sin(\omega_{\mathrm{n}} t)$, the well-known expression for the natural

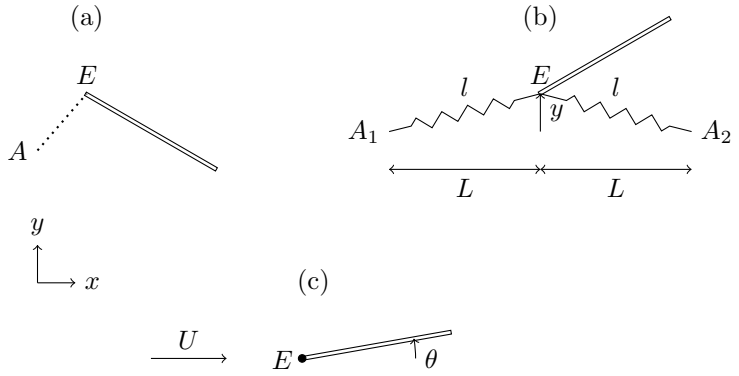

FIGURE 4.2: (a) The ideal model of Sec. 2.2. The dotted line represents the linear spring connecting the anchor point A to the wing pivot point E. (b) The real model representative of our energy harvester. Each elastomer connects the respective anchor point A_i to the wing pivot point E; L is the initial elastomer length while l is the present length during the wing motion; y represents the vertical oscillation of the pivot point. (c) The *wind-vane* situation. The wing is hinged at the pivot point E and rotates about it with a pitching angle θ.

frequency ω_n (in rad/s) holds:

$$\omega_\mathrm{n} = \sqrt{\frac{\mathcal{K}}{m}}. \tag{4.2}$$

To get closer to our real device, we can otherwise consider the situation sketched in Fig. 4.2b. Here, x and y are the horizontal and vertical displacement of the pivot point (assumed to be small), respectively; l is the present length, L the initial length and l_0 is the rest-length of the elastomer; hence, $L = l_0 + \epsilon$ where ϵ is the initially given pre-stretching. Additionally, let G be the shear modulus of the elastomer material and A_0 the initial cross-sectional area of the elastomer. The elastic force modulus is thus assumed to be [75]:

$$F_\mathrm{el} = GA_0 \left[\frac{l}{l_0} - \left(\frac{l_0}{l} \right)^2 \right]. \tag{4.3}$$

The total elastic force along the y-direction can be expressed as:

$$F_y = 4\,GA_0 \left[\frac{\sqrt{L^2 + y^2}}{l_0} - \left(\frac{l_0}{\sqrt{L^2 + y^2}} \right)^2 \right] \frac{y}{\sqrt{L^2 + y^2}} \tag{4.4}$$

that in the limit of small oscillations (i.e. $y \ll l_0 < L$) yields:

$$F_y = 4\,GA_0 \left[\frac{L}{l_0} - \left(\frac{l_0}{L} \right)^2 \right] \frac{y}{L} \tag{4.5}$$

which can be intended as a linear function of y so that it can also be written as $F_y = \mathcal{K}^{\mathrm{eff}}_{(y)}\, y$, where we have introduced the equivalent linear spring stiffness, or effective

stiffness, with respect to the vertical direction:

$$\mathcal{K}^{\text{eff}}_{(y)} = 4\,\frac{GA_0}{L}\left[\frac{L}{l_0} - \left(\frac{l_0}{L}\right)^2\right]. \tag{4.6}$$

Additionally, for the sake of simplicity we can consider the pre-stretching to be small compared to the rest-length i.e. $\epsilon \ll l_0$. In this case, $\mathcal{K}^{\text{eff}}_{(y)}$ reduces to:

$$\mathcal{K}^{\text{eff}}_{(y)} = 12\,GA_0\frac{\epsilon}{{l_0}^2}. \tag{4.7}$$

The natural frequency associated with the vertical oscillations can thus be expressed as:

$$f_{(y)} = \frac{1}{2\pi}\sqrt{\frac{\mathcal{K}^{\text{eff}}_{(y)}}{m}} \tag{4.8}$$

where m is the mass of the device.

Similar considerations can be made for the horizontal displacement. The total elastic force can be expressed now as:

$$F_x = 2\,GA_0\left[\frac{L-x}{l_0} - \left(\frac{l_0}{L-x}\right)^2\right] - 2\,GA_0\left[\frac{L+x}{l_0} - \left(\frac{l_0}{L+x}\right)^2\right] \tag{4.9}$$

that for $x \ll l_0$ yields: $\mathcal{K}^{\text{eff}}_{(x)} = 4\,GA_0/(10\,L^3)(L^3 + 2\,l_0^3)$ and for $\epsilon \ll l_0$ further reduces to $\mathcal{K}^{\text{eff}}_{(x)} = 12\,GA_0/l_0$. Under these assumptions, it is easily seen that

$$\frac{\mathcal{K}^{\text{eff}}_{(y)}}{\mathcal{K}^{\text{eff}}_{(x)}} = \frac{\epsilon}{l_0} \ll 1, \tag{4.10}$$

which means that the natural frequency associated with the streamwise (i.e. surge) oscillations is much higher than the one related to the transverse (i.e. plunge) oscillations. For this reason, we will assume the latter to be the first frequency to couple with the aerodynamic one, which is introduced in the next section.

4.1.2 Wind-vane frequency

The next step is to identify a representative timescale for the action of the flow on the structure. For this purpose, we consider the situation where the wing is hinged at the pivot point and invested by uniform flow (Fig. 4.2c). This choice is justified since the plunge displacement is assumed to be small. In this wind-vane setting, the dynamics is purely rotational and can be described by the moment equation written about the pivot point

$$I_{PP}\,\ddot{\theta} = M^{\text{aero}}_{PP}, \tag{4.11}$$

where I_{PP} denotes the moment of inertia and M_{PP}^{aero} is the aerodynamic moment.

If we also assume the pitching angle θ to be small, the lift force can be evaluated as $C_L = 2\pi\,\theta$ (i.e., it is linear with θ) and considered to be applied at a distance $c/4$ from the leading edge, this yielding the following expression for the aerodynamic moment:

$$M_{PP}^{\text{aero}} = -L\,\frac{c}{4} = -\frac{\pi}{4}\,\rho_{\text{f}}\,c^2\,s\,\theta\,U^2. \tag{4.12}$$

Seeking for a harmonic solution, i.e. $\theta(t) = \theta_0 \sin(\omega_{\text{v}} t)$, the following expression for the wind-vane frequency is found:

$$\omega_{\text{v}} = \frac{\sqrt{\pi}}{2}\,\sqrt{\frac{\rho_{\text{f}}\,c^2\,s}{I_{PP}}}\,U. \tag{4.13}$$

Looking at Eq. (4.13), one can observe that this reflects the existence of an effective rotational stiffness of aerodynamic nature. Despite the absence of any torsional spring, and within the assumption of infinitesimal displacements, a characteristic frequency for pitching can therefore be estimated.

4.1.3 Balance condition for emergence of sustained flapping

At this point, we are able to formulate our prediction by balancing the two characteristic timescales:

$$\omega_{\text{v}} \approx \omega_{\text{n}}. \tag{4.14}$$

From this balance, the expression for the critical flow velocity can be obtained:

$$U_{\text{cr}} \approx \frac{2}{\sqrt{\pi}}\,\sqrt{\frac{\mathcal{K}\,I_{PP}}{m\,\rho_{\text{f}}\,c^2\,s}}. \tag{4.15}$$

This finding can also be rearranged in terms of the nondimensional quantities that were introduced in Sec. 2.2.1, focusing in this case on the critical value of the nondimensional stiffness K_{cr}:

$$K_{\text{cr}} \equiv \frac{\mathcal{K}}{\rho_{\text{f}}\,U^2\,c} = \frac{\pi}{4}\,\frac{m\,c\,s}{I_{PP}}. \tag{4.16}$$

Stable regimes are therefore expected for $U < U_{\text{cr}}$ or, equivalently, $K > K_{\text{cr}}$. Conversely, we predict unstable regimes (i.e. self-sustained flapping states) for $U > U_{\text{cr}}$ or $K < K_{\text{cr}}$.

In the following of the Chapter, this prediction is verified by means of both computational and experimental results, considering different configurations of the aeroelastic system and highlighting the role of geometry and mass distribution on the flapping threshold.

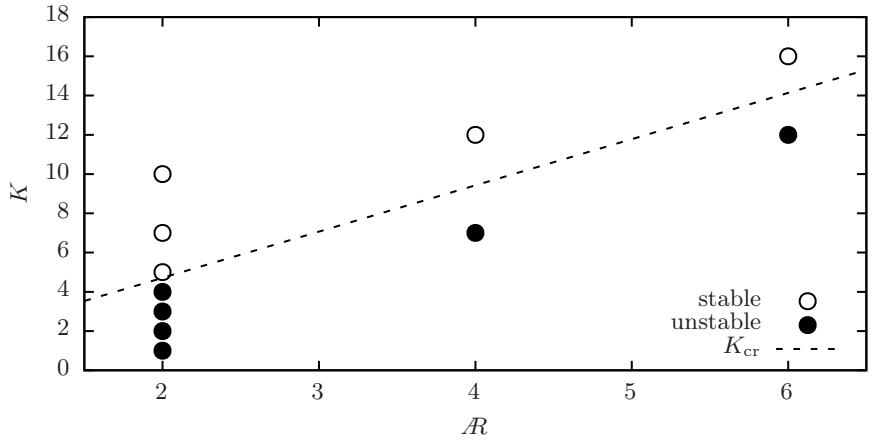

FIGURE 4.3: Threshold for self-sustained flapping in the $(\mathcal{AR}, K)$ plane. Empty circles: stable cases; filled circles: unstable cases. The dashed line reports the theoretical prediction by Eq. (4.17).

4.2 Numerical simulations

In this section, we assess the validity of our theoretical prediction for the nondimensional critical stiffness $K_{\rm cr}$ through a comparison with results from numerical simulations (whose technical description was supplied in Sec. 3.1). We first consider the case of homogeneous plate, and then move to the situation where an additional mass is concentrated on the plate.

4.2.1 Homogeneous plate

As a first step, we apply our theoretical prediction in the framework of the basic model introduced in Sec. 2.2. In this configuration, the moment of inertia with respect to the pivot point is $I_{PP} = m\,c^2/3$. Hence, substituting into Eq. (4.16) yields the following expression for $K_{\rm cr}$:

$$K_{\rm cr} \approx \frac{3}{4}\pi\,\mathcal{AR}, \tag{4.17}$$

which represents the critical condition for the case of homogeneous plate. Looking at Eq. (4.17), we observe that $K_{\rm cr}$ depends linearly on the planform aspect ratio $\mathcal{AR}$. Conversely, both Re and $\rho_{\rm w}$ do not appear, suggesting that they do not influence the threshold for the instability.

To verify this prediction, we have performed a series of simulations at $\rho_{\rm w} = 2$ and $Re = 100$ while varying $\mathcal{AR}$ and K. Results are collected in Fig. 4.3, showing indeed that self-sustained flapping occurs for $K < K_{\rm cr}$ (unstable cases), while the wing asymptotically aligns with the flow for $K > K_{\rm cr}$ (stable cases). As predicted by the theory, a linear dependence of $K_{\rm cr}$ on $\mathcal{AR}$ is found. Although here the simulations

have been performed at $Re = 100$, the same evidence is found for different values (tested up to $Re = 1000$), in agreement with Eq. (4.17) where the Reynolds number does not explicitly appear. Furthermore, similar behaviour has been verified when varying the density parameter ρ_{w}.

4.2.2 Role of additional mass

Having verified the prediction in the simplest case, we now consider the presence of a concentrated mass (i.e., one-dimensional, rod-like and oriented along the spanwise axis) m_{add} placed on the homogeneous plate. This study is also motivated by experimental evidence suggesting a significant role of mass distribution.

In this configuration, the total mass is now $m_{\mathrm{tot}} = m + m_{\mathrm{add}}$, where the additional mass is placed at a distance r_{add} aft of the pivot point. Hence, the moment of inertia is updated to $I_{PP} = m\,c^2/3 + m_{\mathrm{add}} r_{\mathrm{add}}^2$. Plugging these relations into Eq. (4.16) and introducing the mass ratio $\varphi = m_{\mathrm{add}}/m$ and the dimensionless distance $\beta = r_{\mathrm{add}}/c$, the threshold condition gets corrected as

$$K_{\mathrm{cr}} \approx \frac{3}{4}\pi\,\mathit{AR}\,\frac{1+\varphi}{1+3\beta^2\varphi}. \tag{4.18}$$

The role of additional mass appears in Eq. (4.18) as a correction factor with respect to the case of homogeneous plate alone. Looking at this expression, some comments can be made regarding the position of the additional mass β. For $\beta = 1/\sqrt{3}$, the correction ratio becomes unity and the critical condition simplifies into Eq. (4.17), i.e. the same value of K_{cr} holds as for the homogeneous plate. If $\beta < 1/\sqrt{3}$, the critical stiffness increases while increasing φ, enlarging the range of unstable states. The opposite happens when $\beta > 1/\sqrt{3}$.

To verify numerically this expectation, we focus on the case $\mathit{AR} = 2$, $\rho_{\mathrm{w}} = 2$, $Re = 100$, and consider the two limiting positions for the additional mass, i.e. $\beta = 0$ (corresponding to m_{add} placed at the leading edge) and $\beta = 1$ (corresponding to the trailing edge) while varying φ and K accordingly, in order to verify the agreement with Eq. (4.18).

Fig. 4.4 reports the outcome of this investigation. Overall, our theory agrees well with the numerical evidence. For $\beta = 0$ (red circles and dashed line), the correction factor in Eq. (4.18) becomes linear in φ, so that increasing the additional mass always increases the critical threshold. We underline that this corresponds to the most favorable condition for the occurrence of flutter, and consequently for EH. Conversely, adding mass at the trailing edge, i.e. when $\beta = 1$ (blue squares and dotted line), has a stabilizing effect, hence decreasing K_{cr}, although with a tendency to saturate for

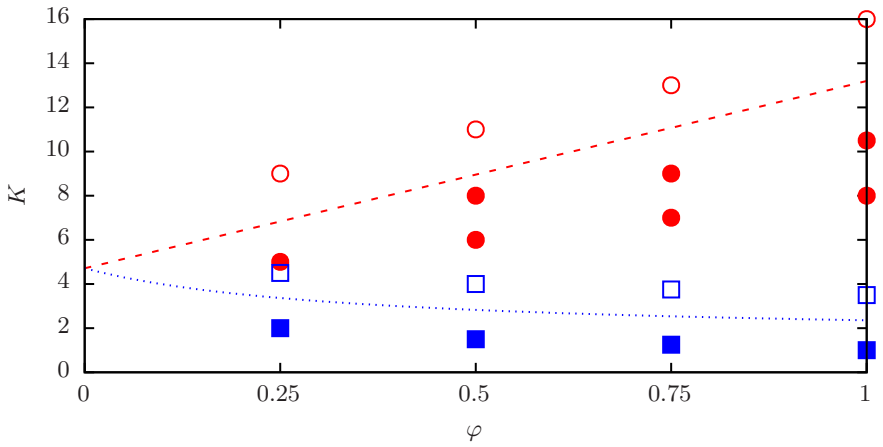

FIGURE 4.4: Threshold for sustained flapping in the (φ, K) plane. The theoretical prediction from Eq. (4.18) is compared with numerical simulations for two different positions of the additional mass (red dashed line vs circles: $\beta = 0$; blue dotted line vs squares: $\beta = 1$). Empty circles/squares denote stable cases and filled circles/squares unstable ones.

large φ: for $\varphi \to \infty$, Eq. (4.18) tell us indeed that $K_{\mathrm{cr}} \to (\pi \mathcal{AR})/4$. Finally, note that for $\varphi = 0$, we recover the case of homogeneous plate alone predicted by Eq. (4.17).

4.3 Wind-tunnel experiments

We now move to corroborate our theory against experimental data, considering real devices such as those already introduced in Sec. 2.1. In particular, we will compare the theoretical value of the critical velocity given by Eq. (4.15) with the measurements performed in wind-tunnel experiments (whose technical description was supplied in Sec. 3.2).

Before presenting such comparison, some observations are worth to be considered. Experimentally, a hysteresis phenomenon has been observed in what it concerns the resulting wing motions whether increasing or decreasing the wind speed, as also observed for similar aeroelastic systems [74, 3, 68]. This turns out to be crucial also when identifying the flapping threshold, leading to the problem on how to define a conventional critical flow velocity U_{cr}. In fact, depending on the previous history the latter may vary within a specific range. In our case, we will assume U_{cr} to be the lower limit of the range that is measured when the wing is already flapping and the wind speed is decreased. However, this is typically found to be between 0.8 and 0.9 times the upper limit (conversely, this is measured when starting from stable state and increasing the wind speed), in agreement with observations reported for classical-flutter systems [3].

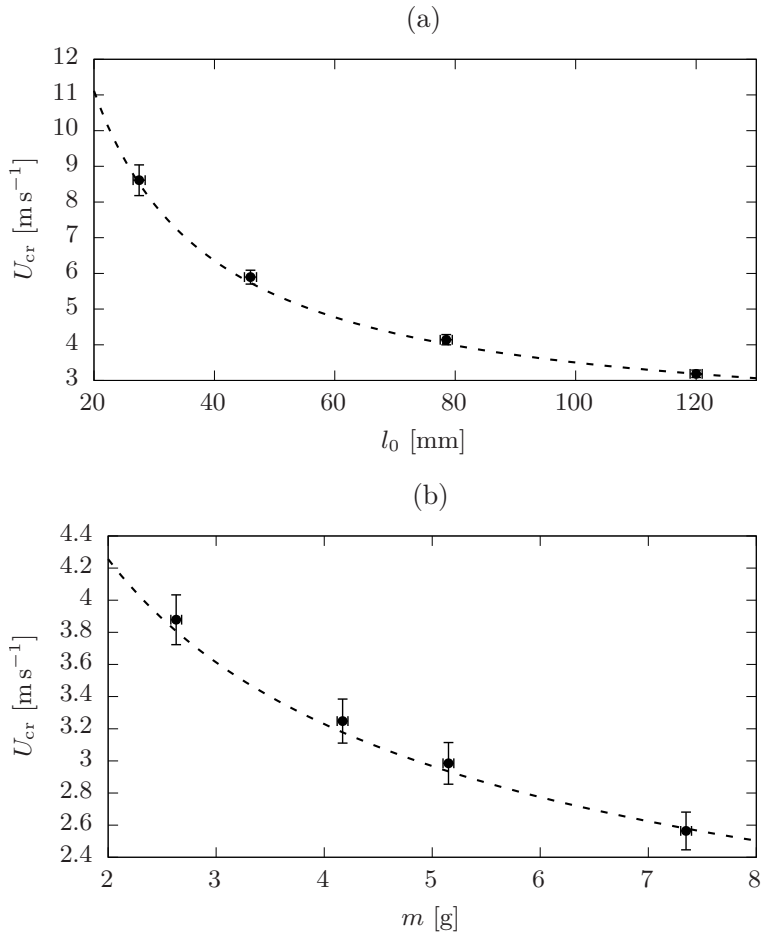

FIGURE 4.5: Experimental measurements of the critical velocity for the onset of sustained flapping (a) as a function of the elastomer rest-length l_0 (here, $m = 1.63$g) and (b) as a function of the wing mass m (with $l_0 = 58$mm, $L = 66$mm). The dashed line represents the marginal curve based on Eq. (4.15).

In order to verify the condition for the emergence of self-sustained flapping according to Eq. (4.15), two studies have been performed. For all measurements, the type of elastomers is fixed such that $GA_0 = 0.604$N while the wing geometry is set to be: $c = 60$mm, $s = 70$mm.

In the first study, we investigate the dependence of the critical velocity $U_{\rm cr}$ on the elastomer rest-length l_0 (while a constant pre-stretching ϵ is retained), i.e. varying the effective stiffness $\mathcal{K}^{\rm eff}_{(y)}$. The experimental results are shown in Fig. 4.5a along with the prediction expressed by Eq. (4.15) where we make use of the simplified expression for $\mathcal{K}^{\rm eff}_{(y)}$, Eq. (4.7), so that the expected scaling turns out to be $U_{\rm cr} \sim l_0^{-1}$. The measurements are found to be in good agreement with the theoretical prediction. For the lowest tested value $l_0 = 25$mm the critical velocity is around $8.5\,\mathrm{m\,s^{-1}}$, while for the highest one ($l_0 = 120$mm) it drops to approximately $3\,\mathrm{m\,s^{-1}}$. This clearly shows how the cut-in speed of the system can be governed by acting on this simple control

parameter.

Next, we focus on the dependence of U_{cr} upon the mass of the system m. In this experiment, the mass is varied by placing additional weights on the wing rotation axis so that the moment of inertia I_{PP} is kept constant. Hence, from Eq. (4.15) it follows that a scaling according to $U_{\mathrm{cr}} \sim (\sqrt{m})^{-1}$ has to be expected. Fig. 4.5b collects the experimental evidence and the theoretical prediction, showing a satisfactory agreement. To give a quantitative indication, let us point out that, for the given configuration, U_{cr} may be reduced of around 33% by placing a 4.5g additional mass on the pivot axis.

Similarly to what we have found before in the simplified framework, the wind-tunnel study appears to verify the balance condition that has been proposed for predicting the onset of self-sustained flapping.

Chapter 5

Postcritical flapping states

Once successfully identified the critical condition for flapping, the next step is to explore the postcritical regime, i.e. the region where $K < K_{\mathrm{cr}}$ or, equivalently, $U > U_{\mathrm{cr}}$. Entering this regime, the role of the nonlinear aspects underlying the aeroelastic instability becomes essential, resulting in limit-cycle oscillations (LCOs) or chaotic motions. In this work, we will focus on regular LCOs which are of greater interest for EH application. The Chapter first deals with results from numerical simulations (Sec. 5.1) and then presents a comparison between experimental measurements and the phenomenological quasi-steady model (Sec. 5.2). Overall, we show how the aeroelastic model is capable of reproducing qualitatively the essential features observed experimentally.

5.1 Numerical investigation

Let us begin our analysis by considering the aeroelastic model of Sec. 2.2, similarly to what we did in the previous Chapter when investigating the flapping threshold. By means of numerical simulations, a parametric analysis has been carried out over three of the governing parameters, i.e. Re, ρ_{w} and K, while retaining the same aspect ratio $\mathit{AR} = 2$. The effect of each parameter is described by looking at several quantities of interest with impact on the potential for energy harvesting.

The first two are kinematic quantities, i.e. the peak-to-peak amplitude of the pivot point (PP) displacement along the transverse distance, $\mathrm{Amp}(y_{PP})$ (normalized by the wing chord), and the Strouhal number, $St = fc/U$ (i.e., the nondimensional frequency).

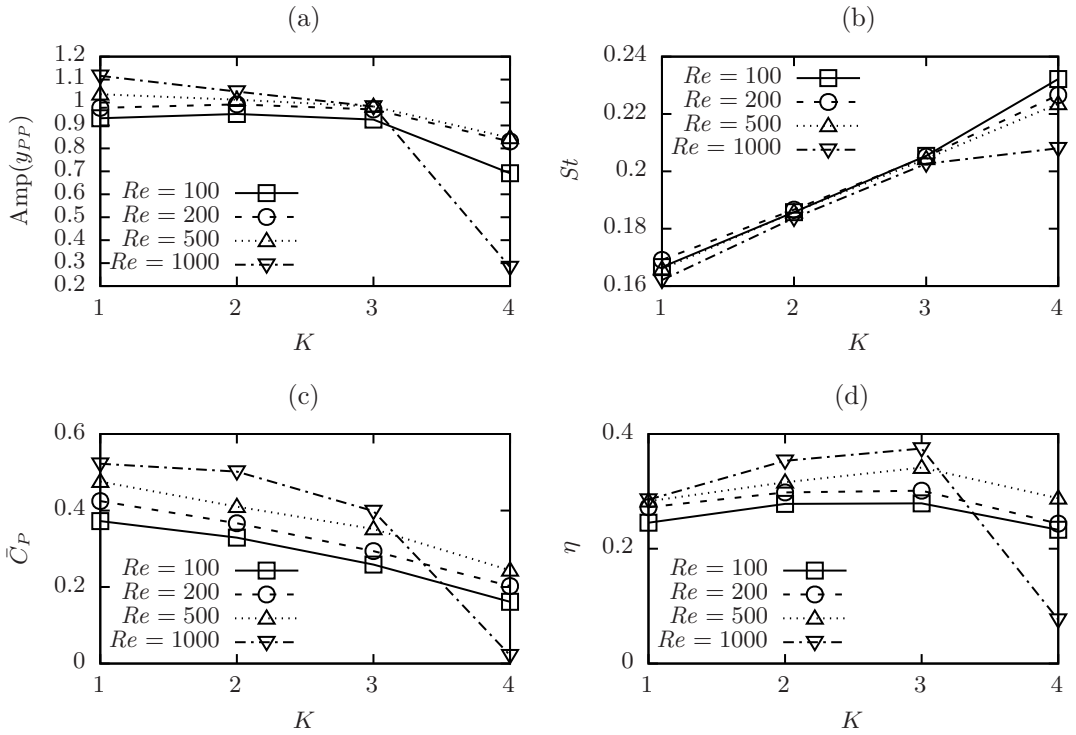

FIGURE 5.1: Flapping observables for the single device as a function of K for $Re = \{100$ (squares, solid line), 200 (circles, dashed line), 500 (triangles, dotted line), 1000 (reverse triangles, dash-dotted line)$\}$, $\rho_{\mathrm{w}} = 2$ and $\mathcal{AR} = 2$: (a) PP transverse oscillation amplitude, (b) Strouhal number, (c) power coefficient and (d) Betz efficiency.

The other two quantities are the average plunge power coefficient $\bar{C}_P$ and the Betz efficiency η, defined as:

$$\bar{C}_P = \frac{\bar{P}_y}{\frac{1}{2}\,\rho_{\mathrm{f}} s c U^3}, \tag{5.1}$$

$$\eta = \frac{\bar{P}_y}{\frac{1}{2}\,\rho_{\mathrm{f}} s d U^3}, \tag{5.2}$$

where $\bar{P}_y = \frac{1}{T}\int_T F^y_{\mathrm{aero}}\,\dot{y}_{PP}\,\mathrm{d}t$ is the average power associated with the plunge motion, F^y_{aero} is the vertical component of the aerodynamic force (i.e., the lift force), and d is the maximum transverse distance swept by the wing during its motion. $\bar{C}_P$ and η are dynamic quantities giving an indication of the energy extracted by the structure from the fluid flow and thus of the potential EH performance.

5.1.1 Effect of K and Re

We start by performing a parametric study over different values of the nondimensional stiffness $K = \{1, 2, 3, 4\}$ and Reynolds number $Re = \{100, 200, 500, 1000\}$. Note that

here $K < K_{\mathrm{cr}}$, where K_{cr} is the value corresponding to the critical condition for the onset of flapping as derived in Chapter 4. Here, we fix $\rho_{\mathrm{w}} = 2$ and $\mathit{AR} = 2$.

The resulting four quantities of interest introduced previously are reported in Fig. 5.1. The first is the pivot point amplitude $\mathrm{Amp}(y_{PP})$. As shown in Fig. 5.1a, $\mathrm{Amp}(y_{PP})$ is found to increase for decreasing K, i.e. softening the spring. On the other hand, the Strouhal number St increases almost linearly with K (Fig. 5.1b). Moreover, the flapping frequency is always found to be larger than the natural frequency (not shown here), as it is generally the case for flutter-based systems.

Looking at Fig. 5.1c, the trend of the power coefficient $\bar{C}_P$ appears qualitatively similar to those found for the PP amplitude. For lowering K, we can argue that the variation of $\bar{C}_P$ gets smaller (although this conclusion should perhaps be corroborated by an investigation over a wider range of K). Conversely, for the Betz efficiency η (Fig. 5.1d) the trend is not monotonic and thus an optimal condition exists at which η gets maximized.

Overall, variations of the Reynolds number do not appear to modify substantially the described trend. For lower Re, however, the oscillation amplitude weakens, as well as power and efficiency, consistently with a more dominant effect of viscosity, except for the stiffest case $K = 4$ where for $Re = 1000$ we observe a sharp decrease. In this case, it can be observed that the wake remains attached to the wing, while for lower Re a sequence of vortices is released from the leading edge, producing higher oscillations. Nevertheless, the Reynolds number appears to play a minor effect. In light of this evidence, in the rest of this study we will focus only on $Re = 100$.

5.1.2 Effect of ρ_{w}

To move further, we have performed another study where the nondimensional stiffness is fixed to $K = 3$ (yielding the maximum η, at $Re = 100$) and the density ratio ρ_{w} is varied between 1 and 10. Results are shown in Fig. 5.2 reporting the same quantities as for the previous analysis.

Starting with the amplitude (Fig. 5.2a), we observe that $\mathrm{Amp}(y_{PP})$ always increases with ρ_{w} and, in particular, there is a sharp variation at the smallest ρ_{w} (between 1 and 1.5). This provides an indication of the essential role of inertia in the fluid-structure interaction. Looking at the flapping frequency (Fig. 5.2b), it is apparent that $St \propto 1/\sqrt{\rho_{\mathrm{w}}}$. This proves that, although being different, the flapping frequency is proportial to the natural frequency and thus depends on the plate inertia. As it was already found for the dependence on K, $\mathrm{Amp}(y_{PP})$ and St show opposite trends while varying ρ_{w}. In this case, however, the variations of both quantities over the investigated parametric range are more pronounced. As a result, the power coefficient has now a different shape (Fig. 5.2c). It shows a maximum for $\rho_{\mathrm{w}} = 1.5$,

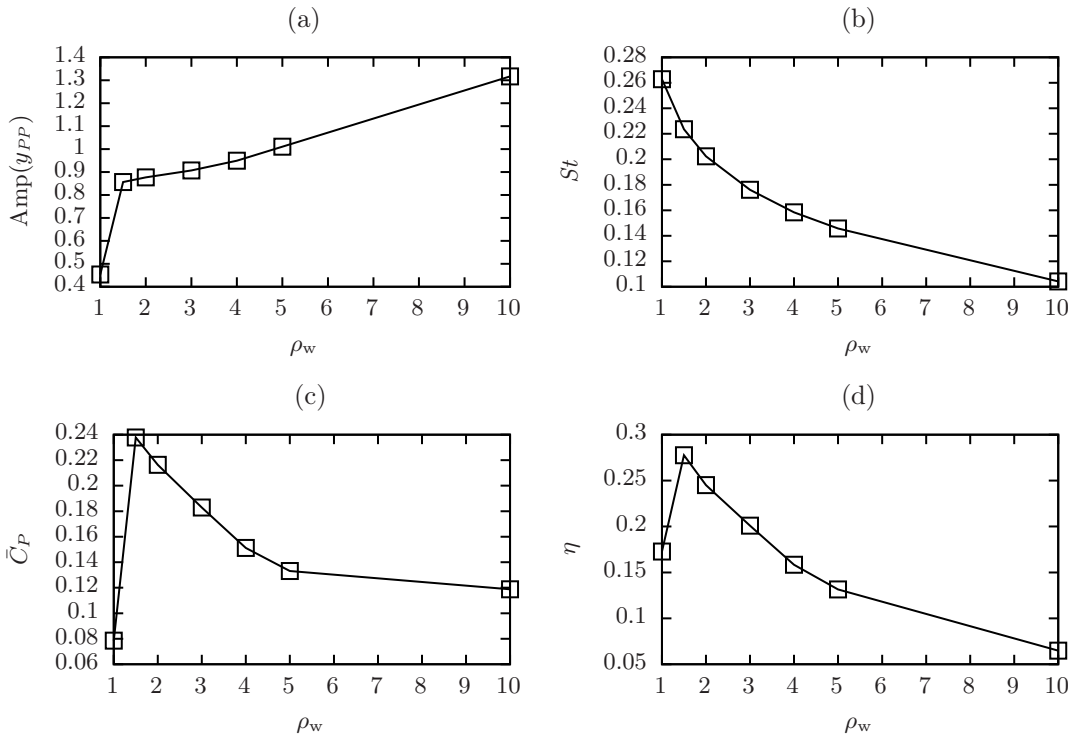

FIGURE 5.2: Flapping observables as a function of ρ_w for $Re = 100$, $K = 3$ and $\mathit{AR} = 2$: (a) PP transverse oscillation amplitude, (b) Strouhal number, (c) power coefficient and (d) Betz efficiency.

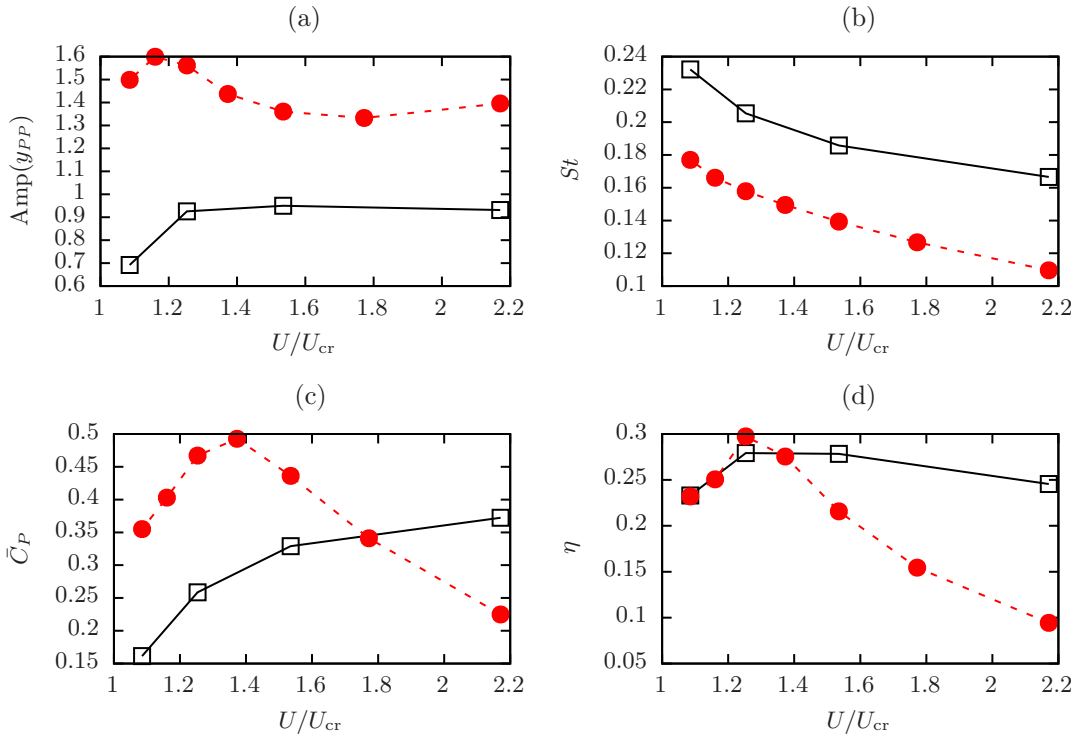

FIGURE 5.3: Flapping observables as a function of U/U_{cr} for $Re = 100$, $\rho_w = 2$ and $\mathcal{AR} = 2$ for plate with (red filled circles and dashed line) and without additional mass (black empty squares and solid line): (a) PP transverse oscillation amplitude, (b) Strouhal number, (c) power coefficient and (d) Betz efficiency.

given by the corresponding high value of St and finite Amp(y_{PP}). However, for a slight decrease of the density ratio, $\bar{C}_P$ drops to its minimum value due to the sharp decrease of Amp(y_{PP}). For $\rho_w > 1.5$, $\bar{C}_P$ gradually decreases since the frequency is decreasing more rapidly than the increase of amplitude. Finally, the Betz efficiency (Fig. 5.2d) shows here a shape that is rather similar to that of the power coefficient.

5.1.3 Effect of additional mass

We now consider the presence of an additional mass on the plate as done in Sec. 4.2.2 for identifying the flapping onset. As shown later in Sec. 5.2, with this feature it is possible to obtain a dynamical behaviour which is rather similar to that observed experimentally, including the appearance of optimal conditions for maximizing the oscillation and the extraction. Recalling the definitions introduced in Sec. 4.2.2, we choose $\beta = 0$ and $\varphi = 1$, which was found to be the configuration most prone to the instability among those considered, and perform computations while varying the stiffness over the set $K = \{2, 3, 4, 5, 6, 7, 8\}$.

Let us start by comparing this configuration with the one without additional mass, referring to the usual four observables Amp(y_{PP}), St, $\bar{C}_P$ and η. For a more direct

comparison, these are reported in Fig. 5.3 as a function of the ratio U/U_{cr} instead of K. This is done since the range of unstable states for the two configurations is different (i.e., the one with additional mass has a higher K_{cr}). Moreover, this will also provide an easier comparison with experimental measurements.

From Fig. 5.3, we observe that a pronounced peak at an intermediate K now occurs for the amplitude (Fig. 5.3a), the power coefficient (Fig. 5.3c) and the Betz efficiency (Fig. 5.3d). Furthermore, the amplitude increases appreciably compared to the case without additional mass, while the Strouhal number (Fig. 5.3b) has the same qualitative behaviour but smaller values, consistent with the fact that K decreases while increasing U/U_{cr}. The peak of the power coefficient occurs for $U/U_{\mathrm{cr}} \approx 1.4$ which corresponds to $K = 5$, reaching the value $\bar{C}_P \approx 0.5$. Compared to the homogeneous plate alone (where the maximum occurs for the smallest $K = 1$), we obtain a significant increase around 40%. On the other hand, the maxima in the efficiency are comparable, i.e. $\eta \approx 30\%$, and occurs at a similar value of U/U_{cr}.

To understand in more detail the optimal condition maximizing $\bar{C}_P$, Fig. 5.4 reports for three different cases the time history of the instantaneous power coefficient, along with the lift coefficient C_L and the pivot point transverse velocity $\dot{y}_{PP}$, their product giving C_P. Fig. 5.4a shows the case $K = 2$ which corresponds to the highest value of $U/U_{\mathrm{cr}} \approx 2.2$ that was tested, for which the lowest value of $\bar{C}_P$ is found. Indeed, both the lift (dotted line) and the PP velocity (dot-dashed line) have relatively small amplitude, along with a phase delay of the latter with respect to the former. As a result, the power coefficient (thick solid line) shows a limited amplitude. The second case, shown in Fig. 5.4b, is the optimal condition with $K = 5$ (corresponding to $U/U_{\mathrm{cr}} \approx 1.4$), where both the amplitude of C_L and $\dot{y}_{PP}$ increase while they become essentially in-phase, so that the resulting power coefficient is almost positive-only and with pronounced peaks, yielding the maximum mean value discussed before. In the third case, $K = 8$ (or equivalently $U/U_{\mathrm{cr}} \approx 1.1$), some phase shift is present again and in turns the oscillation gets decreased. The power coefficient has a larger negative region that decreases substantially the mean value.

Overall, Fig. 5.4 supplies only a description of the different flapping states while varying K. Given the fully passive nature of the aeroelastic system, the phase shift between C_L and $\dot{y}_{PP}$ and their respective amplitude of oscillation are strictly connected. However, some further observations can be drawn. One can notice, in particular, how the form of the lift coefficient differs between the three cases, with a stronger presence of a secondary peak for increasing K (i.e., decreasing U/U_{cr}). It can be argued that this is related to a different way of interacting between the plate and the vortices that are created during the flapping motion.

From the numerical simulation we can also obtain a three-dimensional visualization of the vortical structures that are created by the interaction between the flapping wing

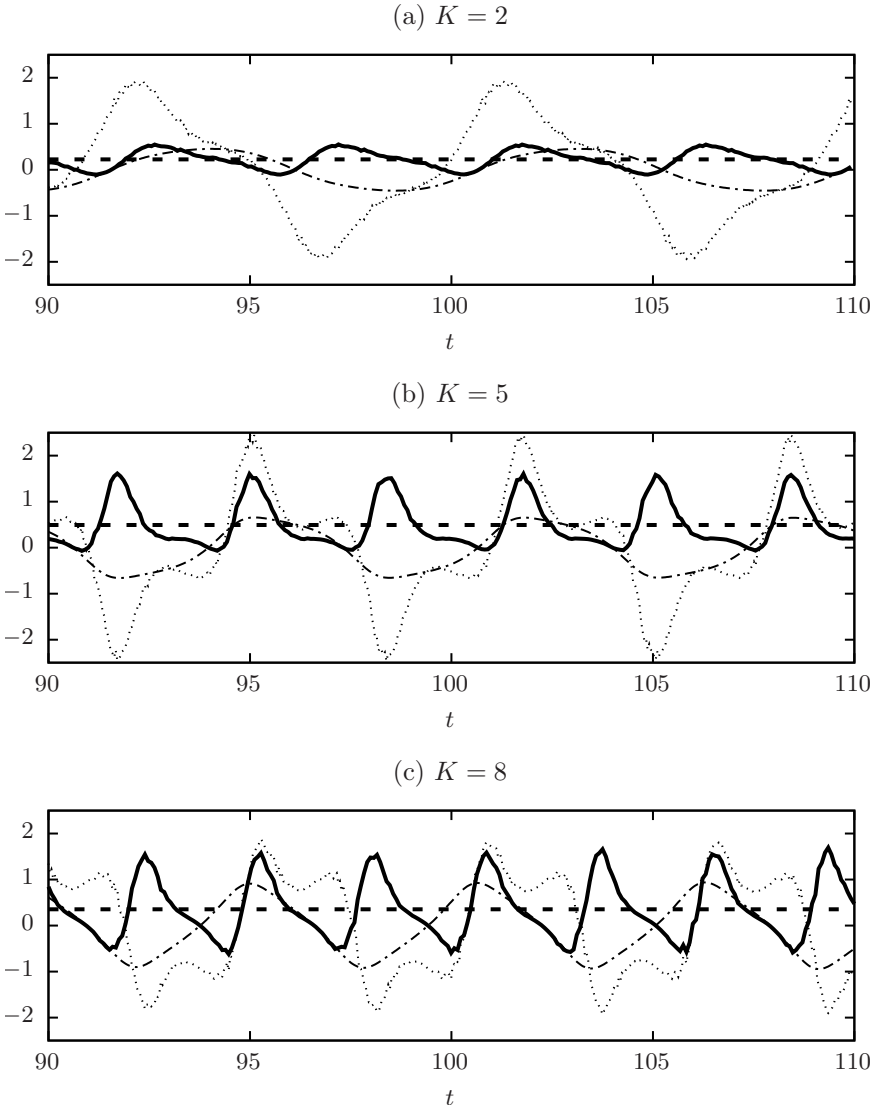

FIGURE 5.4: Time histories of instantaneous power coefficient (thick solid), lift coefficient (dotted) and pivot point transverse velocity (dot-dashed) and average power coefficient (thick dashed line), for (a) $K = 2$, (b) $K = 5$ and (c) $K = 8$.

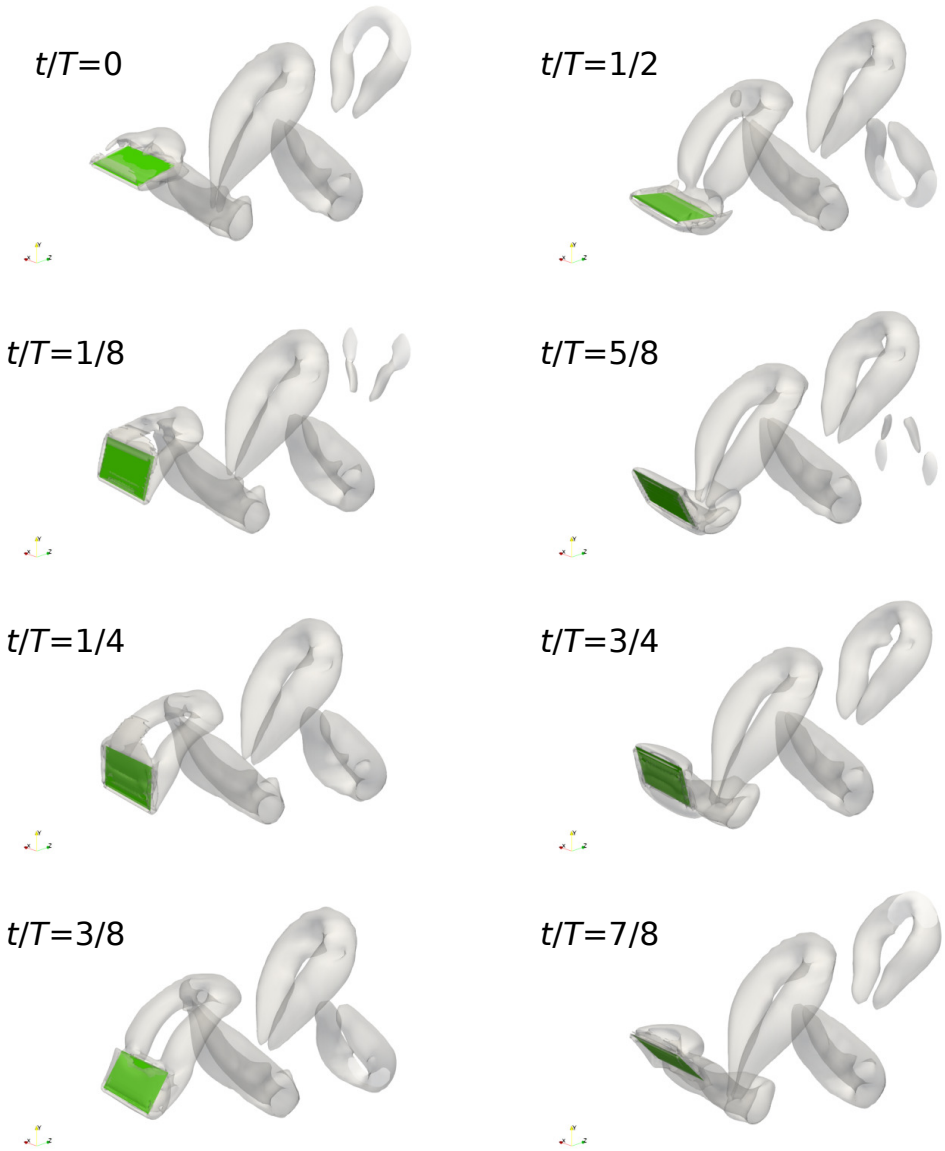

FIGURE 5.5: Q-visualization over one flapping cycle for the case: $\mathcal{AR} = 2$, $\rho_w = 2$, $Re = 100$, $K = 5$ and additional mass with $\beta = 0$, $\varphi = 1$.

and the incoming flow. To this aim, we compute the second invariant of the velocity gradient tensor Q and identify vortices using the Q-*criterion*

$$Q = \frac{1}{2}[|\mathbf{\Omega}|^2 - |\mathbf{S}|^2] > 0, \tag{5.3}$$

where $\mathbf{\Omega}$ and $\mathbf{S}$ are the anti-symmetric and symmetric part of $\nabla\mathbf{u}$, respectively [29].

The visualization of Q-isosurfaces over one flapping period is supplied by Fig. 5.5. Here we show the optimal configuration with $K = 5$ but the outcome is similar for different K (suggesting that the aforementioned interaction details affecting the power extraction arise in the close proximity of the wing). The wake topology has an intrinsic three-dimensional structure, as expected given the plate aspect ratio $\mathcal{AR} = 2$. Spanwise-oriented vortices periodically detach from the leading edge, between $t/T = 1/8$ and $t/T = 1/4$ (during the downstroke) and between $t/T = 5/8$ and $t/T = 3/4$ (during the upstroke). Once detached, they are convected downstream and rapidly merge with chordwise-oriented vortices generated at the side ends, leading to a characteristic horseshoe structure in the wake.

FIGURE 5.6: Sideviews showing pivot point and trailing edge trajectories for different U/U_{cr} (increasing from left to right) from the numerical simulations using additional mass with $\beta = 0$ and $\varphi = 1$ (first row, red), wind-tunnel experiments (second row, blue) and phenomenological model (third row, green).

5.2 Quasi-steady modeling of experimental configurations

In this section, we present results from wind-tunnel measurements, against which we apply the phenomenological model introduced in Sec. 3.3 to reproduce the same evidence.

5.2.1 Configuration without energy extraction

We start by considering the case in the absence of any energy extraction mechanism. In this configuration, the wing is made by a rectangular plate with chord $c = 20$mm, span $s = 70$mm and thickness $\delta = 100\mu$m. The pivot axis is located at 0.5mm from the leading edge. The total mass of the moving system is $m = 0.845$g. Concerning the anchoring elements, each elastomer has diameter is $D_0 = 1.2$mm and length $l_0 = 47.3$mm, at rest. A pre-stretching is given so that the initial length is $L = 66.3$mm. The elastic force magnitude for each elastomer is thus given by $|F_{\rm el}| = GA_0(L/l_0 - (l_0/L)^2)$ [75], where the material shear modulus value is $G = 0.534$MPa and $A_0 = \pi D_0^2/4$. The natural frequency of the system relative to the vertical motion can be measured from the free oscillation of the pivot point when perturbating the elastically bounded wing along the vertical direction, in still fluid, having $f_{(y)} = 13.2$Hz. From this quantity combined with the given mass, using Eq. (4.8) we can compute the equivalent linear stiffness $\mathcal{K}_{(y)}^{\rm eff}$ (cf. Sec. 4.1.1).

Let us propose first a comparison with the numerical evidence presented in the previous section. Fig. 5.6 shows the trajectories from a side view of the pivot point and trailing edge from the numerical simulations of Sec. 5.1.3 along with those obtained from the experimental testing of the present configuration. Moreover, we also report the results from the quasi-steady phenomenological model introduced in Sec. 3.3.

As anticipated, the numerical solution turns out to capture the essential phenomenology that is observed in the experiments, despite the simplifications adopted by the idealized model. For the experimental and quasi-steady modeling results, the motion of the PP is almost purely transverse, unlike that of the numerical ones; however, this difference is simply due to the different arrangements of the elastic elements (in the idealized model, only a pair of springs is present without any pre-stretching suppressing the horizontal motion). On the other hand, the agreement looks better for the trailing edge trajectory showing a lemniscate-like shape.

This resemblance is confirmed by looking at Fig. 5.7 where we report the PP transverse amplitude and Strouhal number, as a function of $U/U_{\rm cr}$, obtained from the laboratory measurements and given by the quasi-steady model. Overall, the trends of these two quantities are in qualitative agreement with those reported in Fig. 5.3 for the numerical investigation.

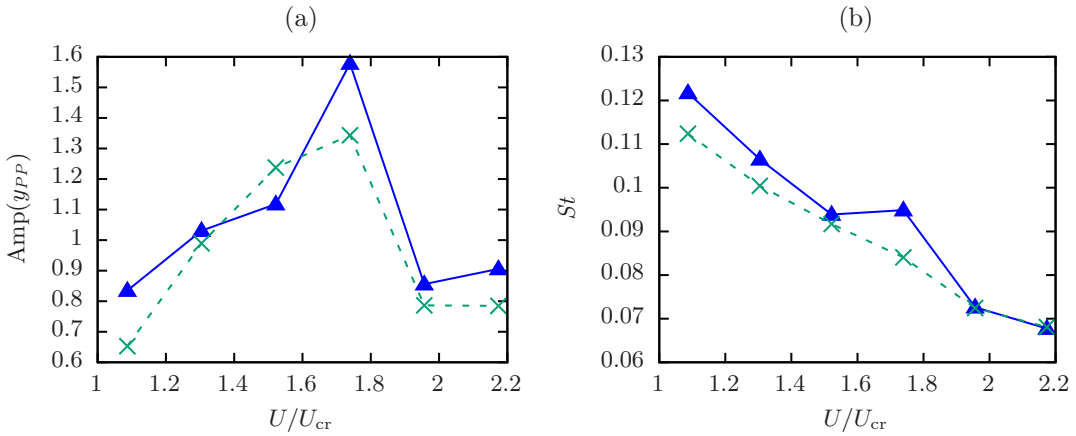

FIGURE 5.7: (a) PP transverse oscillation amplitude and (b) Strouhal number as a function of U/U_{cr} for the experimental configuration described in Sec. 5.2: comparison between wind-tunnel measurements (blue triangles and solid line) and phenomenological model of Sec. 3.3 (green crosses and dashed line).

Looking at Fig. 5.7a, the amplitude of flapping increases for increasing U up to $U/U_{cr} \approx 1.8$ where it suddenly reaches a peak. Increasing further the velocity, the resulting shapes of the trajectory change, showing a wider amplitude of the trailing edge oscillation and the opposite trend for the PP. Displacements are typically of the same order of the wing chord and a maximum exists for the PP amplitude. Concerning the results given by the phenomenological model, the peaks are smoothed with respect to the experimental evidence. One possible cause of such discrepancy is that the model might not properly reproduce some unsteady, time-history dependent features [4]. Apart from this specific aspect, the proposed reduced-order model looks capable of reproducing within reasonable accuracy the aeroelastic behavior of the system that is observed experimentally.

5.2.2 Configuration with energy extraction

We now turn our attention to the experimental prototype that was introduced and described in Sec. 2.1. Reviewing the main parameters, the wing has chord $c = 35$mm, span $s = 85$mm and foil thickness $\delta = 100\mu$m. The pivot axis is set at $0.1c$ from the leading edge. The total mass of the system (wing, axis, supports and elastomers) is $m \approx 5.0$g; The elastomers have at rest diameter $D_0 = 1.2$mm and length $l_0 = 50.3$mm and they are pre-stretched to the initial length $L = 73$mm.

Concerning the electromagnetic apparatus, a pair of coils is placed at the ends of the pivot axis, each with $N_C = 1650$ turns, internal resistance $R_C = 150\Omega$, internal inductance $L_C = 10$mH, internal and external diameter $\phi_i = 5$mm and $\phi_e = 9$mm, respectively, and height $h_C = 5$mm. Two vertical bars of nine $Nd_2Fe_{14}B$ magnets of size 10mm $\times$ 10mm $\times$ 4mm with maximum coercive field $H_{max} = 38$MOe are placed

in front of the coils, at a distance $d_{\mathrm{M-C}} = 1\mathrm{mm}$. The coils are connected in series to an external circuit with a variable resistive load R_{L} (see Fig. 2.1b).

To perform the measurements we proceed as follows: first the fan is turned on at a given voltage which corresponds to a certain flow velocity and the wing is let to reach the steady flapping regime without energy extraction, by setting $R_{\mathrm{L}} = 4\mathrm{M}\Omega$ (i.e. equivalent to the open-circuit condition); subsequently, we reduce the resistive load to the specified value and the resulting voltage V_{L} at the load is measured by a PicoScope 4224 oscilloscope. From the root mean square of the latter we can measure the mean power dissipated by the applied load $P_{\mathrm{out}} = V_{\mathrm{rms}}^2/R_{\mathrm{L}}$ and in this way we can map the extracted power as already shown in Fig. 2.4.

When applying the quasi-steady model, a particular aspect concerns how to express the induced electromotive force $V_{\mathrm{emf}} \equiv -\Phi_{,y}\,\dot{y}_{\mathrm{E}}$, where Φ is the magnetic flux accross the coils and $\dot{y}_{\mathrm{E}}$ is the vertical velocity of the pivot point [20]. Aided by two-dimensional numerical simulations of the electromagnetic field performed with the `FEMM` software [50] along with experimental observations, we assume $\Phi_{,y} = K\sin\left(\pi y_{\mathrm{E}}/h_{\mathrm{mag}}\right)$, where h_{mag} is the magnet height. Note that this approximation holds when the coil diameter and the magnet height are almost equal, as in the present case, otherwise the gradient shape may differ and should be modelled properly. The electromotive force can thus be written as

$$V_{\mathrm{emf}} = -K\sin\left(\frac{\pi y_{\mathrm{E}}}{h_{\mathrm{mag}}}\right)\dot{y}_{\mathrm{E}}, \tag{5.4}$$

where K is a coefficient that depends on the geometric and magnetic properties. In fact, this is adjusted through a calibration against the experimental data, since numerical simulations do not account for 3D effects, yielding $K = 4.8\mathrm{N/A}$. Finally, a counteracting force will be acting on the wing:

$$F^{\mathrm{EC}} = K\sin\left(\frac{\pi y_{E}}{h_{\mathrm{mag}}}\right)I \tag{5.5}$$

where I is the electric current induced within the circuit.

Focusing on the case where $U = 4\mathrm{m/s}$, for which the highest power output is obtained experimentally, an example of the wing kinematics computed by the model was shown in Fig. 2.3 for $R_{\mathrm{L}} = 1\mathrm{k}\Omega$. In terms of flapping frequency, the model is found to underestimate it of about 3% compared to the experimental one, which is about 13.5Hz. The time history of the voltage provided by our approach is compared with the experimental one in Fig. 5.8, where we can observe that some differences exist in the signal shape, although the peaks are captured quite well. Nevertheless, we consider the agreement to be satisfactory for our purpose.

Subsequently, we employ the model to investigate cases within the same range of

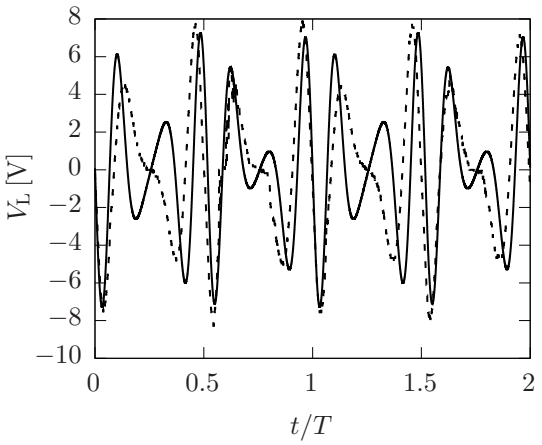

FIGURE 5.8: Time history of the voltage at the load ends for the case: $U = 4$m/s, $R_L = 1$kΩ. Comparison between experiment (dashed line) and phenomenological model (solid line).

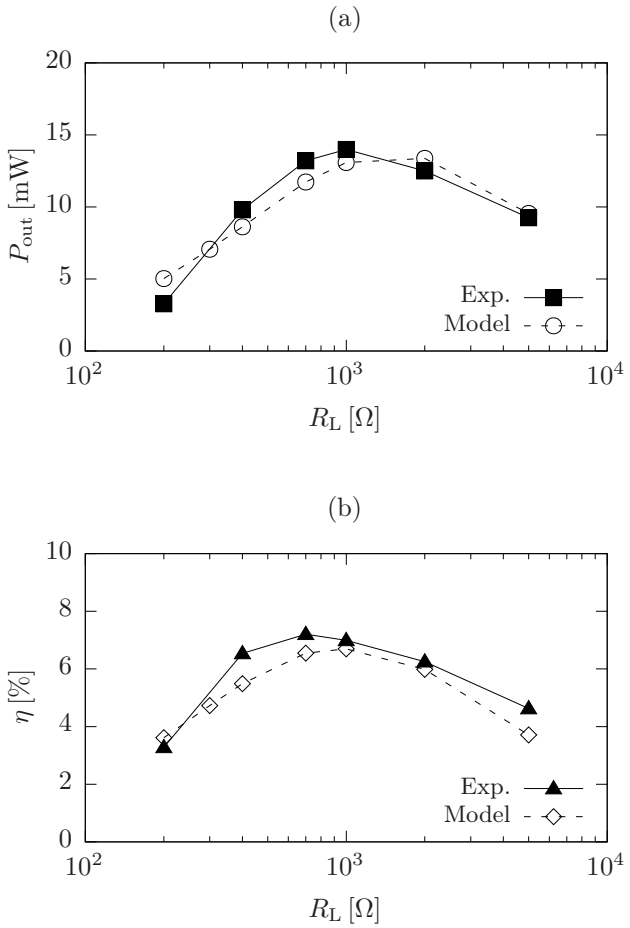

FIGURE 5.9: Results by the phenomenological model (empty symbols) compared with the experimental ones (filled symbols), as a function of the resistive load, for $U = 4$m/s: (a) mean output power; (b) global efficiency (computed using Eq. (5.6)).

R_{L} as in the experiments. Along with the extracted power (Fig. 5.9a), we evaluate the global efficiency of the system (Fig. 5.9b), defined as

$$\eta = \frac{P_{\mathrm{out}}}{\frac{1}{2}\,\rho_{\mathrm{f}}\,U^3\,A_{\mathrm{swept}}}, \tag{5.6}$$

where $A_{\mathrm{swept}} = s\,d$ and d is the vertical displacement swept by the wing (taken as the maximum between the leading and trailing edge oscillation amplitude; in the experiments, an estimation is performed using a high definition camera and digital processing).

Looking at Fig. 5.9, good agreement is found between the analytical and experimental results, both for power and efficiency. Resulting values for η are between 3 and 7%. Moreover, one can argue from the plots that the optimal value of R_{L} maximizing the efficiency is slightly lower than the one corresponding to maximum power. Note that in order to increase the efficiency and/or the energy extraction, further improvements are sought by the adoption of elastomeric capacitors, in place of the current elastomers, to be used jointly with the electromagnetic coupling [7]. On the other hand, the development of adequate electronics, in order to handle in an optimal way the energy extraction, represents a crucial aspect [9].

In conclusion, the phenomenological model here presented turns out to capture also the essential aspects of the complete electroaeroelastic system. Although its predictive capability may depend on the variation range of the physical parameters, the model can provide a useful and complementary tool for the development of EH devices.

Chapter 6

Interaction between multiple plates

The goal of the present Chapter is to provide a fundamental study on the behaviour of multiple elastically-bounded flapping plates immersed in an incompressible laminar flow, characterizing the resulting dynamics and giving useful insights for the development of EH networks made of arrays of such devices. Having characterized the dynamics of the single device in Chapters 4 and 5, here we investigate three basic arrangements of multiple devices (shown in Fig. 6.1): (i) in-line, (ii) staggered and (iii) side-by-side.

A numerical study will be conducted by focusing on the dependence of main quantities of interest with respect to the mutual distance between devices. In light of the evidence previously supplied concerning the dependence of main flapping observables on the Reynolds number (see Sec. 5.1.1), in the following we will focus uniquely on the case at $Re = 100$. This value is selected to deal with the smoothest flow solution among the considered cases, in order to get a clearer understanding of the basic mechanisms occuring in the interaction between multiple devices. In order to corroborate the numerical results, we will also provide experimental evidence from wind-tunnel measurements pertaining to EH application.

6.1 In-line arrangement

We begin our study by considering the in-line configuration, where a second wing is placed downstream at a distance $\mathbf{r} = (0, 0, r_z)$ along the streamwise direction, as sketched in Fig. 6.1a. Here we initially perturb only the upstream wing to evidence

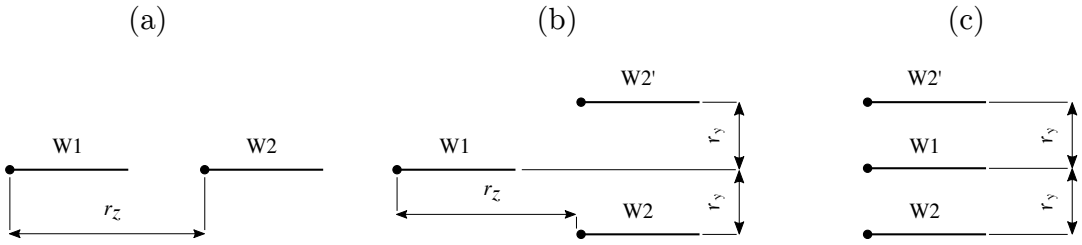

FIGURE 6.1: Sketch of configurations investigated for multiple flapping wings: (a) in-line arrangement; (b) staggered arrangement; (c) side-by-side arrangement.

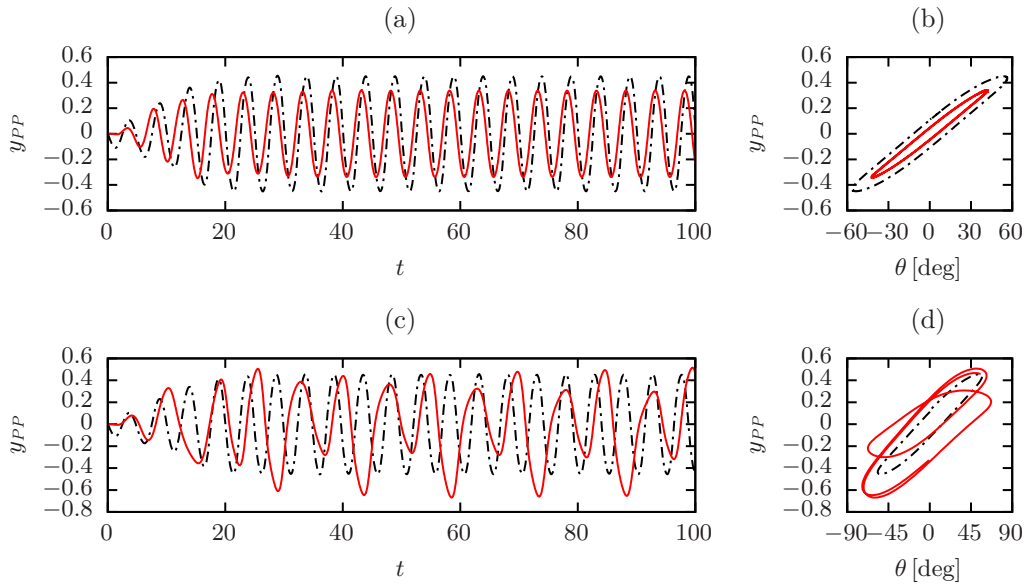

FIGURE 6.2: Time history of transverse PP oscillation (left panels) and steady-state LCO in (θ, y_{PP}) plane (right panels) for two devices in-line configuration with $r_z = 2$, (a,b) $K_{(1)} = K_{(2)} = 3$ and (c,d) $K_{(1)} = 3$, $K_{(2)} = 1$. Black dot-dashed line: upstream wing (W1); red solid line: downstream wing (W2).

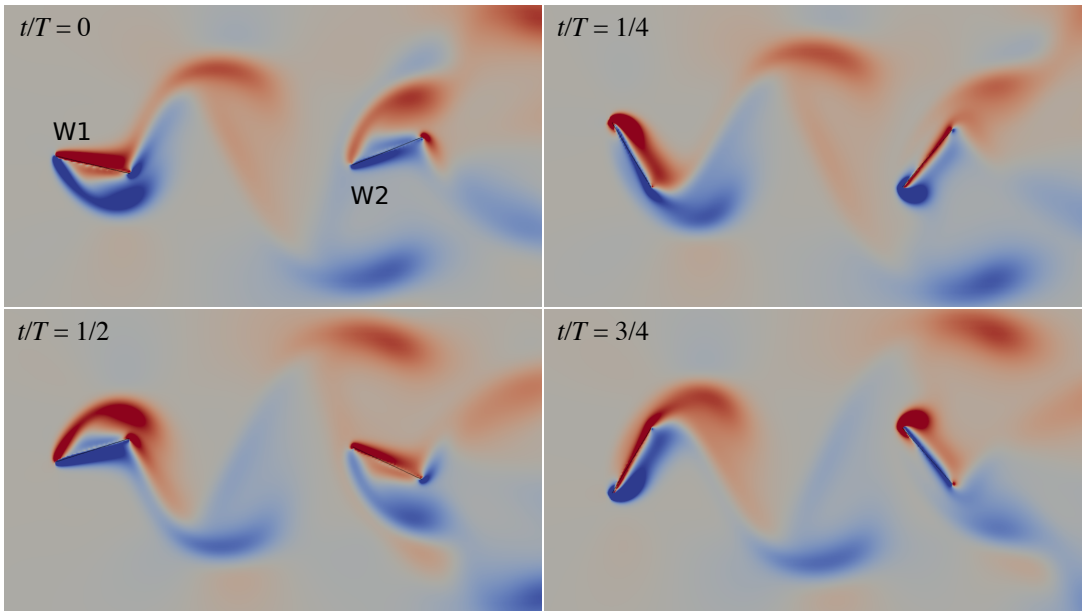

FIGURE 6.3: Instantaneous views of plate position and vorticity field [negative values (i.e. counterclockwise) in blue, positive ones (i.e. clockwise) in red] over one flapping cycle for the in-line arrangement with $r_z = 4$ and $K_{(1)} = K_{(2)} = 3$.

how the downstream wing dynamics is affected by the impacting wake. To accommodate a second downstream device, the domain is enlarged in the streamwise direction up to $z = 20$.

To start our analysis, we fix $K = 3$ for both devices, since this was found to be the most efficient condition (i.e., maximising η) in the case of the single device, and perform simulations for different values of the relative distance r_z (see Fig. 6.1a). An insight of the resulting dynamics for the case $r_z = 2$ is given by the top panels of Fig. 6.2. Looking at the time trace of the plunging motion (Fig. 6.2a), after a short transient (about 2 cycles) a phase shift is established between the oscillations of the two devices. In the new flapping state, the motion of the downstream wing gets synchronized to the wake released by the upstream one, the pitching motion being driven by low-pressure vortical regions, as it can be observed from Fig. 6.3, showing instantaneous views of the vorticity field within one flapping cycle. Furthermore, from the shape of limit-cycles reported in Fig. 6.2b, we note that the state-space trajectory of the second device is contained within that of the upstream device.

Similar findings are obtained when varying the distance r_z, as shown in Fig. 6.4: the downstream device always oscillates with amplitude smaller than the upstream one (Fig. 6.4a), with a monotonic trend that seems to recover the single-device behaviour for large r_z, as expected. The flapping frequencies of the two devices, shown in Fig. 6.4b, are essentially locked to each other and slightly decreasing for shorter separation distances, reflecting a small alteration of the upstream wing dynamics as

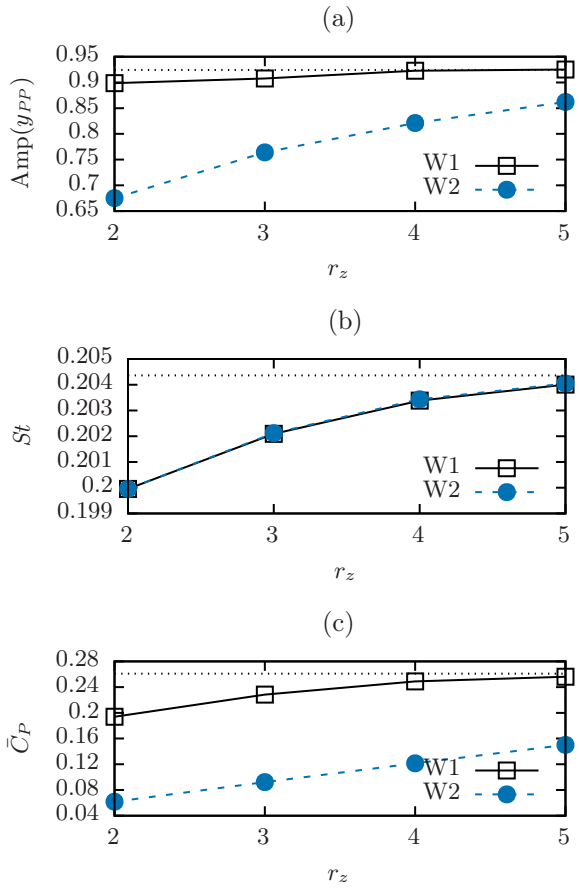

FIGURE 6.4: Flapping observables for in-line arrangement as a function of the distance between the two wings: (a) PP transverse oscillation amplitude, (b) Strouhal number and (c) power coefficient. Solid line and empty squares: upstream wing (W1); dashed line and filled circles: downstream wing (W2); dotted line: values for the isolated, single device.

well. Finally, the power coefficient shows a similar trend (Fig. 6.4c), although the difference with respect to the single configuration is more pronounced: in fact, this quantity involves the product between the lift force and the PP velocity, both being weakened.

6.1.1 Structural tuning of downstream device

In order to improve the performance of the downstream device, we investigate the configuration in which the value of its stiffness $K_{(2)}$ is varied, while for the upstream device it is kept fixed to $K_{(1)} = 3$. Two streamwise distances are considered, i.e. $r_z = \{2, 4\}$. Similarly to the previous case, the flapping observables are reported in Fig. 6.5. The plunge motion increases its amplitude for decreasing $K_{(2)}$, attaining values close to the device in the single configuration (Fig. 6.5a). Conversely, the Strouhal number (Fig. 6.5b) decreases while softening the spring for $K_{(2)} < K_{(1)} = 3$. In this range, the resulting dynamics is a nonlinear combination of the self-excitation, taking place in uniform flow, and the wake-forcing mechanism previously discussed.

Bottom panels of Fig. 6.2 show the resulting flapping in time for a representative case, where one can notice the larger amplitude of both pitch and plunge compared to the corresponding case with $K_2 = K_1$. Furthermore, for this particular case ($r_z = 2$, $K_2 = 1$), one can see that the system shows asymmetric and multiperiodic oscillation of the pivot-point (Fig. 6.2c,d). Indeed, it was observed that when $K_{(2)} < K_{(1)}$ the spectral content is richer and the dominant frequency is altered compared to the single flapping wing at $K = K_{(2)}$.

For $K_{(2)} > K_{(1)} = 3$, the flapping frequency remains locked to the upstream wing. The downstream wing oscillation decreases while increasing $K_{(2)}$ but flapping now occurs also for $K_{(2)} > K_{\mathrm{cr}} \approx 4.7$, unlike what happens in the case of an isolated device. In this case, the only mechanism causing such motion is wake forcing.

A recovery in the value of the power coefficient is obtained by lowering K_2, as shown in Fig. 6.5c, which is beneficial from the EH perspective, although in none of the considered cases the same amount as for the single device was obtained. Our numerical results can be compared with the experimental evidence recently presented in Ref. [38], where the idea of tuning the pitching stiffness of the downstream wing was proposed for pitch-and-plunge EH systems: despite the different structural features (e.g., the presence of restoring moments both in plunging and pitching) and the significant difference in Reynolds numbers considered, a qualitative analogy can be drawn.

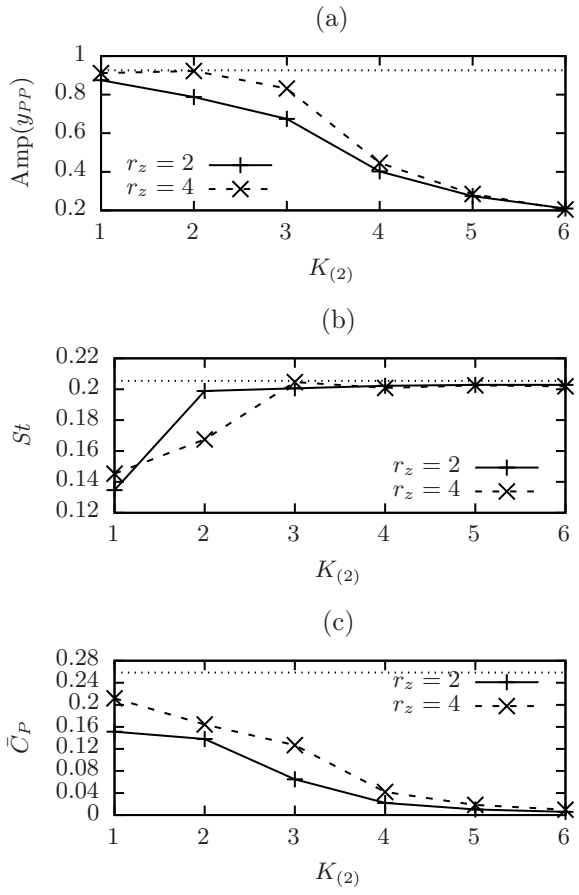

FIGURE 6.5: Flapping observables of downstream wing in in-line arrangement with tuning of its stiffness, as a function of this latter: (a) PP transverse oscillation amplitude, (b) Strouhal number and (c) power coefficient. Solid line and +'s: $r_z = 2$; dashed line and x's: $r_z = 4$; dotted line: values for single-device configuration with $K = 3$.

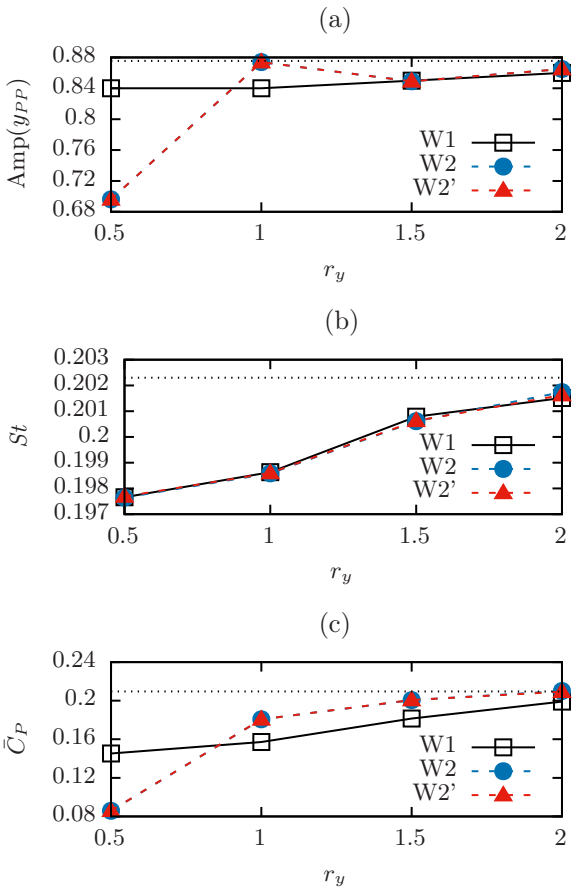

FIGURE 6.6: Flapping observables for staggered arrangement (Fig. 6.1b), as a function of the transverse distance between devices: (a) PP transverse oscillation amplitude, (b) Strouhal number and (c) power coefficient. Black solid line and empty squares: W1; blue dashed line and filled circles: W2; red dashed line and filled triangles: W2'; black dotted line: values for single-device configuration with $K = K_{(1)} = 3$.

6.2 Staggered arrangement

In the staggered arrangement, shown in Fig. 6.1b, a pair of devices (W2 and W2') is placed aft of the first one (W1) at a distance $\mathbf{r} = (0, \pm r_y, r_z)$. We choose the closest streamwise distance considered for the in-line case, i.e. $r_z = 2$, and investigate the behaviour for different values of the transverse distance $r_y = \{0.5, 1, 1.5, 2\}$.

Results of the analysis are presented in Fig. 6.6. Concerning the plunging amplitude (Fig. 6.6a), an attenuation is found with respect to the single-device configuration for all devices, which is however limited for W1 to about 5%, while for W2 and W2' we have a relative peak at $r_y = 1$ (approaching the value in single configuration) and a sharp decrease for $r_y = 0.5$ (about 20%). In the latter, the downstream wings are found to lie entirely within the wake released by W1, the oscillation being reduced in a way similar to what reported for the in-line arrangement, featuring the same synchronization mechanism. For $r_y = 1$, the wake is impacting on downstream devices only during a portion of the flapping cycle, yielding a different dynamics: the flapping motions are collectively in-phase, as shown by Fig. 6.7, and the occurring interference is presumably responsible for the relative peak in amplitude. Increasing the distance to $r_y = 1.5$ and 2, the same in-phase motion is still observed but W2 and W2' are now located outside the wake region and consequently the weakly constructive interference is not present anymore.

Note that for W2 and W2' the flapping motion is asymmetric with respect to the streamwise direction but substantially specular with respect to each other. The Strouhal number shows almost negligible variations (less than 5%) compared to the single-device configuration, decreasing for smaller r_y (Fig. 6.6b). Values of the power coefficient are always found to be lower than that of the isolated device. We note however that, for $r_y > 1$, the power coefficient is found to be higher for downstream devices (Fig. 6.6c).

6.3 Side-by-side arrangement

We now focus on the side-by-side arrangement, where we place a pair of devices (W2 and W2') at a transverse distance $\mathbf{r} = (0, \pm r_y, 0)$ with respect to the central one (W1), as sketched in Fig. 6.1c. As for the other two arrangements, only the first wing is initially perturbed.

Flapping observables from numerical simulations considering three different values of the mutual distance, i.e. $r_y = \{1, 1.5, 2\}$, are reported in Fig. 6.8. Looking at the plunging amplitude (Fig. 6.8a), for sufficiently small separations (i.e. $r_y \leq 1.5$) the resulting values are larger than that obtained for the single device, although the relative increment is only up to about 8% for W1 and 20% for W2 and W2'. The

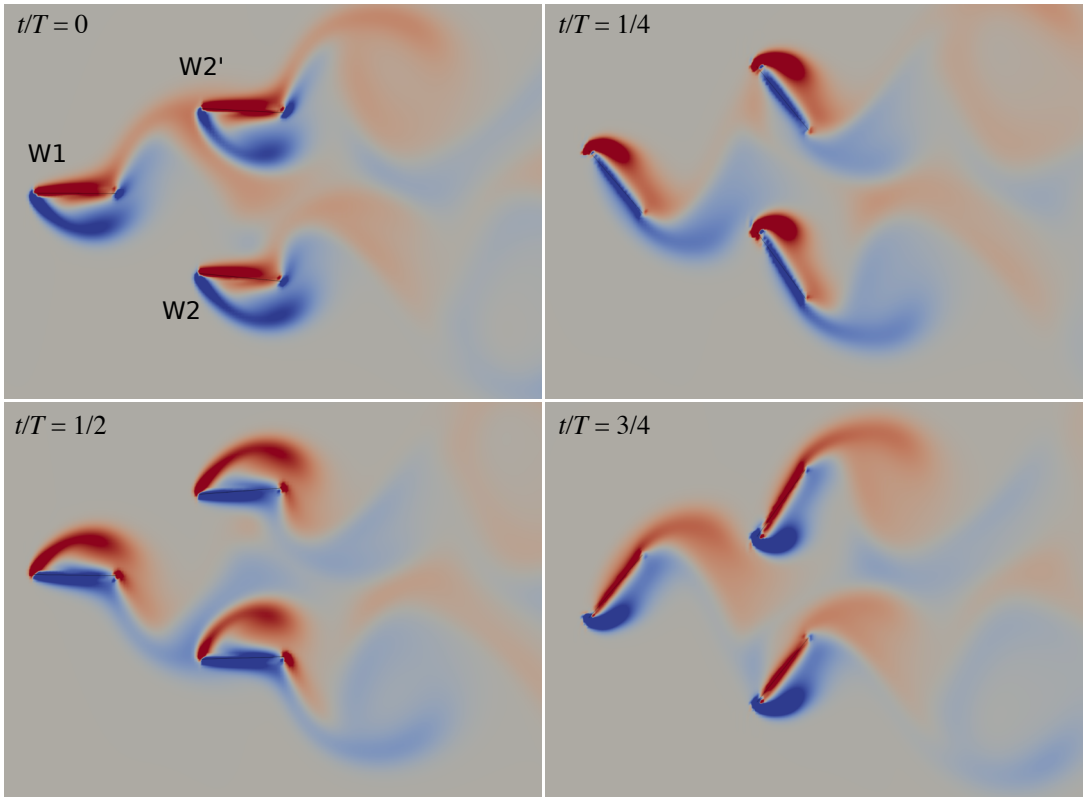

FIGURE 6.7: Instantaneous views of plate position and vorticity field [negative values (i.e. counterclockwise) in blue, positive ones (i.e. clockwise) in red] over one flapping cycle for the staggered arrangement with $r_y = 1$ and $r_z = 2$.

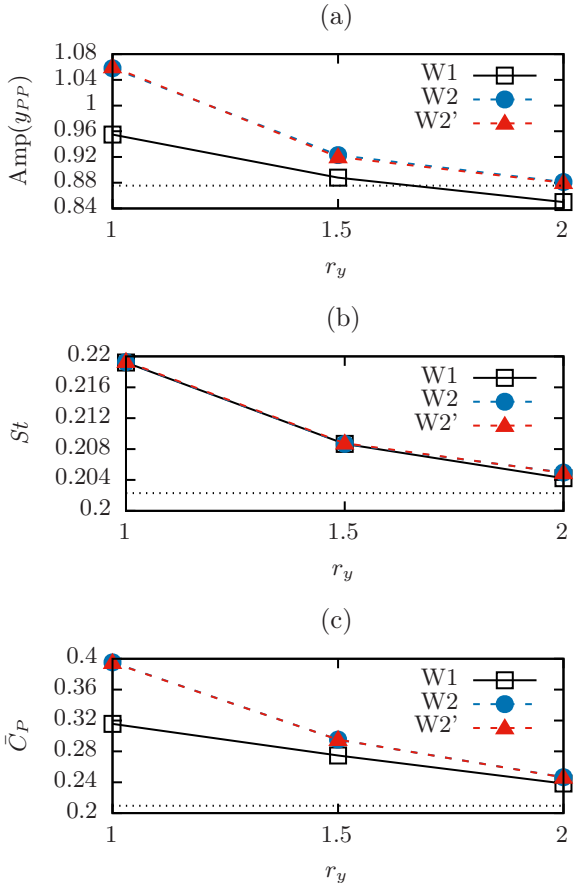

FIGURE 6.8: Flapping observables for side-by-side arrangement (Fig. 6.1c), as a function of the transverse distance between devices: (a) PP transverse oscillation amplitude, (b) Strouhal number and (c) power coefficient. Black solid line and empty squares: W1; blue dashed line and filled circles: W2; red dashed line and filled triangles: W2'; black dotted line: single-device configuration.

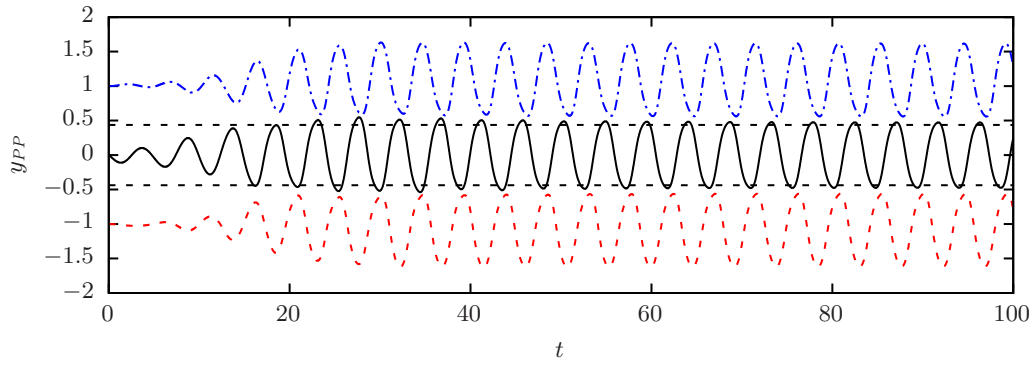

FIGURE 6.9: Time history of transverse PP oscillation for devices in side-by-side arrangement with $r_y = 1$. Black solid line: W1; red dashed line: W2; blue dot-dashed line: W2'. Black dashed lines report the maximum and minimum of PP oscillation in the single configuration.

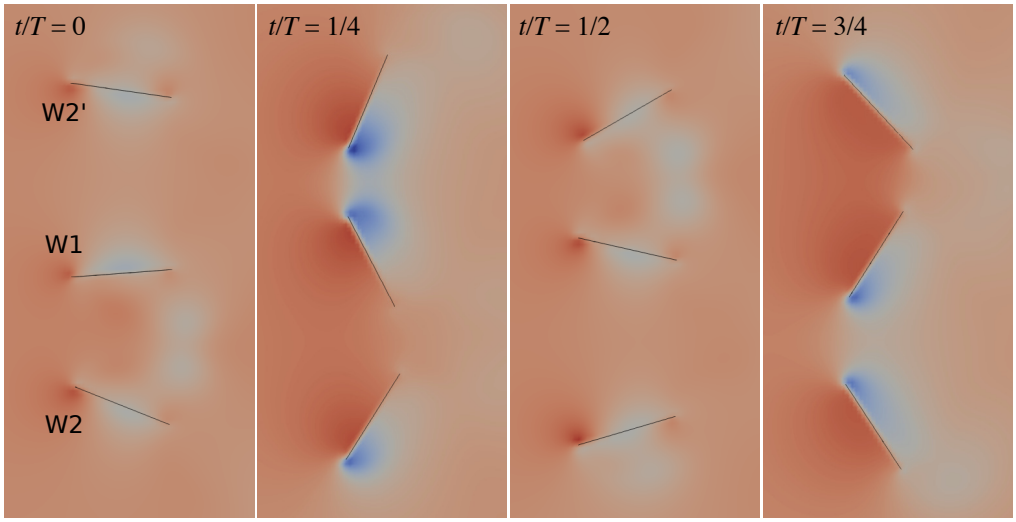

FIGURE 6.10: Instantaneous views of plate position and pressure field [negative values in blue, positive ones in red] over one flapping cycle for the side-by-side arrangement with $r_y = 1.5$.

flapping frequency is nearly identical for the three devices and slightly increases while decreasing r_y, up to about 5% when $r_y = 1$ (Fig. 6.8b). Despite the relatively small variation of these two quantities, a significant increase of the power coefficient occurs for all flapping plates (Fig. 6.8c): with respect to the single device, for the central wing the increase is almost 50%, while for the side wings this reaches nearly 90%.

Similarly to what it was observed for the staggered arrangement (Sec. 6.2), the central wing undergoes symmetrical motion while the side wings exhibit slightly asymmetrical flapping, as it can be observed from the time traces of the transverse PP displacement reported in Fig. 6.9. Moreover, the steady-state oscillations of the side wings are approximately in-phase with respect to each other and in counter-phase with respect to the central wing. From the qualitative viewpoint, we can observe how the resulting scenario resembles the counter-phase flapping regime observed for flexible bodies placed at moderate distances [95, 26, 35].

The described dynamics is supported by Fig. 6.10, where the position of the three wings along with the pressure field at different instants within one flapping cycle is shown. From these snapshots, we argue that when two adjacent wings get closer (approximately when the pitching angle is at its maximum/minimum), the flow velocity has to increase due to the narrower effective cross section; hence, the pressure minimum gets amplified compared to the single case, this in turns increasing the amplitude of the lift force and, consequently, the wing oscillation.

In Fig. 6.9, the PP oscillation amplitude of W1 is compared to that of the isolated case. As mentioned before, the variation of this quantity does not provide a

direct indication of the gain in performance that is achieved employing this configuration. To perform a more detailed comparison, let us focus on the quantities that are directly associated with the plunge power, whose time evolutions are reported in Fig. 6.11. The first one is the PP transverse velocity (Fig. 6.11a), for which the observed difference, in terms of amplitude, is about 20% for all wings. The second is the lift coefficient (defined as $C_L = 2\,F^y_{\text{aero}}/(\rho_{\text{f}} csU^2)$), shown in Fig. 6.11b, for which the variation is approximately 20% for W1 and 40% for the side wings. For the latter, the increment is even more pronounced since the flapping motion is asymmetric, so that higher positive (or negative) peaks of C_L are found for the top (or bottom) wing. By multiplying these two quantities, we obtain the instantaneous power coefficient reported in Fig. 6.11c, where one can see how the positive peaks in the side-by-side configuration are appreciably higher than in the single case, while the negative peaks remain essentially at the same values. Consequently, the average power coefficient undergoes the significant increase already presented in Fig. 6.8c.

In light of these results, we move further by considering arrays of more than three objects, fixing the mutual distance between adjacent devices to $r_y = 1$, for which we found the highest increase in performance. The outcome of this analysis is presented by Fig. 6.12 collecting the average power coefficient for each device: when placing two additional plates at $y = \pm 2$ (i.e., considering an array of $N_{\text{d}} = 5$ devices), these achieve a further enhanced performance compared to the case where $N_{\text{d}} = 3$. The same trend holds when increasing the number of devices to $N_{\text{d}} = 11$. Increasing N_{d}, the motion of flapping objects may be found to be less regular and periodic, as e.g. for the side wing placed at $y = 5$. Consequently, we evaluate the average in a statistical sense by assessing its convergence in time.

Emphasizing the comparison with the total power that could be expected considering N_{d} isolated devices, we can write the overall power coefficient associated with the whole array $\bar{C}_P^{\text{tot}}$ as:

$$\bar{C}_P^{\text{tot}} = \sum_{i=1}^{N_{\text{d}}} \bar{C}_P = N_{\text{d}} \bar{C}_P^{\text{S}} + I, \tag{6.1}$$

where $\bar{C}_P^{\text{S}}$ is the power coefficient of the single device (in isolated configuration) and the interference quantity $I = I(N_{\text{d}})$ has been introduced. The latter quantifies the additional power due to the cooperative effect. Similarly, the relative increment can be expressed by introducing the interference factor

$$IF = \frac{I}{N_{\text{d}} \bar{C}_P^{\text{S}}}. \tag{6.2}$$

Table 6.1 collects the values obtained from our computations, from which *IF* seems

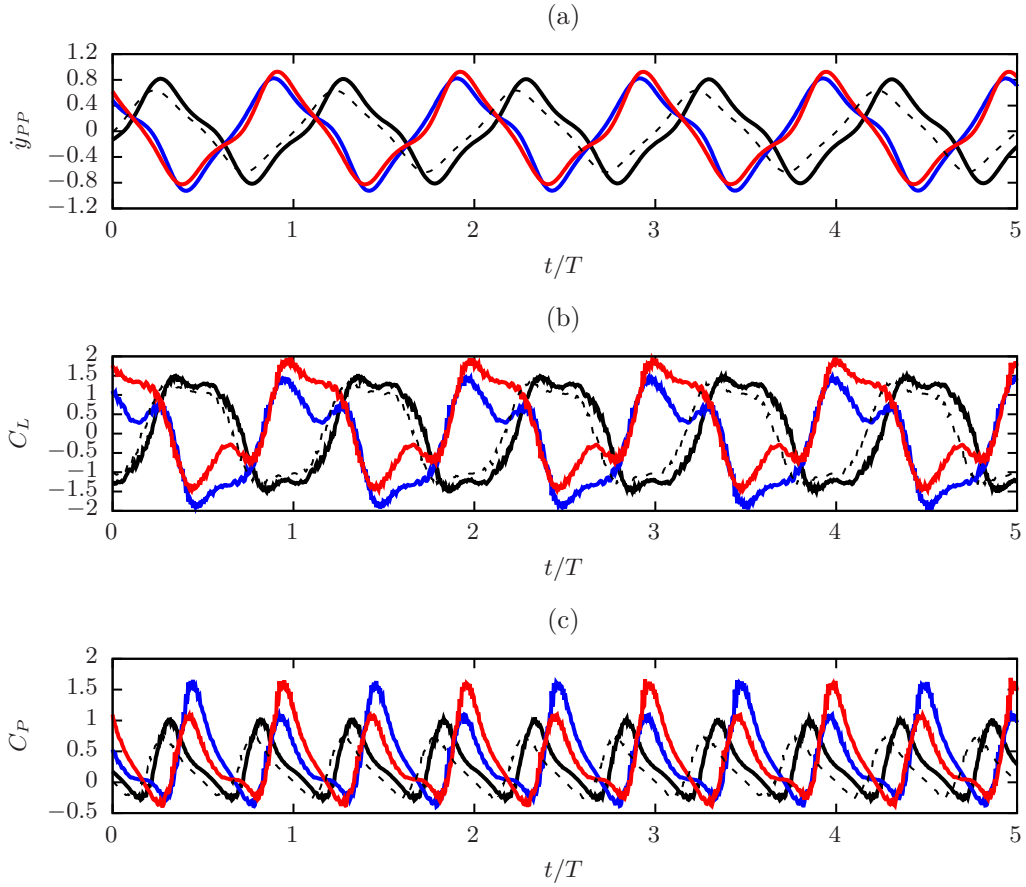

FIGURE 6.11: Time histories of (a) PP transverse velocity, (b) lift coefficient and (c) instantaneous plunge power coefficient, comparing the central (W1, black), bottom (W2, blue) and top (W2', red) wings in side-by-side arrangement with $r_y = 1$ (solid line) and the same device in single configuration (dashed line). Time is normalized by the corresponding period of flapping motion.

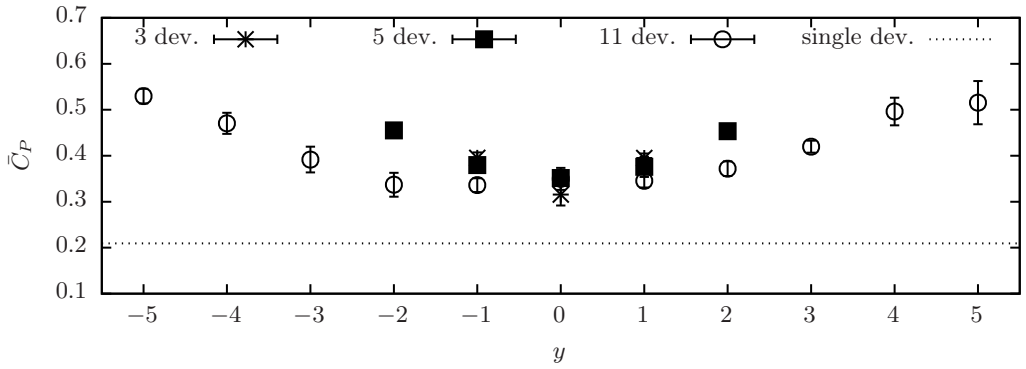

FIGURE 6.12: Power coefficient distribution for side-by-side arrangements with different number of devices, placed at mutual transverse distance $r_y = 1$. Error bars indicate the variation in the performed cumulative average due to non-regular flapping.

TABLE 6.1: Performance of side-by-side arrays with different number of devices N_d; $\bar{C}_P^{\mathrm{tot}}$ is the total power coefficient of the array (Eq. (6.1)) and IF is the interference factor as defined by Eq. (6.2).

N_d	$\bar{C}_P^{\mathrm{tot}}$	IF
3	1.10	0.76
5	2.01	0.92
11	4.56	0.98

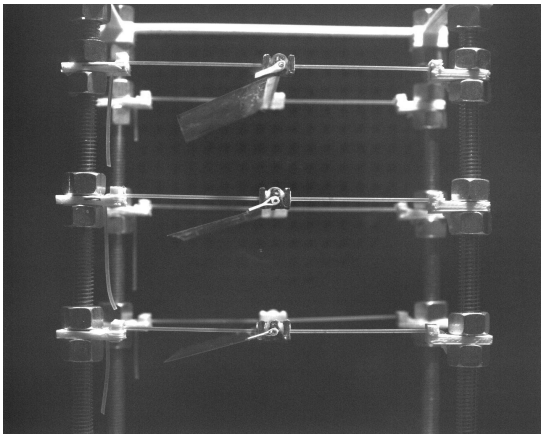

FIGURE 6.13: Side view of the experimental realization of side-by-side array, made by three elastically-bounded plates, tested in the wind tunnel.

to converge with the number of devices approximately to unity, i.e. the amount of available power is almost 100% increased compared to the sum of N_d isolated devices. Moreover, this evidence can be representative when extrapolating our results to the situation of a network made of a vast number of devices. In this situation the side effects, although beneficial in terms of performance, are expected to be negligible. Nevertheless, each device can be thought to behave as those in the central part of the array. We can therefore conclude that employing a side-by-side arrangement of many devices appears to be substantially beneficial in terms of EH potential.

6.3.1 Wind-tunnel experiments

In order to corroborate the numerical findings, our study is complemented by an experimental study on an array of three devices in the side-by-side arrangement, shown in Fig. 6.13.

Each of the three devices composing the array is similar to those already described in this work (see e.g. Sec. 5.2.1) and also presented in Refs. [59, 62]. A 0.1mm-thick foil made of polyvinil acetate, with planform dimensions $c = 30$mm and $s = 65$mm,

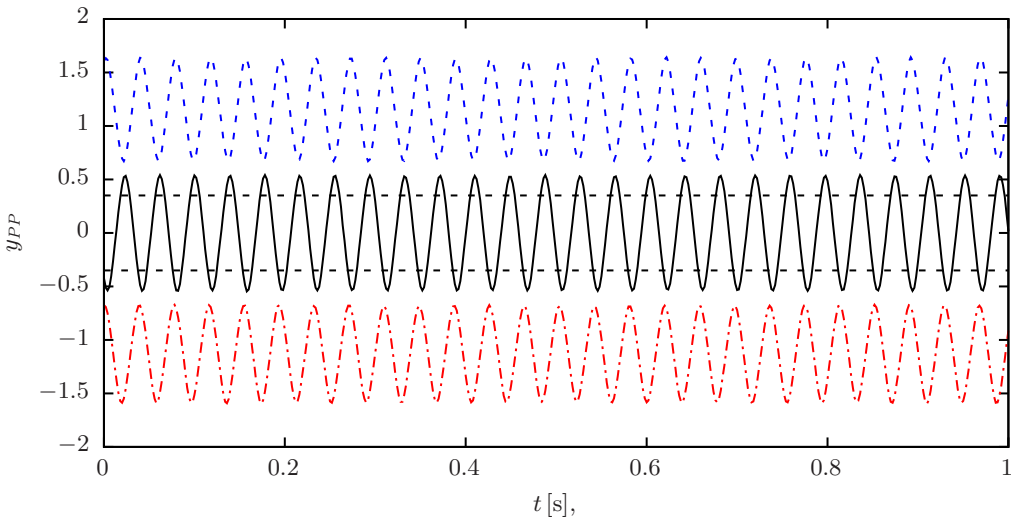

FIGURE 6.14: Time history of transverse PP oscillation for the experimental array of three devices in side-by-side arrangement (Fig. 6.13). Black solid line: W1; red dot-dashed line: W2; blue dashed line: W2'. Black dashed lines indicate maximum and minimum displacement of W1 in the single configuration.

is glued to a brass rod that is connected (allowing free rotation) to four elastomeric elements made of siliconic rubber, aligned with the streamwise direction and pre-stretched so that, following Eq. (4.6), the value of the effective stiffness is about $\mathcal{K}_{(y)}^{\text{eff}} \approx 13\text{N/m}$. The mass of the moving body is $m = 0.94\text{g}$ and the center of mass is approximately placed $0.2c$ aft of the leading edge.

Experiments were performed following the procedure that has been described in Sec. 3.2. The three devices are collocated within a fixed frame and placed approximately at the center of the test chamber. The mutual distance between devices is $r_y \approx 1.1$. A freestream air velocity $U = 4.5\text{m/s}$ is chosen, at which regular LCO was found for devices tested in the single configuration.

Assuming air at standard conditions, the chord-based Reynolds number can be estimated as $Re \approx 9 \times 10^3$, while from the other quantities we can derive the remaining equivalent nondimensional parameters: $\mathcal{AR} \approx 2$, $\rho_{\text{w}} \approx 17$ and $K \approx 21$. Except for the aspect ratio, these values are clearly different from those considered in the numerical investigation. The analysis is thus intended as complementary, in order to assess the robustness of the outlined mechanism when moving into the operational range of the real EH application.

The experiment has been conducted as follows. First, we performed measurements of each device taken individually, i.e. removing the other two from the array and retaining the device under consideration in the same position as in the multiple configuration. Then, we tested the multiple configuration, where all three devices are present.

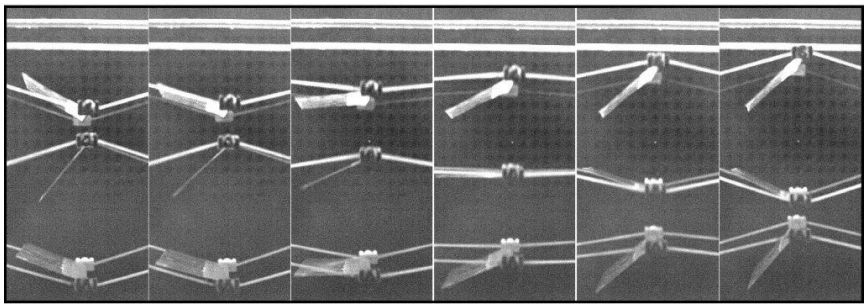

FIGURE 6.15: Side views of the experimental side-by-side arrangement of three devices during collective flapping motion (the wind is coming from the right and the time interval between frames is 4ms).

TABLE 6.2: Flapping observables for the experimental array of three devices in side-by-side arrangement. The suffix denotes values for the single (S) or the array (A) configuration.

Device	$\mathrm{Amp}(y_{PP})^{\mathrm{S}}$	$\mathrm{Amp}(y_{PP})^{\mathrm{A}}$	St^{S}	St^{A}	$\bar{C}_P^{\mathrm{S}}$	$\bar{C}_P^{\mathrm{A}}$
W2'	0.69	0.97	0.16	0.17	0.13	0.30
W1	0.73	1.07	0.16	0.17	0.16	0.43
W2	0.83	0.9	0.17	0.17	0.23	0.29

The time traces of the acquired PP oscillation for each device are reported in Fig. 6.14, where it appears that the behaviour is analogous to that observed numerically: the amplitude of the oscillation increases and the flapping motions of adjacent wings are essentially in counterphase, as it is also shown by the side views of Fig. 6.15.

To quantify the effect due to the mutual interaction, Table 6.2 reports values of the same observables analysed numerically, i.e. amplitude of PP oscillation, Strouhal number and power coefficient, both for the single and multiple configurations. Focusing on data of the single configuration, we observe that a certain difference exists between the three devices, which can be ascribed to constructive details. Nevertheless, when considering the same quantities in the multiple configuration, an increase with respect to the single case is found for all devices. In particular, the PP amplitude is maximised for the central wing (W1), with an increase around 40% with respect to the individual configuration. Variation in frequency is smaller, i.e. between 2 and 10% with the same resulting synchronisation between devices that is observed numerically. From the acquired movies it is also possible to evaluate the aerodynamic forces and thus the power associated to the plunge and pitch motions. In Table 6.2, we report the cycle-averaged plunge power coefficient, as defined in Eq. (5.1). The increment when the three wings are coupled is evident, confirming qualitatively the results obtained by the simulations.

Chapter 7

Conclusions and outlook

This work has investigated the dynamics of an aeroelastic system, based on the fluttering oscillations of elastically-bounded plates interacting with laminar flow, suitable for energy harvesting applications.

To support the experimental development and capture the essential physics involved, we have considered an effective physical model where homogeneous plates are anchored by linear springs and immersed in uniform flow. By employing a finite-difference Navier-Stokes solver coupled with a moving-least-squares immersed boundary method, we have performed numerical simulations for the single and multiple wing configurations. Such approach has been proven to be particularly suitable for problems with many moving and/or deformable objects. Along with this methodology, we have also presented evidence from wind-tunnel experiments as well as by a reduced-order, quasi-steady phenomenological model that has been employed with success in similar fluid-structure interaction problems.

This study has addressed three key features which can be summarized along with the corresponding main outcomes:

1. We have identified the critical condition for self-sustained flapping using a simple balance between characteristic timescales.

2. We have explored postcritical regimes characterized by regular limit-cycle oscillations, highlighting how to maximize their amplitude and in turns the mechanical power.

3. We have investigated the dynamics of arrays of multiple devices, revealing how substantial performance improvements can be obtained using certain arrangements.

Overall, useful insights have been supplied that can support the design of efficient EH devices based on elastically-bounded flapping plates.

As a first step, we have focused on how to predict the onset of self-sustained oscillating motion and therefore deduce an expression for the critical flow velocity U_{cr} (or, equivalently, in terms of the nondimensional stiffness K_{cr}), above (below) which unstable flapping states are found. Both numerical and experimental evidence are in agreement with the theoretical prediction obtained by a balance condition between the natural frequency of the system and the so-called wind vane frequency (i.e., the characteristic frequency when a rigid plate is hinged at a pivot point and immersed in an incompressible flow). This finding has practical relevance, since the critical velocity for sustained flapping represents the lower threshold of the operational flow velocity range.

Once identified the critical condition for flapping, the second step has regarded the analysis of the postcritical regime, i.e. the region $U > U_{\mathrm{cr}}$ (or, equivalently, $K < K_{\mathrm{cr}}$), where the nonlinear aspects become crucial and LCOs emerge. Focusing on regular oscillations which are of greater interest for EH, we carried out a parametric investigation first assessing the role of the governing parameters (Re, K and ρ_{w}), and then also considering the presence of an additional mass on the plate. Despite the simplicity of the model, this latter configuration turns out to capture the essential behavior that is observed experimentally for the real device, including the appearance of optimal conditions with maxima of the oscillation and power extraction at intermediate K. Moreover, the quasi-steady phenomenological modeling strategy has been successfully applied to reproduce the experimental data and provide an analytical description from which further information can be obtained.

The third aspect has been investigated by considering three basic arrangements of multiple devices: (i) in-line, (ii) staggered and (iii) side-by-side. We investigated how the dynamical behavior is affected by the mutual distance at which devices are placed in the multiple configuration. For both the in-line and staggered arrangements, the performance of interacting devices is found to be worse than in the single case, although a recovery in performance can be achieved by tuning the elasticity of downstream devices. When considering the side-by-side configuration, in contrast, the interaction turns out to be beneficial and relevant increases of the power coefficient are found. Further enhancements are obtained when increasing the number of devices in the array. A constructive interference is found, causing the total power coefficient of the network to increase up to 100% with respect to the expected amount by the

same number of isolated devices. The occurrence of this cooperative effect has been verified experimentally considering an array of prototypal devices in complementary conditions. Our results therefore suggest the development of dense arrays of devices as a strategy that could enable higher EH performance.

We conclude by pointing out open issues that could foster future developments along this line of research. These include points that have not been fully addressed so far, as well as other aspects that remain completely unexplored:

- Understand in more detail the optimal condition that has been observed in the postcritical flapping states of the plate with additional mass (Sec. 5.1.3) as well as in the experimental configuration (Sec. 5.2.1).
- Explore other arrangements for multiple devices, e.g. placing several ones also along the spanwise direction (not considered here), in order to outline a fully three-dimensional EH network concept.
- Include the presence of the energy extraction stage in the fully-resolved numerical simulations by means of a proper modeling strategy, such as an additional ODE mimicking the connected electrical circuit.
- Consider a turbulent incoming flow, which is a typical condition of many real-world environments (e.g., atmospheric or oceanic currents) and investigate the behavior of the elastically-bounded flapping plates in this condition.

Summary of other research activity

Besides the one addressed by this Thesis, the work that has been developed during this Ph.D. project concerned also other topics related to fluid-structure interaction, transport phenomena, turbulence and particle-laden flows. In this annex, a short description of such activity and related outcomes is provided.

Passive control by appendages behind bluff bodies [41]

Sophisticated flow control techniques are used by organisms of various kind, including both motile animals and non-motile seeds, to improve their locomotion. To increase our understanding of such mechanisms, we have investigated the problem by focusing on passive lift/drag control by means of three-dimensional elliptic-shaped appendages behind a sphere at moderate Reynolds number flow conditions (Fig. 1).

Our starting point is the semi-empirical model proposed by Lācis et al. [40], for the two-dimensional case where a simple splitter plate was attached behind a circular cylinder falling in still fluid, revealing an *inverted-pendulum-like* (IPL) instability which leads to reorientation of the body and passive dispersion, i.e. drift with respect to the direction of gravity.

We have extended this work characterizing the described fluid-structure interaction in a three-dimensional situation by carrying out numerical simulations over a wide range of the appendage aspect ratio. Results show that the presence of the IPL instability persists also in the 3-D case, despite the more complex wake topology, for a wide range of appendages. Hence, the IPL model is used to explain, from a qualitative viewpoint, the mechanisms underlying the observed evidence. Furthermore, from the systematic parametric investigation over the aspect ratio and length of appendages, we are also able to identify the one giving the largest drift angle of the body that would be free to fall.

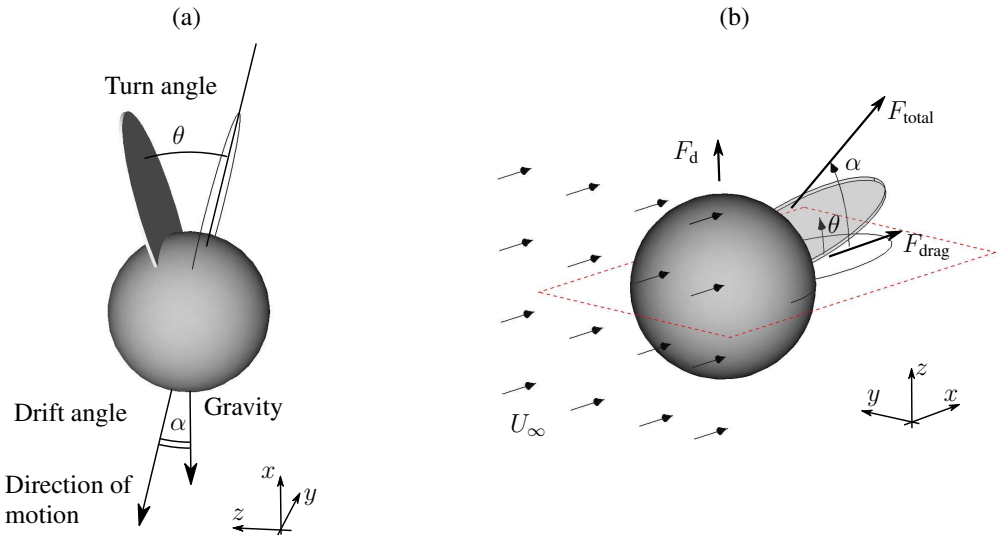

FIGURE 1: (a) Body consisting of a sphere and a planar, elliptical appendage falling freely under the influence of gravity. (b) Same body in a fixed framework, where it is exposed to a constant free-stream velocity.

Dispersion of inertial particles in turbulent flow [10]

In the early 1920s, Taylor derived what can be fairly considered one of the cornerstones of large-scale transport of tracer particles in fluid flows. In the limit of long observation time and under rather general assumptions, Taylor observed that the mean square of tracer particle displacement grows linearly in time with a rate now usually referred to as the eddy-diffusivity coefficient. Based on this observation, Taylor established a first principle identity expressing the tracer particle eddy diffusivity as a time integral of the fluid velocity autocorrelation function evaluated along the fluid trajectories. Since then, Taylor's formula has played a key role in the analysis of turbulent dispersion of tracers.

Tracer dispersion is a small subset of a much larger class of transport problems: the transport of inertial particles. Inertial particles are small particles having a finite size and/or density different from that of the carrier fluid. Our aim has been to review in a fashion independent of model details the conditions presiding over the expression of the inertial particle eddy diffusivity as an integral of the correlation functions of fluid velocity and external forces evaluated along the particle trajectories.

Thanks to our generalized Taylor formula, one can evaluate the autocorrelations and the cross correlations of flow and external forces, either through available data or from analytical dynamical models. This allows investigating how and in what regions of the flow the model terms and their mutual interactions contribute to transport, providing more physical information about the problem.

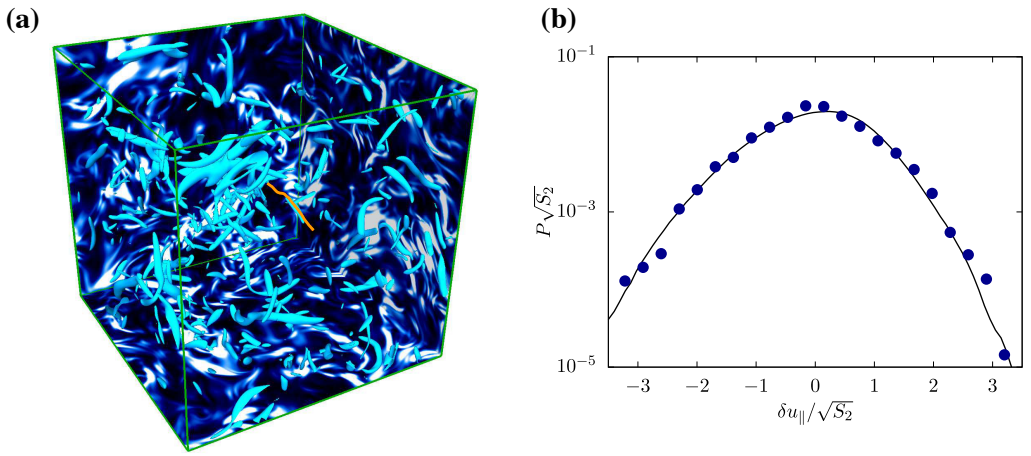

FIGURE 2: (a) Snapshot from DNS of HIT in which a flexible fiber (line in orange) is immersed, with isosurfaces of $\mathcal{Q}$ (in cyan) depicting the istantaneous vorticity field, and the three back planes coloured according to the value of the enstrophy field. (b) Probability density function (PDF) of the longitudinal velocity increments for the subcritical underdamped case $\gamma/\gamma_{\mathrm{crit}}^{\mathrm{ud}} = 0.3$. Comparison between the Lagrangian fiber measurement (bullets) and the Eulerian one (filled curve).

Lagrangian fiber tracking as a proxy of turbulent statistics and fluid velocity gradient [76, 18]

We have explored the possibility of using fiber-like objects to measure fluid flow properties in both laminar and turbulent conditions. First, we have investigated how to access the statistics of homogeneous isotropic turbulence (HIT) by considering fibers with length in the inertial range of scales (Fig. 2a). We found that the statistical properties of turbulent eddies of comparable size can be measured in a Lagrangian way by simply tracking the position and velocity difference between the fiber ends. For the case of flexible fibers, a phenomenological theory recently proposed by Rosti et al. [77] is able to predict different flapping regimes, in some of which the fiber is effectively slaved to the flow and can therefore be used to measure various two-point statistics of turbulence such as, e.g., the probability density function of longitudinal velocity increments (Fig. 2b). The predictions have been corroborated by fully-coupled direct numerical simulations employing an immersed boundary technique for the fluid-structure interaction.

When considering rigid fibers the same outcome is obtained, provided that the Stokes number is sufficiently small and that one focuses on transverse velocity differences instead of longitudinal ones. In this case, experimental evidence has also been recently obtained along with the numerical one. The results are complemented by the measurement of the eddy turnover time through the fiber tumbling time and the evaluation of the Kolmogorov constant.

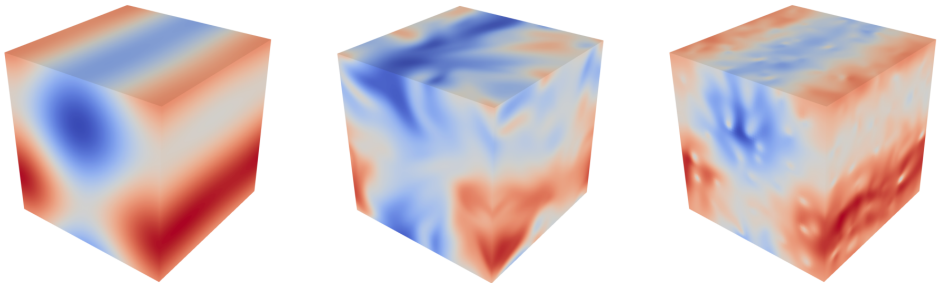

FIGURE 3: Visualizations of the velocity field for three-dimensional cellular flows. Left: stable ABC flow solution; center: unstable flow at $Re = 130$; right: the same but in the presence of a network of 6^3 fibers, leading to a steady configuration.

While for HIT the outlined strategy works only in a statistical sense, we have also studied how instantaneous measurements of the whole fluid velocity gradient can be performed by tracking assemblies of rigid fibers. This has been investigated for different classes of cellular flows (steady or time dependent, two dimensional or three dimensional) comparing the fiber-based measurement with the analytical solution for the unperturbed flow.

Overall, our results strongly suggest the possibility of using fibers (or assemblies of them) to perform multi-point flow measures, giving rise to a new 'Fiber Tracking Velocimetry' technique.

Turbulence alteration in a network of fixed fibers

We investigated how classical fluid turbulence is modified by the presence of a network of fixed fibers, as a conceptual representation of flow within a canopy. In boundary-layer meteorology, the interaction of wind with plant (or urban) canopies is known to cause modifications in the momentum and heat fluxes and velocity profiles. Moreover, such features can influence the transport and mixing properties within the canopy, consequently altering ecological mechanisms such as carbon dioxide exchange.

To this aim, we first consider a steady large-scale external forcing, for which the stable Arnold-Beltrami-Childress (ABC) solution is obtained (for a sufficiently low Reynolds number Re), and investigate the stabilizing effect of the canopy (Fig. 3). This framework enables us to obtain a clear understanding of the energy distribution across the scales of motion, and to propose an effective large-scale description by means of a simple Darcy friction term. The predicted scaling with the main parameters, e.g. fiber concentration and length, is confirmed when considering different flow configurations such as the parallel Kolmogorov flow and homogeneous isotropic turbulence, providing evidence of the same mechanisms.

List of papers and communications

The present annex reports the list of contributions, in terms of scientific articles and presentations, produced during the development of this Doctoral Thesis. These concern the topic of this dissertation as well as the other subjects on which the Candidate has actively worked as complementary research activity.

Articles on peer-reviewed scientific journals

1. S. Olivieri, G. Boccalero, A. Mazzino, and C. Boragno. "Fluttering conditions of an energy harvester for autonomous powering". *Renewable Energy* 105 (2017), pp. 530–538

   Flapping states of an energy harvesting device have been investigated by means of experiments, numerical simulations and a phenomenological model. The main aim is to predict the geometrical/physical properties of the system allowing sustained flapping limit cycles to emerge. These latter regimes are interesting when the system is used to harvest energy from flows. The main argument to identify flapping states is based on a simple resonance condition between the characteristic (elastic) time of the system and the flow time-scale. Similar arguments have been successful in other fields of fluid dynamics and fluid-structure interactions including turbulent flows of dilute polymer solutions and interactions between the wake originated by bluff bodies and elastic structures. The predictions of the geometrical/physical properties associated to critical conditions (i.e. those separating stable stages from flapping regimes) have been compared against the results of experiments, numerical simulations and a phenomenological model based on a set of ordinary differential equations. Results clearly confirm the expectations from the resonance condition. Discussions on how to extend our analysis in situations where the extraction stage is taken into account are also

provided: this latter is indeed expected to influence the flapping stage and thus the critical conditions for flapping.

2. U. Lācis, S. Olivieri, A. Mazzino, and S. Bagheri. "Passive control of a falling sphere by elliptic-shaped appendages". *Physical Review Fluids* 2 (3 2017), p. 033901

   The majority of investigations characterizing the motion of single or multiple particles in fluid flows consider canonical body shapes, such as spheres, cylinders, discs, etc. However, protrusions on bodies—either surface imperfections or appendages that serve a function—are ubiquitous in both nature and applications. In this work, we characterize how the dynamics of a sphere with an axis-symmetric wake is modified in the presence of thin three-dimensional elliptic-shaped protrusions. By investigating a wide range of three-dimensional appendages with different aspect ratios and lengths, we clearly show that the sphere with an appendage may robustly undergo an inverted-pendulum-like (IPL) instability. This means that the position of the appendage placed behind the sphere and aligned with the free-stream direction is unstable, similar to how an inverted pendulum is unstable under gravity. Due to this instability, nontrivial forces are generated on the body, leading to turn and drift, if the body is free to fall under gravity. Moreover, we identify the aspect ratio and length of the appendage that induces the largest side force on the sphere, and therefore also the largest drift for a freely falling body. Finally, we explain the physical mechanisms behind these observations in the context of the IPL instability, i.e., the balance between surface area of the appendage exposed to reversed flow in the wake and the surface area of the appendage exposed to fast free-stream flow.

3. G. Boccalero, S. Olivieri, A. Mazzino, and C. Boragno. "Power harvesting by electromagnetic coupling from wind-induced limit cycle oscillations". *Smart Materials and Structures* 26.9 (2017), p. 095031

   Recent developments of low-power microprocessors open to new applications such as wireless sensor networks (WSN) with the consequent problem of autonomous powering. For this purpose, a possible strategy is represented by energy harvesting from wind or other flows exploiting fluid–structure interactions. In this work, we present an updated picture of a flutter-based device characterized by fully passive dynamics and a simple constructive layout, where limit cycle oscillations are undergone by an elastically bounded wing. In this case, the conversion from mechanical to electrical energy is performed by means of an electromagnetic coupling between a pair of coils and magnets. A centimetric-size prototype is shown to harvest energy from low wind velocities (between 2

and 4 ms^{-1}), reaching a power peak of 14 mW, representing a valuable amount for applications related to WSN. A mathematical description of the nonlinear dynamics is then provided by a quasi-steady phenomenological model, revealing satisfactory agreement with the experimental framework within a certain parametric range and representing a useful tool for future optimizations.

4. S. Boi, A. Mazzino, P. Muratore-Ginanneschi, and S. Olivieri. "Generalization of Taylor's formula to particles of arbitrary inertia". *Physical Review Fluids* 3 (10 2018), p. 104501

   One of the cornerstones of turbulent dispersion is the celebrated Taylor's formula. This formula expresses the rate of transport (i.e., the eddy diffusivity) of a tracer as a time integral of the fluid velocity autocorrelation function evaluated along the fluid particle trajectories. Here, we review the hypotheses which permit us to extend Taylor's formula to particles of any inertia. The hypotheses are independent of the details of the inertial particle model. We also show by explicit calculation that the hypotheses encompass cases when memory terms such as Basset's and Faxén's corrections are taken into account in the modeling of inertial particle dynamics.

5. S. Olivieri, C. Boragno, R. Verzicco, and A. Mazzino. "Constructive interference in a network of elastically-bounded flapping plates". *Journal of Fluids and Structures* 90 (2019), pp. 334–353

   Aeroelastic phenomena are gaining significant attention from the perspective of energy harvesting (EH) with promising applications in supplying low-power remote sensors. Besides the development of individual EH devices, further issues are posed when considering multiple objects for realizing arrays of devices and magnifying the extracted power. Due to nonlinear mutual interactions, the resulting dynamics is generally different from that of single devices and the setup optimization turns out to be nontrivial. In this work, we investigate the problem focusing on a flutter-based EH system consisting of a rigid plate anchored by elastic elements and invested by a uniform laminar flow, undergoing regular limit-cycle oscillations and flapping motions of finite amplitude. We consider a simplified, yet general, physical model and employ three-dimensional direct numerical simulations based on a finite-difference Navier–Stokes solver combined with a moving-least-squares immersed boundary method. Focusing on main kinematic and performance-related quantities, we first report on the dynamics of the single device and then on multiple devices, considering different arrangements (i.e.: in-line, staggered and side-by-side). A parametric exploration is performed by varying the mutual distance between the devices and insights are

provided. For the in-line arrangement, a recovery in performance for downstream devices is achieved by tuning their elasticity. Moreover, cooperative effects in the side-by-side arrangement are found to be substantially beneficial in terms of resulting power, with increases (i.e. constructive interference) up to 100% with respect to the single-device configuration. In order to confirm this numerical evidence, complementary results from wind-tunnel experiments are presented. Finally, we describe the system behaviour when increasing further the number of devices, outlining the ultimate goal of developing a high-performance EH network of numerous aeroelastic energy harvesters.

6. M. E. Rosti, S. Olivieri, A. A. Banaei, L. Brandt, and A. Mazzino. "Flowing fibers as a proxy of turbulence statistics". *Meccanica* 55 (2020), pp. 357–370

   The flapping states of a flexible fiber fully coupled to a three-dimensional turbulent flow are investigated via state-of-the-art numerical methods. Two distinct flapping regimes are predicted by the phenomenological theory recently proposed by Rosti et al. (Phys. Rev. Lett. 121:044501, 2018) the under-damped regime, where the elasticity strongly affects the fiber dynamics, and the over-damped regime, where the elastic effects are strongly inhibited. In both cases we can identify a critical value of the bending rigidity of the fiber by a resonance condition, which further provides a distinction between different flapping behaviors, especially in the under-damped case. We validate the theory by means of direct numerical simulations and find that, both for the over-damped regime and for the under-damped one, fibers are effectively slaved to the turbulent fluctuations and can therefore be used as a proxy to measure various two-point statistics of turbulence. Finally, we show that this holds true also in the case of a passive fiber, without any feedback force on the fluid.

7. M. Cavaiola, S. Olivieri, and A. Mazzino. "The assembly of freely moving rigid fibers measures the flow velocity gradient tensor" (2020). (under review)

   The motion of an assembly of rigid fibers is investigated for different classes of closed streamline flows, steady or time dependent, two dimensional or three dimensional. In our study, the dynamics of the fiber assembly is fully-coupled to the flow field by means of a state-of-the-art immersed boundary method. We show that, for sufficiently small Stokes times of the assembly, the whole flow gradient tensor can be accurately reconstructed by simply tracking the fiber assembly and measuring suitable fiber velocity differences evaluated at the fibers ends. Our results strongly suggest the possibility of using rigid fibers (or assembly of them) to perform flow measures either in laboratory or in field. Experiments are mandatory to inquire this latter possibility including the one

of exploiting our new findings to give birth to a 'Fiber Image Velocimetry' as a new technique to measure multi-point flow properties.

Proceedings of international conferences

1. S. Olivieri, G. Boccalero, A. Mazzino, and C. Boragno. "FLuttering Energy Harvester for Autonomous Powering (FLEHAP): aeroelastic characterisation and preliminary performance evaluation". *Procedia Engineering* 199 (2017). X International Conference on Structural Dynamics, EURODYN 2017, pp. 3474 –3479

   Significant efforts are being devoted in order to develop efficient and reliable energy harvesters based on interactions between structures and environmental fluid flows such as wind or marine currents. In this framework, a fully-passive energy harvester of centimetric size employing an elastically bounded wing has been developed. The system exploits the coupled-mode flutter, leading in certain conditions to finite amplitude and self-sustained oscillations. Electrical output power levels up to 15[mW] have been reached by an experimental prototype within a wind range between 2 and 5 [m/s] by means of electromagnetic coupling as the conversion strategy. Focusing on the aeroelastic point of view, it is crucial to investigate how the kinematics (i.e. flapping amplitude and frequency, phase between the pitch and plunge motion DoFs) varies with the main parameters (e.g. wind velocity and wing geometry), in order to identify the optimal conditions for potential harvesting. With this goal in mind, we present and discuss the results for a representative configuration of the device (first without the extraction mechanism), exploring the behavior within the design wind range, combining wind-tunnel experiments, three-dimensional CFD simulations and the development of a quasi-steady phenomenological model. We find that both the amplitude and the frequency of the flapping motion are maximised for a certain wind velocity. Moreover, the phase between pitch and plunge changes abruptly when close to this condition. Hence, we estimate the mechanical power that the wing is able to collect and the Betz efficiency, e.g. the ratio between the latter and the power available in the flow. The mathematical model is then enriched by additional terms mimicking an electrical resistive circuit and predictions are made regarding the extracted power and global efficiency of the system, showing the presence of optimal conditions for which these quantities are maximised. Finally, we outline future challenges in the harvester development towards a realistic deployment.

2. G. Boccalero, C. Boragno, S. Olivieri, and A. Mazzino. "FLuttering Energy Harvester for Autonomous Powering (FLEHAP): a synergy between EMc and Dielectric Elastomers Generators". *Procedia Engineering* 199 (2017). X International Conference on Structural Dynamics, EURODYN 2017, pp. 3428 –3433

   Energy Harvesting is the main solution to ensure the powering of sensors and micro-processors, especially in extreme environmental conditions where the use of batteries can be expensive or even impractical. In this work, a coupled-mode aero elastic fluttering system, exploiting self-sustained oscillations to harvest electrical energy from the mechanical one, is proposed. An airfoil can freely turn around its rotational axis, bounded to two elastomers parallel to the flow: in the presence of a fluid in motion, under particular mechanical conditions, the system exhibits limit cycle oscillations characterized by noteworthy amplitude and frequency. Moving in the space of parameters every flow speed range is theoretically achievable for the purposes of electrical extraction; this work will focus on low wind speed conditions. By positioning a pair of coils at the ends of the rotational axis of the wing and fixing magnets in an alternated polarity in front of their quasi-vertical harmonic motion, an electro-magnetic coupling (EMc) is obtained: during the oscillations an alternated voltage at the ends of the coils is measured. Dielectric Elastomer Generators (DEGs), composite material formed by coupling two stretchable electrodes to a high permittivity rubber, forming a capacitor in which the capacitance changes with the stretching, replace traditional elastomers: this permits, by charging the DEGs in the maximal stretched status and discharging it in the pre-stretch status, to amplify the input voltage. DEGs cannot be an autonomous powering, because they need an external electrical energy source. Synergistically, the use of an integrated circuit designed for storing efficiently the charges from the EMc in a supercapacitor (SC), and electronics able to manage the DEGs by a 'charge pumping' process supplying a second SC, allows to ensure an excellent and adaptable autonomous powering. A further synergy is introduced exploiting intrinsic effects of the two electrical extraction strategies adopted in the system: EM damping due to the resistance load, and the change in stiffness of DEGs when a voltage is applied, can extend the operating speed range, increasing its global efficiency. Centimeter-sized devices exploiting EMc and DEGs, and an overview about DEGs materials are presented in this work.

Communications at scientific events

1. S. Olivieri, G. Boccalero, A. Mazzino, and C. Boragno. "FLEHAP: FLuttering Energy Harvester for Autonomous Powering". 1st Winter School in Multiscale Approaches and Multiphysic Couplings in Fluid and Solid Mechanics. Grenoble (France), 16 January 2017 [Poster]

2. S. Olivieri, G. Boccalero, A. Mazzino, and C. Boragno. "Energy harvesting by an elastically-bounded flapping wing: aeroelastic investigation and performance evaluation". 4th Workshop in Devices, Materials and Structures for Energy Harvesting and Storage. Oulu (Finland), 17 May 2017 [Talk]

3. S. Olivieri, G. Boccalero, A. Mazzino, and C. Boragno. "FLuttering Energy Harvester for Autonomous Powering (FLEHAP): aeroelastic characterisation and preliminary performance evaluation". X International Conference on Structural Dynamics, EURODYN 2017. Rome (Italy), 13 September 2017 [Talk]

4. S. Olivieri, M. E. Rosti, A. A. Banaei, L. Brandt, and A. Mazzino. "Flowing fibers as a proxy for two-point measurements in turbulent flows". CISM-AIMETA Advanced school on Anisotropic Particles in Viscous and Turbulent Flows. Udine (Italy), 5 July 2019 [Talk]

5. S. Olivieri, C. Boragno, R. Verzicco, and A. Mazzino. "On the dynamics of multiple elastically-bounded flapping plates for flow energy harvesting". 17th European Turbulence Conference. Turin (Italy), 6 September 2019 [Talk]

(only the contributions where the Candidate was the presenting author are reported)

Bibliography

[1] A. Abdelkefi. "Aeroelastic energy harvesting: A review". *International Journal of Engineering Science* 100 (2016), pp. 112 –135.

[2] I. Akyildiz, W. Su, Y. Sankarasubramaniam, and E. Cayirci. "Wireless sensor networks: a survey". *Computer Networks* 38.4 (2002), pp. 393 –422.

[3] X. Amandolese, S. Michelin, and M. Choquel. "Low speed flutter and limit cycle oscillations of a two-degree-of-freedom flat plate in a wind tunnel". *Journal of Fluids and Structures* 43 (2013), pp. 244 –255.

[4] A Andersen, U Pesavento, and Z. J. Wang. "Unsteady aerodynamics of fluttering and tumbling plates". *Journal of Fluid Mechanics* 541 (2005), pp. 65–90.

[5] R. L. Bisplinghoff, H. Ashley, and R. L. Halfman. *Aeroelasticity*. Dover Publications, 1955.

[6] R. D. Blevins. *Flow-induced vibration*. Van Nostrand Reinhold, 1990.

[7] G. Boccalero, C. Boragno, S. Olivieri, and A. Mazzino. "FLuttering Energy Harvester for Autonomous Powering (FLEHAP): a synergy between EMc and Dielectric Elastomers Generators". *Procedia Engineering* 199 (2017). X International Conference on Structural Dynamics, EURODYN 2017, pp. 3428 –3433.

[8] G. Boccalero, S. Olivieri, A. Mazzino, and C. Boragno. "Power harvesting by electromagnetic coupling from wind-induced limit cycle oscillations". *Smart Materials and Structures* 26.9 (2017), p. 095031.

[9] G. Boccalero, C. Boragno, D. D. Caviglia, and R. Morasso. "FLEHAP: A Wind Powered Supply for Autonomous Sensor Nodes". *Journal of Sensor and Actuator Networks* 5.4 (2016), p. 15.

[10] S. Boi, A. Mazzino, P. Muratore-Ginanneschi, and S. Olivieri. "Generalization of Taylor's formula to particles of arbitrary inertia". *Physical Review Fluids* 3 (10 2018), p. 104501.

[11] C. Boragno, R. Festa, and A. Mazzino. "Elastically bounded flapping wing for energy harvesting". *Applied Physics Letters* 100.25 (2012), p. 253906.

[12] M. Boudreau, G. Dumas, M. Rahimpour, and P. Oshkai. "Experimental investigation of the energy extraction by a fully-passive flapping-foil hydrokinetic turbine prototype". *Journal of Fluids and Structures* 82 (2018), pp. 446 –472.

[13] S. Bressers, D. Avirovik, C. Vernieri, J. Regan, S. Chappell, M. Hotze, S. Luhman, M. Lallart, D. Inman, and S. Priya. "Small-scale modular windmill". *American Ceramics Society Bulletin* 89.8 (2010), pp. 34–40.

[14] W.-P. Breugem. "A second-order accurate immersed boundary method for fully resolved simulations of particle-laden flows". *Journal of Computational Physics* 231.13 (2012), pp. 4469–4498.

[15] M. Bryant, J. C. Gomez, and E. Garcia. "Reduced-order aerodynamic modeling of flapping wing energy harvesting at low reynolds number". *AIAA Journal* 51.12 (2013), pp. 2771–2782.

[16] M. Bryant, A. D. Schlichting, and E. Garcia. "Toward efficient aeroelastic energy harvesting: device performance comparisons and improvements through synchronized switching". *Proceedings of SPIE* 8688 (2013), pp. 868807–868807–10.

[17] M. Bryant, R. L. Mahtani, and E. Garcia. "Wake synergies enhance performance in aeroelastic vibration energy harvesting". *Journal of Intelligent Material Systems and Structures* 23.10 (2012), pp. 1131–1141.

[18] M. Cavaiola, S. Olivieri, and A. Mazzino. "The assembly of freely moving rigid fibers measures the flow velocity gradient tensor" (2020). (under review).

[19] A. Collar. "The expanding domain of aeroelasticity". *The Aeronautical Journal* 50.428 (1946), pp. 613–636.

[20] H. Dai, A Abdelkefi, U Javed, and L Wang. "Modeling and performance of electromagnetic energy harvesting from galloping oscillations". *Smart Materials and Structures* 24.4 (2015), p. 045012.

[21] Digital Transformation Monitor. *Energy harvesting to power the rise of the Internet of Things*. 2017.

[22] G. Dimitriadis and J. Li. "Bifurcation Behavior of Airfoil Undergoing Stall Flutter Oscillations in Low-Speed Wind Tunnel". *AIAA Journal* 47.11 (2009), pp. 2577–2596.

[23] E. H. Dowell and D. Tang. "Nonlinear Aeroelasticity and Unsteady Aerodynamics". *AIAA Journal* 40.9 (2002), pp. 1697–1707.

[24] E. Dowell. *A Modern course in aeroelasticity*. Mechanics: Dynamical Systems Series. Sijthoff & Noordhoff, 1978.

[25] E. A. Fadlun, R. Verzicco, P. Orlandi, and J. Mohd-Yusof. "Combined immersed-boundary finite-difference methods for three-dimensional complex flow simulations". *Journal of Computational Physics* 161.1 (2000), pp. 35–60.

[26] J. Favier, A. Revell, and A. Pinelli. "Numerical study of flapping filaments in a uniform fluid flow". *Journal of Fluids and Structures* 53 (2015). Special Issue on Unsteady Separation in Fluid-Structure Interaction–II, pp. 26 –35.

[27] J. H. Ferziger and M. Peric. *Computational methods for fluid dynamics*. Springer Science & Business Media, 2012.

[28] J. Gubbi, R. Buyya, S. Marusic, and M. Palaniswami. "Internet of Things (IoT): A vision, architectural elements, and future directions". *Future Generation Computer Systems* 29.7 (2013), pp. 1645 –1660.

[29] G. Haller. "An objective definition of a vortex". *Journal of Fluid Mechanics* 525 (2005), 1–26.

[30] A. Harb. "Energy harvesting: State-of-the-art". *Renewable Energy* 36.10 (2011). Renewable Energy: Generation & Application, pp. 2641 –2654.

[31] A. S. Holmes. "Energy Harvesting from Fluid Flows". *Micro Energy Harvesting*. Wiley-VCH Verlag GmbH & Co. KGaA, 2015, pp. 297–319.

[32] R. Hu and L. Wang. "Motion transitions of falling plates via quasisteady aerodynamics". *Physical Review E* 90.1 (2014), p. 013020.

[33] W.-X. Huang and H. J. Sung. "Three-dimensional simulation of a flapping flag in a uniform flow". *Journal of Fluid Mechanics* 653 (2010), pp. 301–336.

[34] W. Huang, H. Liu, F. Wang, J. Wu, and H. P. Zhang. "Experimetal study of a freely falling plate with an inhomogeneous mass distribution". *Physical Review E* 88 (5 2013), p. 053008.

[35] C. Huertas-Cerdeira, B. Fan, and M. Gharib. "Coupled motion of two side-by-side inverted flags". *Journal of Fluids and Structures* 76 (2018), pp. 527 –535.

[36] G. Iaccarino and R. Verzicco. "Immersed boundary technique for turbulent flow simulations". *Applied Mechanics Reviews* 56.3 (2003), pp. 331–347.

[37] E. Jonsson, C. Riso, C. A. Lupp, C. E. Cesnik, J. R. Martins, and B. I. Epureanu. "Flutter and post-flutter constraints in aircraft design optimization". *Progress in Aerospace Sciences* 109 (2019), p. 100537.

[38] B. Kirschmeier and M. Bryant. "Experimental investigation of wake-induced aeroelastic limit cycle oscillations in tandem wings". *Journal of Fluids and Structures* 81 (2018), pp. 309 –324.

[39] S.-D. Kwon. "A T-shaped piezoelectric cantilever for fluid energy harvesting". *Applied Physics Letters* 97.16, 164102 (2010), p. 164102.

[40] U Lācis, N. Brosse, F Ingremeau, A Mazzino, F. Lundell, H Kellay, and S. Bagheri. "Passive appendages generate drift through symmetry breaking". *Nature Communications* 5 (2014), p. 5310.

[41] U. Lācis, S. Olivieri, A. Mazzino, and S. Bagheri. "Passive control of a falling sphere by elliptic-shaped appendages". *Physical Review Fluids* 2 (3 2017), p. 033901.

[42] B. Lee, S. Price, and Y. Wong. "Nonlinear aeroelastic analysis of airfoils: bifurcation and chaos". *Progress in Aerospace Sciences* 35.3 (1999), pp. 205 –334.

[43] I. Lee and H. Choi. "A discrete-forcing immersed boundary method for the fluid–structure interaction of an elastic slender body". *Journal of Computational Physics* 280 (2015), pp. 529–546.

[44] Y. J. Lee, K. B. Lua, T. T. Lim, and K. S. Yeo. "A quasi-steady aerodynamic model for flapping flight with improved adaptability". *Bioinspiration & Biomimetics* 11.3 (2016), p. 036005.

[45] D. Li, Y. Wu, A. D. Ronch, and J. Xiang. "Energy harvesting by means of flow-induced vibrations on aerospace vehicles". *Progress in Aerospace Sciences* 86 (2016), pp. 28 –62.

[46] S. Li, J. Yuan, and H. Lipson. "Ambient wind energy harvesting using cross-flow fluttering". *Journal of Applied Physics* 109.2 (2011), p. 026104.

[47] J. McCarthy, A. Deivasigamani, S. John, S. Watkins, F. Coman, and P. Petersen. "Downstream flow structures of a fluttering piezoelectric energy harvester". *Experimental Thermal and Fluid Science* 51 (2013), pp. 279 –290.

[48] J. McCarthy, S. Watkins, A. Deivasigamani, and S. John. "Fluttering energy harvesters in the wind: A review". *Journal of Sound and Vibration* 361 (2016), pp. 355 –377.

[49] J. McCarthy, A. Deivasigamani, S. Watkins, S. John, F. Coman, and P. Petersen. "On the visualisation of flow structures downstream of fluttering piezoelectric energy harvesters in a tandem configuration". *Experimental Thermal and Fluid Science* 57 (2014), pp. 407 –419.

[50] D. C. Meeker. *Finite Element Method Magnetics.*

[51] K. Menon and R. Mittal. "Flow physics and dynamics of flow-induced pitch oscillations of an airfoil". *Journal of Fluid Mechanics* 877 (2019), 582–613.

[52] S. Michelin and O. Doaré. "Energy harvesting efficiency of piezoelectric flags in axial flows". *Journal of Fluid Mechanics* 714 (2013), 489–504.

[53] R. Mittal and G. Iaccarino. "Immersed boundary methods". *Annual Review of Fluid Mechanics* 37.1 (2005), pp. 239–261.

[54] T. J. Mueller and J. D. DeLaurier. "Aerodynamics of small vehicles". *Annual Review of Fluid Mechanics* 35.1 (2003), pp. 89–111.

[55] S. Olivieri, C. Boragno, R. Verzicco, and A. Mazzino. "Constructive interference in a network of elastically-bounded flapping plates". *Journal of Fluids and Structures* 90 (2019), pp. 334–353.

[56] S. Olivieri, G. Boccalero, A. Mazzino, and C. Boragno. "Energy harvesting by an elastically-bounded flapping wing: aeroelastic investigation and performance evaluation". 4th Workshop in Devices, Materials and Structures for Energy Harvesting and Storage. Oulu (Finland), 17 May 2017.

[57] S. Olivieri, G. Boccalero, A. Mazzino, and C. Boragno. "FLEHAP: FLuttering Energy Harvester for Autonomous Powering". 1st Winter School in Multiscale Approaches and Multiphysic Couplings in Fluid and Solid Mechanics. Grenoble (France), 16 January 2017.

[58] S. Olivieri, M. E. Rosti, A. A. Banaei, L. Brandt, and A. Mazzino. "Flowing fibers as a proxy for two-point measurements in turbulent flows". CISM-AIMETA Advanced school on Anisotropic Particles in Viscous and Turbulent Flows. Udine (Italy), 5 July 2019.

[59] S. Olivieri, G. Boccalero, A. Mazzino, and C. Boragno. "Fluttering conditions of an energy harvester for autonomous powering". *Renewable Energy* 105 (2017), pp. 530–538.

[60] S. Olivieri, G. Boccalero, A. Mazzino, and C. Boragno. "FLuttering Energy Harvester for Autonomous Powering (FLEHAP): aeroelastic characterisation and preliminary performance evaluation". X International Conference on Structural Dynamics, EURODYN 2017. Rome (Italy), 13 September 2017.

[61] S. Olivieri, C. Boragno, R. Verzicco, and A. Mazzino. "On the dynamics of multiple elastically-bounded flapping plates for flow energy harvesting". 17th European Turbulence Conference. Turin (Italy), 6 September 2019.

[62] S. Olivieri, G. Boccalero, A. Mazzino, and C. Boragno. "FLuttering Energy Harvester for Autonomous Powering (FLEHAP): aeroelastic characterisation and preliminary performance evaluation". *Procedia Engineering* 199 (2017). X International Conference on Structural Dynamics, EURODYN 2017, pp. 3474 –3479.

[63] *OpenFOAM, The open source CFD toolbox* – `http://www.openfoam.com`.

[64] A. Orchini, A. Mazzino, J. Guerrero, R. Festa, and C. Boragno. "Flapping states of an elastically anchored plate in a uniform flow with applications to energy harvesting by fluid-structure interaction". *Physics of Fluids* 25.9 (2013), p. 097105.

[65] Z. Peng and Q. Zhu. "Energy harvesting through flow-induced oscillations of a foil". *Physics of Fluids* 21.12 (2009), p. 123602.

[66] C. S. Peskin. "Flow patterns around heart valves: a numerical method". *Journal of Computational Physics* 10.2 (1972), pp. 252–271.

[67] C. S. Peskin. "The immersed boundary method". *Acta numerica* 11 (2002), pp. 479–517.

[68] L. Pigolotti, C. Mannini, G. Bartoli, and K. Thiele. "Critical and post-critical behaviour of two-degree-of-freedom flutter-based generators". *Journal of Sound and Vibration* 404 (2017), pp. 116 –140.

[69] L. Pigolotti, C. Mannini, and G. Bartoli. "Destabilizing effect of damping on the post-critical flutter oscillations of flat plates". *Meccanica* 52.13 (2017), pp. 3149–3164.

[70] L. Pigolotti, C. Mannini, and G. Bartoli. "Experimental study on the flutter-induced motion of two-degree-of-freedom plates". *Journal of Fluids and Structures* 75 (2017), pp. 77 –98.

[71] D. Poirel, V. Métivier, and G. Dumas. "Computational aeroelastic simulations of self-sustained pitch oscillations of a NACA0012 at transitional Reynolds numbers". *Journal of Fluids and Structures* 27.8 (2011), pp. 1262 –1277.

[72] K. Ramesh, J. Murua, and A. Gopalarathnam. "Limit-cycle oscillations in unsteady flows dominated by intermittent leading-edge vortex shedding". *Journal of Fluids and Structures* 55 (2015), pp. 84 –105.

[73] P. Rawat, K. D. Singh, H. Chaouchi, and J. M. Bonnin. "Wireless sensor networks: a survey on recent developments and potential synergies". *Journal of Supercomputing* 68.1 (2014), pp. 1–48.

[74] N. A. Razak, T. Andrianne, and G. Dimitriadis. "Flutter and Stall Flutter of a Rectangular Wing in a Wind Tunnel". *AIAA Journal* 49.10 (2011), pp. 2258–2271.

[75] S. L. Rosen. *Fundamental Principles of Polymeric Materials*. Wiley, 1982.

[76] M. E. Rosti, S. Olivieri, A. A. Banaei, L. Brandt, and A. Mazzino. "Flowing fibers as a proxy of turbulence statistics". *Meccanica* 55 (2020), pp. 357–370.

[77] M. E. Rosti, A. A. Banaei, L. Brandt, and A. Mazzino. "Flexible Fiber Reveals the Two-Point Statistical Properties of Turbulence". *Physical Review Letters* 121 (4 2018), p. 044501.

[78] T. Sarpkaya. "Vortex-Induced Oscillations: A Selective Review". *Journal of Applied Mechanics* 46.2 (1979), pp. 241–258.

[79] M. J. Shelley and J. Zhang. "Flapping and bending bodies interacting with fluid flows". *Annual Review of Fluid Mechanics* 43 (2011), pp. 449–465.

[80] K. Shoele and R. Mittal. "Energy harvesting by flow-induced flutter in a simple model of an inverted piezoelectric flag". *Journal of Fluid Mechanics* 790 (2016), 582–606.

[81] J. Sirohi and R. Mahadik. "Piezoelectric wind energy harvester for low-power sensors". *Journal of Intelligent Material Systems and Structures* 22.18 (2011), pp. 2215–2228.

[82] V. Spandan, V. Meschini, R. Ostilla-Mónico, D. Lohse, G. Querzoli, M. D. de Tullio, and R. Verzicco. "A parallel interaction potential approach coupled with the immersed boundary method for fully resolved simulations of deformable interfaces and membranes". *Journal of Computational Physics* 348 (2017), pp. 567 –590.

[83] L. Tang, M. P. Païdoussis, and J. Jiang. "Cantilevered flexible plates in axial flow: Energy transfer and the concept of flutter-mill". *Journal of Sound and Vibration* 326.1 (2009), pp. 263 –276.

[84] T. Theodorsen. *General Theory of Aerodynamic Instability and the Mechanism of Flutter*. Tech. rep. 496. NACA, 1935.

[85] M. de Tullio and G. Pascazio. "A moving-least-squares immersed boundary method for simulating the fluid-structure interaction of elastic bodies with arbitrary thickness". *Journal of Computational Physics* 325 (2016), pp. 201 –225.

[86] M. Uhlmann. "An immersed boundary method with direct forcing for the simulation of particulate flows". *Journal of Computational Physics* 209.2 (2005), pp. 448–476.

[87] M. Vanella and E. Balaras. "A moving-least-squares reconstruction for embedded-boundary formulations". *Journal of Computational Physics* 228.18 (2009), pp. 6617 –6628.

[88] J.-C. Veilleux and G. Dumas. "Numerical optimization of a fully-passive flapping-airfoil turbine". *Journal of Fluids and Structures* 70 (2017), pp. 102 –130.

[89] R. Verzicco and P. Orlandi. "A Finite-Difference Scheme for Three-Dimensional Incompressible Flows in Cylindrical Coordinates". *Journal of Computational Physics* 123.2 (1996), pp. 402 –414.

[90] E. Wang, K. Ramesh, S. Killen, and I. M. Viola. "On the nonlinear dynamics of self-sustained limit-cycle oscillations in a flapping-foil energy harvester". *Journal of Fluids and Structures* 83 (2018), pp. 339 –357.

[91] Z. Wang, L. Du, J. Zhao, and X. Sun. "Structural response and energy extraction of a fully passive flapping foil". *Journal of Fluids and Structures* 72 (2017), pp. 96 –113.

[92] Q. Xiao and Q. Zhu. "A review on flow energy harvesters based on flapping foils". *Journal of Fluids and Structures* 46 (2014), pp. 174 –191.

[93] J. Young, J. Lai, and M. F. Platzer. "A review of progress and challenges in flapping foil power generation". *Progress in Aerospace Sciences* 67 (2014), pp. 2–28.

[94] J. Young, M. A. Ashraf, J. C. Lai, and M. F. Platzer. "Numerical simulation of fully passive flapping foil power generation". *AIAA Journal* 51.11 (2013), pp. 2727–2739.

[95] J. Zhang, S. Childress, A. Libchaber, and M. Shelley. "Flexible filaments in a flowing soap film as a model for one-dimensional flags in a two-dimensional wind". *Nature* 408.6814 (2000), p. 835.

[96] D. Zhu, S. P. Beeby, M. J. Tudor, N. M. White, and N. R. Harris. "Novel Miniature Airflow Energy Harvester for Wireless Sensing Applications in Buildings". *IEEE Sensors Journal* 13.2 (2013), pp. 691–700.

[97] Q. Zhu. "Energy harvesting by a purely passive flapping foil from shear flows". *Journal of Fluids and Structures* 34 (2012), pp. 157 –169.

Ringraziamenti

Giunto al termine di questo percorso, desidero ringraziare tutte le persone che in questi anni sono state per me importanti.

In primis, il mio grazie va al mio supervisore Prof. Andrea Mazzino, per lo stimolo costante nell'attività di ricerca scientifica e per le numerose opportunità per la mia crescita professionale, nonché per il supporto sul piano umano e nei momenti di difficoltà.

Voglio ringraziare tutti i Docenti del DICCA per il confronto sul piano scientifico, professionale ed umano, ed in particolare i Proff. Alessandro Bottaro e Jan Pralits che hanno avuto un ruolo significativo nella mia carriera universitaria.

Il risultato di questa Tesi non sarebbe stato possibile senza i seguenti Ricercatori all'infuori del DICCA con cui ho avuto la fortuna di collaborare, ampliando sensibilmente il mio bagaglio di conoscenze e competenze: Corrado Boragno, Gregorio Boccalero, Roberto Verzicco, Shervin Bagheri, Uğis Lācis, Paolo Muratore-Ginanneschi, Marco Edoardo Rosti, Arash Alizad Banaei e Luca Brandt.

Grazie a tutti i colleghi *Flubii* delle varie 'generazioni', coi quali è stato bello lavorare insieme o anche solo condividere la quotidiana vita di ufficio: Damiano, Edoardo, Giuseppe, Joel, Matteo, Simone, e più recentemente Biniyam, Mattia e Sarish. Grazie anche ai compagni del XXXII Ciclo: Arianna, Francesco D. e Stefano P., e a tutti i Dottorandi e Assegnisti del DICCA, in particolare i Francesco (E. e F.) e Gaetano.

Desidero infine ringraziare tutti gli amici ed i miei familiari. In particolar modo, ai miei genitori: grazie per il sostegno e soprattutto per l'ispirazione che mi avete saputo dare con la vostra vita.